Single Crystal Silicon as a Macro-World Structural Material: Application to Compact, Lightweight High Pressure Vessels

by

Tanya Cruz Garza

B.S., Massachusetts Institute of Technology (2004)
S.M., Massachusetts Institute of Technology (2007)

Submitted to the Department of Aeronautics and Astronautics
in Partial fulfillment of the requirements for the degree of
Doctor of Philosophy in Aeronautics and Astronautics
at the
Massachusetts Institute of Technology
February 2011

Signature of Author……..
Department of Aeronautics and Astronautics
January 27, 2011

Certified by……...
Alan H. Epstein
Professor Emeritus
Committee Chair

Certified by……...
S. Mark Spearing
Professor of Engineering Materials, Head of School of Engineering Sciences, University of Southampton

Certified by……...
Martin A. Schmidt
Professor of Electrical Engineering; Associate Provost

Certified by……...
Raul A. Radovitzky
Associate Professor

Accepted by……
Eytan H. Modiano
Chairman, Department Committee on Graduate Theses

Single Crystal Silicon as a Macro-World Structural Material: Application to Compact, Lightweight High Pressure Vessels

by

Tanya Cruz Garza

Submitted to the Department of Aeronautics and Astronautics
on January 27, 2011, in partial fulfillment of the
requirements for the degree of
Doctor of Philosophy in Aeronautics and Astronautics

Abstract

Single crystal silicon has promising inherent structural properties which are attractive for weight sensitive applications. Single crystal silicon, however, is a brittle material which makes the usable strength that can be obtained from silicon devices dependent on flaws or cracks that can arise during fabrication in a sample that begins relatively free of defects. This research explores the use of micro-machined, single crystal silicon (Si) for high-strength macro-scale application and determines its practical advantages when compared to conventional approaches. The major contributions of this thesis includes evaluation of wafer-scale silicon for macro-world applications, identification of cellular pressure vessels as a promising wafer-scale silicon device, identification of design criteria for brittle pressure vessels and quantified metrics for a competitive silicon pressure vessel design, identification of DRIE failure mechanisms, elucidation of the role of wafer-level strength variation related to surface morphology variation in wafer-scale structures, and identification of promising strength recovery techniques and promising avenues to explore for further strength improvements.

High pressure vessels for aerospace applications with volumes of 10's of cc's were designed under the premise that the superior strength-to-density ratio of Si and post-processing strength recovering techniques can compensate for fabrication technology limitations that constrain the vessel shape and for the brittle nature of the material. A combination of literature review, analysis, and numerical simulations suggest that there are single crystal silicon fabrication technology compromised pressure vessel designs that can have lower structural mass to pressurant mass ratios than conventional pressure vessel designs at design pressures above about 6000 psi. A honeycomb geometry offered the best results of those studied. The honeycomb silicon pressure vessel offers the possibility of integrated micro-valves, regulators and sensors. Such vessels would be useful for nano and pico satellites and for launch vehicles.

Fabrication processes and strength recovering techniques were explored experimentally to understand and improve the usable strength of microfabricated single crystal silicon macro-structures. It was found that silicon strength will vary across a DRIE etched wafer as a result of submicron sidewall roughness variation independent

of larger geometric parameter variation. Secondary anisotropic SF_6 plasma etching and surface migration were shown to be a promising combination for recovery of microfabricated silicon strength while oxidation and oxide removal offer less promise. Long SF_6 smoothing etches revealed significantly varied sidewall roughness from that hidden by overhanging silicon which affects correlations of surface morphology to device strength.

An analytical model was developed that correlates silicon strength data found experimentally to the silicon pressure vessel design. The model predicts that reasonable improvements to usable silicon strength need to be made to make a silicon pressure vessel design competitive with conventional designs. Further work on strength uniformity across wafer and strength recovery is recommended to improve the usable strength of wafer-scale, DRIE single crystal silicon devices.

Thesis Supervisor: Alan H. Epstein
Title: Professor Emeritus
Committee Chair

Acknowledgments

During my first year of grad school I spoke to a TA of mine who was finishing his Ph.D. after nearly a decade of working on it. I told him that it must feel wonderful to be finished. He did not respond to this in the smiling, joyous way I expected. He told me that the experience of the Ph.D. was infact an emotionally challenging experience filled with many unexpected twists. He told me that he didn't know if he would embark upon this experience again given what he had been through. After now going through a Ph.D. journey myself and seeing those around me go through the journey as well, I have found that my TA's experience was not out of the ordinary. Infact, the Ph.D. experience for me was one that did not come as easily as I might have hoped it would. It was an experience which required leaning on the support of others at numerous points along the way to finally make it to the end. For this reason, I take this section to acknowledge a number of people whom I thank God for and who made it possible for me to finish.

First I must acknowledge my advisor Professor Alan Epstein, a man who not only provided me with the resources I needed to complete this project but also provided me with consideration and mentorship. Professor Epstein has an amazing ability to see problems from a larger perspective and effectively derive a plan of action. In addition, Professor Epstein has an amazing sense of humor which never fails to improve any situation. I consider Professor Epstein to be an example of the kind of person I would hope to one day be.

I would like to thank my committee who helped my thesis work move more smoothly and whose guidence has shaped me into a better researcher. I want to thank Professor Mark Spearing for devoting time to help me through problems and for giving me lots of encouragement. I want to thank Professor Martin Schmidt for taking time to help me with microfabrication problems and helping me get microfabriction resources I could not get by myself. I would like to thank Professor Raul Radovitzky for providing me with time to help me with my research and providing resources from his lab.

I would also like to acknowledge my thesis readers. I would like to thank Dr. Hanqing Li for providing me with an unlimited amount of mentorship with all my microfabrication needs in addition to helpful comments on my thesis. I also would like to thank Dr. Stuart Jacobson for serving as the external evaluator for my thesis proposal defense as well as providing me with useful comments on my thesis.

I would like to thank the labs and professors who helped me achieve surface migration. I would like to thank Professor Roger Howe and his lab for helping me with hydrogen annealing and from his lab I would like to specifically thank Dr. Rishi Kant and J Provine. I would like to thank Professor Eugene A. Fitzgerald and his lab for helping me with UHV annealing and from his lab I would like to specifically thank Dr. Mayank Bulsara and Prithu Sharma.

I would like to thank Professor Greitzer for being my unofficial advisor and my in-lab motivator. I appreciate the time he spent to keep an eye on my progress and make me laugh. I also appreciate the award-winning costume ;-)

I would like to thank Professor Youssef Marzouk for providing me with mentorship and experience as a teaching assistant. I learned enourmous amounts from the responcibility I was given.

I would like to thank the GTL staff whose assistance made my life much easier and brighter. I would like to thank James Letendre for helping me put together my test setup as well as help me with every testing-related question I had. I would like to thank Dr. Gerald Guenette for lending me his expertiese from time to time. I want to thank Holly Anderson for helping me with all my purchasing needs, being a friend I could go to when I needed a break, being a positive addition to my life, and providing me with lots and lots of candy. I would thank Robin Courchesne-Sato for helping me with all kinds of problems as well as being so nice to me.

I would like to thank the great staff and students at MTL for their help with fabbing and kindness. I would like to thank Vicky Diadiuk for her assistance with my special needs and processes. I would like to thank David Terry for all his help in the lab and helping keep me sane through all those long fab hours. I would like to thank Daniel A. Adams, Donal Jamieson, Eric Lim, Gary Riggott, Paul Tierney, and

Dennis Ward for their patience with all my questions and messups as well as their friendliness. I would also like to thank all the MTL students for being friends in the fab, accomidating times when I needed to sneak onto machines early or run late, and sympathizing with my fab problems. I want to thank Namiko Yamamoto for sharing the MIT experience with me from unified to the extra years of grad school and always doing it with an encouraging smile.

I would like to acknowledge my labmates from both SPL and GTL for making the journey a little more enjoyable. I want to thank my officemates for being unpaid therapists as well as good friends to me. I want to thank Leo Ng for always alerting me about food events, talking to me about random things, teaching me about Canada (and taking Canada jokes well), and helping me with work. I want to thank Anne-Raphaelle Aubry for showing up just when Leo left and adding some great female personality to the lab. I want to thank Shinji Tanaka for staying a great friend even after many disagreements on office temperature and sunlight. I also want to thank Cong Luo, Daanish Maqbool, Hiten Mulchandani, and Yuan Wang for conversing with me even when you needed to be working.

I want to thank my weekly lunch crew Felix Parra, Luis Fernando Velasquez-Garcia, and Grigory Kagan who made the my life and week brighter. I also want to thank Felix for being a close friend and officemate. I also want to thank Luis for being a friend, mentor, and great help with my fab.

The last and perhaps most important school friend I would like to thank is Hansen Bow. Having someone to share every step of this experience with and to dine/coffee/snack-away my stress with is something I will truely miss.

I want to thank my non-grad school friends for keeping me balanced and taking me away from school sometimes. I want to thank Jessica Scott for reliably showing up to my events, offering me tons of encouragement, and making Mexican Thursday one of the best parts of my week. I also want to thank my additional Mexican Thursday buddies Michael Hirsh, Brett Anderson, Luke Bussey, and Brooke Sachs for amping up my Thursdays and weekends. I want to thank Cristina Costantino for getting people together when she lived in Boston and hosting me everytime I wanted a place

in NYC. I want to thank Jasmine Perez for also making my NYC escapes fun. I want to thank Sarah Foley for coming into my life when I could use another friend and bringing lots of crazy-time joy. I want to thank Sarah Knox and Justin Cichon for hosting me at so many awesome parties. I want to thank Emily Havens Greenhagen for so much support over the past years and for our Border Cafe dinners that would run late into the night. I want to thank Bryan Greenhagen for eating dinner so late because I kept Emily so long. I want to thank Nnnennia Ejebe for being like a sister to me even when she was so busy and so far. I want to thank Nina Kshetry for being a sincere and warm hearted friend who always shos me the good side of humanity. Finally, I want to thank Jesse Greene for always being my rock. Jesse has been there for every disaster and always talked me through it and given me a level head when I didn't have one of my own. I am very lucky to have a soulmate like Jesse and wouldn't want to have to get through the Ph.D. without him.

Finally, and perhaps most importantly, I want to thank my family whom I love so much and who has showed me so much love through this time. I want to thank my brother Cayetano Garza Jr. and my niece Beatrix Garza for moving close by and always being so positive and supportive. I want to thank my father Cayetano Garza Sr. for calling me every week to make sure I had everything I needed and providing for me when I did need something. I want to thank my brother and sister David Garza and Celeste Esparza and my niece Abigail Esparza Garza for giving me more love and support than I could ever dream is possible. Finally, I want to thank my mom Syliva Palacios Cruz who has aways believed I could do things even when I didn't believe I could do them myself, has always been proud of all my accomplishments even those I considered to be no big deal, has felt every pain and frustration I have ever had, who has dedicated her time and energy towards my success, and who has been a friend who has never let me down.

Contents

1 Introduction **21**

1.1 Context 21

1.1.1 Silicon Properties 22

1.1.2 Conventional Pressure Vessels 24

1.2 Relevant Work and Motivations 26

1.2.1 Structural Silicon MEMS 26

1.2.2 Work to Improve Silicon Strength 27

1.2.3 Motivations 29

1.3 Research Objectives 32

2 Design of a Silicon Pressure Vessel **33**

2.1 First Order Investigation of Silicon Designs 33

2.1.1 Silicon Vessel Designs 34

2.1.2 Conventional Vessel Designs 40

2.1.3 Final Comparison of Analytical Analysis 42

2.2 FEM Refinement of Designs 45

2.2.1 FEM Evaluation of Honeycomb Vessel 45

2.2.2 FEM Evaluation of the Concentric Tori Vessel 46

2.2.3 FEM Evaluation of the Wedge Vessel 47

2.2.4 Results of FEM Analysis 47

2.3 Conclusions 49

3 Exploring Usable Silicon Strength with Radius Hubbed Flexure Specimens **51**

3.1 Radius Hubbed Flexure Specimen Background 51

3.1.1 Strength Recovering Techniques 53

3.2 Fabrication 55

3.2.1 Surface Migration and Related Fabrication 59

3.3 Experimental Work 60

3.4 FEM Modelling 62

3.4.1 FEM Calculation of Uncertainty 63

3.5 Results 64

3.5.1 SEM Analysis of Smoothing 68

3.5.2 Exploring Sidewall Roughness 68

3.6 Summary 74

4 Probabilistic Design of Silicon Pressure Vessel **77**

4.1 Weibull Statistics 77

4.2 Probabilistic Design of Vessel 79

4.2.1 Cell Inner-Wall Modeled as Cylinder 80

4.2.2 Cell Top and Bottom Wall Modeled as Clamped Plate 82

4.2.3 Multiple Cells 83

4.2.4 Designing for the Weakest Cell 83

4.2.5 Final Design Selection 84

4.3 RHFS Test Data Reduction 85

4.3.1 Correlating RHFS Data to Pressure Vessel 86

4.3.2 Predictions for Pressure Vessel 91

4.3.3 Wafer-Scale Implications 92

4.4 Conclusions 92

5 Conclusions and Recommendations **95**

5.1 Summary of Usable Silicon Strength Work 95

5.2 Summary of Pressure Vessel Design Work 97

5.3 Contributions 97
5.4 Discussion 98
5.4.1 Improvements in Usable Silicon Strength 98
5.4.2 Further Comparison to Previous Work 99
5.4.3 Prospects for Further Research 100
5.4.4 Lessons Learned 100
5.5 Future Work 101
5.5.1 Tuning Etch Conditions 102
5.5.2 Experimental Evaluation of Pressure Vessel Features 102

A Detailed Si Pressure Vessel Calculations 103
A.1 Investigation of Designs from First Principles 103
A.1.1 Honeycomb Vessel 103
A.1.2 Concentric Tori Vessel 109
A.1.3 Wedge Vessel 114
A.1.4 Pancake Vessel 119
A.1.5 Conventional Vessel Geometries 126

B Fabrication Details and Etch Recipes for Radiused Hubbed Flexure Specimen 131
B.1 RHFS Fabrication Process Steps 131
B.2 Etch Recipes 134

C Error Analysis 135
C.1 RHFS Error Analysis 135
C.1.1 Geometry Error 135
C.1.2 Experimental Error 140

D Weibull Plots 143
D.1 RHFS Weibull Plots 143

E Experimental Evaluation of Pressure Vessel Features **153**

E.1 Pressure Vessel Coupon Design 153

E.2 Fabrication 153

E.3 Experimental Setup 155

E.4 FEM Modelling 155

F Mesh Sensitivity Studies **159**

F.1 RHFS Mesh Sensitivity Studies 159

F.2 PVC Mesh Sensitivity Studies 159

List of Figures

1-1 Image of drawn silicon boule[42] 23

1-2 Images of composite overwrapped pressure vessels from the ATK website 25

1-3 Plots of specific tank mass versus maximum vessel dimension for ATK vessels 26

1-4 SEM of sidewall scallops caused by DRIE etching[43] 27

1-5 Images of smoothed sidewall roughness on 15 μm high, 25 μm wide cylinder before and after hydrogen annealing taken from reference [25] 30

1-6 Illustration of pressure vessel integrated in launch stack 31

2-1 Diagram of the four compact vessel geometries considered. From left to right: pancake, concentric tori, honeycomb and wedge vessels respectively. 36

2-2 Honeycomb vessel cross-sections 36

2-3 Concentric tori cross-sections 37

2-4 Wedge cell and vessel cross-section 38

2-5 Illustration of pancake vessel cross-section 40

2-6 Cylinder vessel design 41

2-7 Conventional torus design 41

2-8 Comparison of first order silicon pressure vessel analysis 44

2-9 FEM results for honeycomb vessel 46

2-10 FEM results for concentric tori vessel in MPa 47

2-11 Comparison of second order silicon pressure vessel analysis 48

3-1 Illustration of RHFS geometry and testing procedures (not to scale) . 52

3-2 Illustration of die cross-section and mask through process 56
3-3 Illustration of RHFS masks 57
3-4 Cross-sections of RHFS showing inner hub wall and root 58
3-5 RHFS experimental setup 61
3-6 Procedure to align translating loader 62
3-7 Illustration of principal stress distribution in RHFS FEM model from a perspective below RHFS. 62
3-8 Comparison of RHFS results to previous RHFS results. 65
3-9 Failure stress distribution over wafer with omitted data represented by grey area 66
3-10 SEM images of various amounts of smoothing (10k magnification) . . 68
3-11 Distorted ion flux 68
3-12 RHFS trench sidewall 69
3-13 Inspection of sidewall at varying etch depths 70
3-14 Off center die (10.10) with various amounts of SF_6 (1k magnification) 71
3-15 Center die (7.7) root morphology with 0 minutes and 6 minutes of SF_6 (5k magnification) 72
3-16 SEM images of DRIE sidewall at different wafer locations 73

4-1 Illustration of cell cylindrical section 81
4-2 Illustration of cell plate section 82
4-3 Parameters for honeycomb vessel design with a 5 cc volume, failure probability of 10^{-8}, a design pressure $\leq$ 13 ksi, and for silicon strengths of 1 and 1.76 GPa 85
4-4 Failed RHFS where center hub has been detached 87
4-5 Weibull Distribution for 6 inch 650μm Thick Wafer with 1 minute SF_6 Smoothing and 112 Data Points 87
4-6 Noonan model for RHFS 89

4-7 Predictions for achievable silicon pressure vessel strength plotted with parameters for honeycomb vessel design with a 5 cc volume, failure probability of 10^{-8}, a design pressure $\leq$ 13 ksi, and for silicon strengths of 1 and 1.76 GPa 91

5-1 RHFS trench sidewall 95

A-1 Single honeycomb cell 104
A-2 Illustration of honeycomb vessel cross-section through wafer plane . . 105
A-3 Specific Tank Mass versus Cell # and Height for Honeycomb Design (varied volume and constant pressure) 107
A-4 Specific Tank Mass versus Cell # and Height for Honeycomb Design (varied pressure and constant volume) 108
A-5 Illustration of planer and through plane cross-sections of concentric tori vessel 109
A-6 Specific Tank Mass versus Cell # and Height for Concentric Tori Design (varied volume and constant pressure) 112
A-7 Specific Tank Mass versus Cell # and Height for Concentric Tori Design (varied pressure and constant volume) 113
A-8 Single wedge vessel cell 114
A-9 Plate model 115
A-10 $1/\sqrt{\beta}$ factor for various values of θ 116
A-11 Specific Tank Mass versus Cell # and Height for Wedge Design w/o Plate Section Model (varied volume and constant pressure) 117
A-12 Specific Tank Mass versus Cell # and Height for Wedge Design w/o Plate Section Model (varied pressure and constant volume) 118
A-13 Cross-section view of pancake vessel taken through the wafer plane . 119
A-14 Specific Tank Mass versus Cell # and Height for Pancake Design (varied volume and constant pressure) 125
A-15 Specific Tank Mass versus Cell # and Height for Pancake Design (varied pressure and constant volume) 126

A-16 Cross-section view of torus vessel 128

B-1 Illustration of die cross-section and mask through process 133

C-1 Percent error in σ_{max} estimate for various etch depth variation ± 30 μm. (Maximum load considered is maximum loader load ability) . . . 136

C-2 Nearly radially symmetric etch depth across 6" 650μm thick wafer with 1min SF_6 137

C-3 Cross-section views of hub root fillets at various radial wafer locations and circular fits 6" 650μm thick wafer with 1min SF_6 and oxide smoothing 137

C-4 Cross-section views of hub root fillets at various radial wafer locations and circular fits of 6" 650μm thick wafer with 1min SF_6 and oxide smoothing 138

C-5 Percent error in σ_{max} estimate by assuming fillet radius of 11 μm for actual fillets of 1-12 μm (Maximum load considered is maximum loader load ability) 138

C-6 Comparison of RHFS Data including variation due to varied fillet radius neglecting the effect of varied etch depth 139

C-7 Error in σ_{max} by using 650μm wafer data for a 450μm wafer 140

C-8 Simulated Weibull experiments estimate of error for varied data points 141

D-1 Weibull Distribution for 6 inch 650μm Thick Wafer with 1 minute SF_6 Smoothing and 112 Data Points 143

D-2 Weibull Distribution resulting from data binning for 6 inch 650μm Thick Wafer with 1 minute SF_6 and 55 Data Points 144

D-3 Weibull Distribution for 6 inch 650μm Thick Wafer with 1 minute SF_6 and Oxidation and 108 Data Points 144

D-4 Weibull Distribution resulting from data binning for 6 inch 650μm Thick Wafer with 1 minute SF_6 and Oxidation and 54 Data Points . . 145

D-5 Weibull Distribution for 4 inch 450μm Thick Wafer with 1 minute SF_6 and 42 Data Points 145

D-6 Weibull Distribution resulting from data binning for 4 inch 450μm Thick Wafer with 1 minute SF_6 and 20 Data Points 146
D-7 Weibull Distribution for 4 inch 450μm Thick Wafer with 1 minute SF_6 and 0.5 hours H_2 Annealing and 56 Data Points 146
D-8 Weibull Distribution resulting from data binning for 4 inch 450μm Thick Wafer with 1 minute SF_6 and 0.5 hours H_2 Annealing and 26 Data Points 147
D-9 Weibull Distribution for 4 inch 600μm Thick Wafer with 1 minute SF_6 and 2.5 hours H_2 Annealing and 52 Data Points 147
D-10 Weibull Distribution resulting from data binning for 4 inch 600μm Thick Wafer with 1 minute SF_6 and 2.5 hours H_2 Annealing and 22 Data Points 148
D-11 Weibull Distribution for 6 inch 500μm Thick Wafer with 6 minutes SF_6 and 71 Data Points 148
D-12 Weibull Distribution resulting from data binning for 6 inch 500μm Thick Wafer with 6 minutes SF_6 and 37 Data Points 149
D-13 Weibull Distribution for 6 inch 500μm Thick Wafer with 6 minutes SF_6 and Oxidation and 67 Data Points 149
D-14 Weibull Distribution resulting from data binning for 6 inch 500μm Thick Wafer with 6 minutes SF_6 and Oxidation and 35 Data Points . 150
D-15 Weibull Distribution for 6 inch 650μm Thick Wafer with 1 minute SF_6, Oxidation, and UHV and 68 Data Points 151
D-16 Weibull Distribution resulting from data binning for 6 inch 650μm Thick Wafer with 1 minute SF_6, Oxidation, and UHV and 29 Data Points 152

E-1 Illustration of PVC with cross-section taken through top portion to reveal inner geometry 154
E-2 Fabrication steps for PVC 155
E-3 Illustration of PVC experimental setup 156

E-4 Simplified model of o-rings as pins on PVC 156
E-5 Illustration of principal stress distribution in PVC FEM model with 2x exaggerated deformation 157

F-1 RHFS FEM mesh sensitivity 160
F-2 PVC FEM mesh sensitivity 161

List of Tables

1.1 Material properties of Si and aerospace materials[15, 1, 6] 23

3.1 Previous RHFS testing results 53

3.2 RHFS testing results 64

4.1 Comparison of RHFS A_{eff} Calculations with Noonan. 90

4.2 Variation in predicted pressure vessel strength across wafer for each RHFS data set 92

B.1 DRIE Recipe for RHFS 134

B.2 SF_6 Smoothing Etch Recipe for RHFS 134

Chapter 1

Introduction

Single crystal silicon is a material that has been developed for electronic applications. Single crystal silicon has promising inherent structural properties that are attractive for weight sensitive applications. This thesis explores the concept of using single crystal silicon as a structural material for macro-world structures with length scales of centimeters to tens of centimeters. It uses aerospace high pressure vessels as a focus application.

This chapter presents the properties of single crystal silicon that make it a favorable structural material and discusses current pressure vessel designs optimized for ductile metals. This chapter also presents the results of past researchers of structural silicon and silicon-based MEMS technology relevant to pressure vessel applications. This chapter concludes with a statement of research objectives.

1.1 Context

Single crystal silicon material offers favorable material properties and an unique alternative to conventional pressure vessels. In this section we will review the properties that make silicon such an attractive structural material. We will also review the state of current conventional pressure vessel designs.

1.1.1 Silicon Properties

Single crystal silicon is a material with theoretical strengths higher than steel and with a lower density than aluminum. This high strength, light weight characteristic of silicon make it an ideal structural material. Silicon however is a brittle material whose strength is sensitive to flaws that can arise during fabrication. The amount of volume flaws will increase as volume increases from a micro-scale to a macro-scale and surface flaws will increase as area increases as well.

Single crystal silicon has theoretical strengths between 15.2 and 22.4 GPa based on molecular bond strengths in the $< 110 >$ and $< 100 >$ crystal planes respectively.[23] In practice, measured silicon strengths tend to stay well below 10 GPa and tend to be in the range of a few GPa.[8, 31, 17] Similar single crystal materials such as germanium have achieved tensile strengths close to their theoretical strength in practice.[30] The achievement of germanium suggests that it may be possible for silicon to achieve more than ten gigapascals or a strength value close to its theoretical strength.

If single crystal silicon were able to reliably achieve even the high strengths that have already been demonstrated in practice, it would hold great promise as a structural material particularly for aerospace applications. Table 1.1 shows how silicon compares to conventional aerospace alloys of aluminum, titanium, and steel. We can see that silicon has a density close to and less than aluminum 2014-T6 with an ultimate strength, in some cases, 4 times higher than steel. This means that the strength to density ratio of silicon is about a order of magnitude higher than conventional aerospace materials.

The source of usable strength limitations in silicon is its brittle nature. For temperatures below 700 K, silicon behaves as a brittle material.[38] Failure in silicon at room temperatures will occur as fracture with no appreciable plastic deformation.[20, 32] As can be seen in table 1.1, silicon has a fracture toughness orders of magnitudes lower than the aerospace materials. Fracture toughness is a quantitative description of a material's ability to resist fracture. Silicon's fractures toughness is on the order of concrete.

Table 1.1: Material properties of Si and aerospace materials[15, 1, 6]

	Materials			
	Single Crystal Si	**2014-T6 Al**	**6Al-4V Ti**	**17-4 Steel**
Density [g/cm^3]	2.3	2.7	4.5	7.75
Ultimate Strength [MPa]	up to 9000	455	900	up to 1500
Strength/Density [MPa · m^3/kg]	up to 3.91	0.17	0.2	up to 0.19
Fracture Toughness [MPa·m$^{1/2}$]	∼0.9	19	up to 100	up to 100

Other important considerations for structural applications of single crystal silicon are high temperature capabilities. When silicon reaches a temperature above its brittle to ductile transition temperature, BDTT, (∼850 K) its strength is significantly reduced due to limitations from plasticity and creep. Between 700K and 850K silicon will display elastic-brittle behavior. Silicon has high chemical aggressiveness at elevated temperatures as well. Oxidation is a concern for silicon materials at elevated temperatures. Thermal oxidation on silicon for many hours at temperatures as high as 1200 K can produce oxides as thick as $5\mu m$, which can interfere in silicon systems with micron length scales.

Figure 1-1: Image of drawn silicon boule[42]

Demands for high purity single crystal silicon in the semiconductor industry have led to lower-cost, nearly defect free silicon samples. Development of silicon for semiconductor applications began in the 1940s. By the early 1950s silicon was formed with high levels of impurities due to its high chemical aggressiveness at high temperatures required for its preparation. In 1952, vertical zone melting was developed in which silicon rods are slowly melted from one end to another. Impurities would remain in the molten silicon region as

the past silicon region cooled until a large amount of impurities are collected at one end of the rod, which is cut off. Developments in the molten zone method led to improvements in silicon purity but eventually limits in the method itself made growing processes turn back to the Czochralski method which was actually developed originally in 1916. The Czochralski process begins with a seed of single silicon crystal drawn out of melted silicon so that the silicon crystals can align before the silicon cools and hardens into a boule. The Czochralski method is predominately used today for bulk silicon wafer production with improved levels of purity. An image of a finished boule is shown in figure 1-1. The resultant boule has a virtually defect free crystalline structure. The boule is then sliced into thin wafers that range between 300-1000 μm. Purity is important for strength because actual failure in silicon is the result of flaws or cracks in the material surface and bulk that grow under critical loading conditions.[44]

Silicon wafers can also be fusion bonded together with virtually no loss in strength due to the bond.[16] These silicon wafers can be made with diameters up to 12 inches. Given this manufacturing process, a silicon wafer begins its life virtually free of bulk flaws that lead to low strength. It is thus believed that the majority of flaws in a structure fabricated from a silicon is introduced mainly to the silicon surface from the fabrication process.

Section 1.2 will discuss previous work done towards removing flaws introduced from the fabrication process.

1.1.2 Conventional Pressure Vessels

Currently, conventional pressure vessel designs are not generally made with small volumes and thus are not optimal for such. There are penalties for trying to reduce the size of conventional pressure vessel designs. This is due to the fact that conventional pressure vessels are made with metal machining technology that is limited to few thousandths of a inch precision. In addition to the metal machining limitations, high pressure conventional vessels are often times reinforced with a composite overwrap such as those illustrated in figure 1-2. Threading of composite fibers becomes

increasingly difficult as the vessel size is reduced.

Commercial aerospace pressure vessels were investigated as part of the literature review for this project. The majority of data came from ATK PSI Operations, who are the largest manufacturer of propellant and pressurant tanks for the space industry. The following plots show the specific structural mass or mass ratio of the tanks (structure mass)/(pressurant mass) versus their longest dimension. The plot on the left of figure 1-3 is for all the ATK tanks and shows theoretical specific structural mass values based on the tank dimensions, design burst pressure q_{burst}, and theoretical material ultimate strength σ_u. The theoretical specific structural mass values are based on thin walled vessel theory which gives the following equations for wall thickness t based on ultimate strength σ_u and vessel dimensions:[45]

Figure 1-2: Images of composite overwrapped pressure vessels from the ATK website

$$t = \frac{q_{burst} r}{2\sigma_u}, \text{ for a sphere of radius r}$$

and

$$t = \frac{q_{burst} r}{\sigma_u}, \text{ for a cylinder of radius r with spherical end caps.}$$

The plot on the left of figure 1-3 seems to imply a trend of lower mass ratio with larger tank dimensions. The plots on the right show that this apparent trend disappears when the tanks are separated by monolithic tanks versus composite overwrapped tanks. This result indicates that there is no apparent advantage of conventional pressure vessel designs for small scale applications.

Other useful findings from conventional pressure vessel investigation are that the maximum operating pressures of the ATK vessels was at 8,000 psi achieved with a monolithic 6AL-4V titanium vessel with typical high end operating pressures of 4,000 psi. Also, the design factors-of-safety (FOS) used on these vessels ranged from 1.5 to 2.

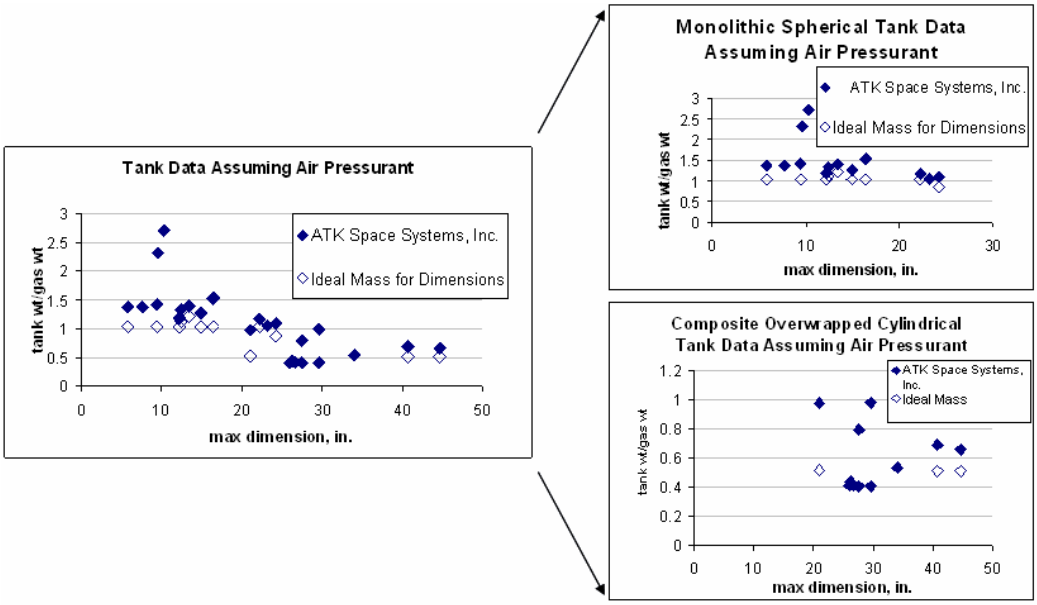

Figure 1-3: Plots of specific tank mass versus maximum vessel dimension for ATK vessels

1.2 Relevant Work and Motivations

As microeletromechanical systems (MEMS) have gained popularity, micro-scale silicon structural applications have emerged. On small scales, it is theoretically easier to make a silicon device free of larger defects because there is less area and volume that could contain flaws. Recent developments in silicon smoothing techniques lead to the belief that macro-scale structural silicon can also be achieved.

1.2.1 Structural Silicon MEMS

With developments in silicon fabrication methods there has been increased work in MEMS. One of the fabrication developments widely used in MEMS is the Bosch process, which allows the etching of deep trenches in a silicon wafer surface with straight sidewalls in a process called deep reactive-ion etching (DRIE).[36] The Bosch process is simply an alternation between an isotropic etch with some ions directed perpendicular to the wafer surface and a passivation step where the walls and bottom of the etched trench is coated with a polymer. The directional ions cause polymer to

be removed from the trench bottom and for the trench bottom to be etched while the sidewalls are mostly protected by the polymer. Although the trench tends to have an overall straight sidewall, it will have small-scale scallops due to the nature of the etch. An image the scallops formed are shown in figure 1-4. In addition to DRIE etching alone, DRIE etching combined with wafer to wafer bonding described in section 1.1.1 can create highly three dimensional silicon structures. Mechanical silicon structures include pressure transducers consisting of thin silicon membranes, microscale beams, and MEMS valves[18],[39, 21, 10],[7, 19]. More advanced structures include gears, turbine engines with rotating blades, and chemical rocket engines[12],[8],[31].

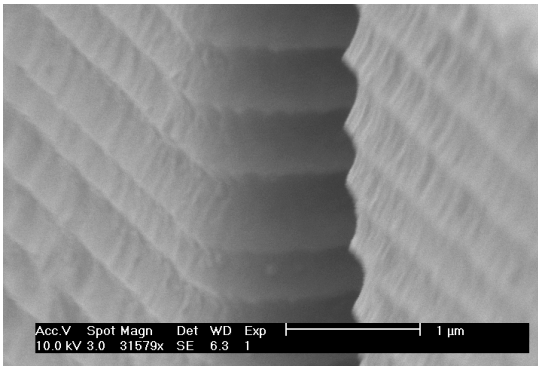

Figure 1-4: SEM of sidewall scallops caused by DRIE etching[43]

1.2.2 Work to Improve Silicon Strength

Some of the first investigations of steps to improve silicon wafer strength was done by S. M. Hu.[17] Hu looked at the effects of polishing, crystal orientation, ion implantation, quartz and polysilicon overlays, and annealing on silicon strength. Hu began with polished wafers, introduced damage to the surface by grinding the surface with grit of various particle sizes, and then attempted to repair the damage with polishing, ion implantation, overlays, and annealing. Hu found that chemo-mechanically polished (CMP) wafers with $< 100 >$ surface orientations achieved the highest strength with an average strength of 3 GPa. He also found that the surface treatment that led to the highest strength was argon implantation with annealing at 900°C in nitrogen

for one hour giving an average strength of 2.3 GPa.

Recent work done at MIT has led to even greater Si strengths through a variety of surface treatments. Unlike the work of Hu, the work at MIT used Weibull statistics to analyze silicon strength data. It is believed that the Weibull method is best for characterizing brittle material, in particular single crystal silicon.[10, 38] The Weibull method will be described in greater detail in section 4.1. The important results of the Weibull method are two parameters known as the characteristic strength σ_0 and the Weibull modulus m. The characteristic strength is an indicator of average strength defined as the strength at which the probability of failure is approximately 1/3 ($1/e = 0.37$). The Weibull modulus, m, is an indicator of the spread of strength values or distribution of flaw size. A higher value of Weibull modulus means a smaller spread of strength and flaw size and a higher reliability of the material under a given stress.

Kuo-Shen Chen was the first MIT researcher to investigate surface treatments to improve room temperature silicon strength.[8] Chen investigated the effects of two kinds of mechanical polishing, chemical polishing, KOH etching, and deep reactive ion etching (DRIE) on silicon wafers with $< 100 >$ surface crystal orientation. For these five surface treatments, Chen used the same kind of experimental setup used by Hu. His work found that the highest characteristic strength of $\sigma_0 = 4.6$ GPa was achieved by the DRIE etched surface with a respective low Weibull modulus of $m = 3.3$. The KOH etch did achieve a high Weibull modulus of $m = 7.2 - 12$ (range due to uncertainty in data) with a characteristic strength of $\sigma_0 = 3.5$ GPa.

Most MEMS devices are not made from silicon wafers with flat surfaces. A good deal of MEMS devices employ DRIE etching to make high aspect ratio trenches. In the interest of analyzing the strength of DRIE etched trenches and improving the resultant strength of a DRIE etch, Chen developed a strength test specimen named a radiused hubbed flexure specimen (RHFS). More details of the RHFS can be found in Section 3. For these specimens, Chen analyzed the effects of a wet enchant consisting of nitric acid (HNO_3) and hydrofluoric acid (HF) and a dry sulfur hexafluoride (SF_6) etch on silicon strength. Although both surface treatments improved the RHFS strengths,

the dry SF_6 etch improved the strength the most with a characteristic strength of $\sigma_0 = 4$ GPa and a respective Weibull modulus range of $m = 3.3 - 8.8$.

Further investigations of surface treatment effects on RHFS strength were done by Erin E. Noonan. Noonan examined the effects of varied DRIE recipes with and without SF_6 surface treatments on RHFS. Noonan showed some variation of silicon strength with varied DRIE recipes but found significant improvement in Weibull strength with SF_6 surface treatments with a respective decrease in Weibull modulus. Noonan also investigated the effects of varied DRIE recipes with and without SF_6 surface treatments on pressurized silicon pressure vessels. Noonan's work also incorporated stress concentration factors associated with the corner fillet radius of both the RHFS and pressure vessels which resulted in higher characteristic strength and Weibull modulus results. Noonan achieved the highest characteristic strength of silicon found through Weibull methods of $\sigma_0 = 8.821$ GPa with a Weibull modulus less than 3, $m = 2.572 - 2.693$. Noonan's results found that with high characteristic strengths, samples had lower Weibull moduli.

1.2.3 Motivations

Previous work done with surface treatments to improve silicon strength have had one important feature in common. That common trait is that large values of characteristic strength σ_0 come with a decreased value of Weibull modulus m and vise-vera. In other words, improvement of average silicon strength has always come at the cost of high variability in the strength value. Perhaps it is possible that silicon surface treatments either repaired or reduced the size of surface flaws in the silicon while introducing a larger variety of small size flaws. It is believed that if it were possible to repair surface flaws in silicon completely without introducing new flaws or new flaw sizes, one could produce a silicon device with high silicon strength with a low variability.

Recent work has been done in a field known as hydrogen annealing also referred to as surface migration which shows promise for repairing surface damage to silicon in such a way as to improve silicon strength and Weibull modulus. Initial research revealed that an atmosphere of low pressure between tens to hundreds of

Torr hydrogen gas at a high temperature around 1000°C or greater for a period of time between a few seconds to a few minutes could actually transform the shape of silicon trenches from a rough rectangular shape to a smooth rounded shape.[35] It is believed that the cause of this shape change is due to the migration of surface atoms in the silicon to lower energy states. Surface migration has been shown to remove scallops formed by the DRIE Bosch process as shown in figure 1-5.[24, 25] It was previously believed that a reducing atmosphere such as hydrogen was necessary to remove native oxide on the silicon surface that might inhibit surface migration. Recent work at Stanford has measured actual migration rates and shown that surface migration can occur in nonreducing inert gas environments such as helium, neon, argon, and nitrogen. It is believed that this work could lead to improved silicon strength and reliability.

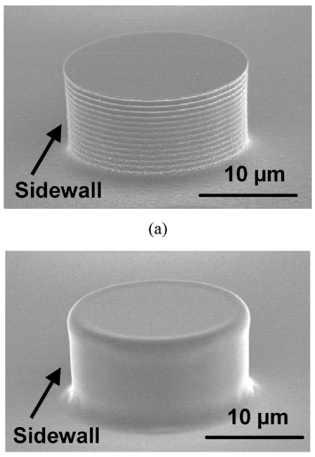

Figure 1-5: Images of smoothed sidewall roughness on 15 μm high, 25 μm wide cylinder before and after hydrogen annealing taken from reference [25]

The potential of single crystal silicon's inherent structure and the promise of surface migration techniques lead to the hypothesis that high strength macro-scale silicon structural applications may be achievable. The promise of high strength macro-scale silicon make it a good candidate for aerospace high pressure vessels . A single crystal silicon high pressure vessel is advantageous for a number of reasons that can have multiple applications.

As the size of satellite payloads are reduced, so are the weight and size of the launch vehicles putting those payload into orbit. An example of small payloads is the development of the CubeSat done between California Polytechnic State University and Stanford University to develop a 10 cm cubic picosatellite with a weight of no more than one kilogram.[14] As payloads sizes decrease, so does the need for fuel pressurization.

A simple alternative to the small scale pumps are small scale silicon pressure vessel whose flat, wafer shapes could conceivably fit compactly in a cylindrical launch vehicle design. Figure 1-6 illustrates how the pressure vessel would fit into a launch system. An advantage of a silicon pressure vessel design is that the associated valves and control circuit could be integrated on-chip. Silicon micro-valves have already been investigated.[7, 19] Silicon's inherently high strength to density ratio would make it possible to make a light-weight pressure vessel, an important consideration for space systems. The unique fabrication methods that exist for single crystal silicon avoid the complications mentioned in section 1.1.2 with reducing the size of conventional pressure vessels.

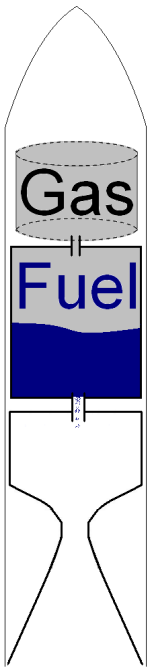

Figure 1-6: Illustration of pressure vessel integrated in launch stack

Other applications of silicon pressure vessels are those where a conventional pressure vessel would be needed on smaller scales. All the advantages that the silicon pressure vessel has to pressurize fuel for an earth-to-orbit launch vehicle would also be advantageous as an in-space cold-gas rocket. A cold-gas rocket system is merely one where the pressure vessel is directly connected to a rocket nozzle. Again, a small scale silicon pressure vessel cold-gas rocket could have control circuits and valves integrated on chip. Another possible application of small scale silicon high pressure vessels could be to inflate car airbags. Current airbag inflation systems involve the decomposition of a highly toxic propellant. Using an inert high pressure gas for airbag inflation could avoid the possible complications of having toxic propellant. Again, with a microfabricated silicon pressure vessel, necessary accelerometers and control circuits could be packaged on-chip.

1.3 Research Objectives

Single crystal silicon has excellent mechanical properties and is now widely available in high quality. This research attempts to find out if these properties can be exploited for macro-scale aerospace structural applications. This research seeks to find the combination of properties, fabrication methods, and design approaches needed for single crystal silicon to be useful.

To explore these topics, this research is broken into two separate research objectives, this thesis has a scientific objective and an engineering objective. The scientific objective of this research is **to explore the use of micro-machined single crystal silicon as a macro-world structural material in order to understand its advantages and limitations**. The engineering objective of this research is **to use the aerospace pressure vessel application as a proof of concept that properly fabricated single crystal silicon can be used for a useful macro-world structure**.

This thesis is structured as to primarily explore the engineering objective with an analytical design of a silicon pressure vessel. The thesis then explores the scientific objective through literature review, fabrication work, and experimental work. The final research portion of this thesis will tie together the findings of both sections into and fabrication and experimental exploration of silicon pressure vessels. Chapter 2 describes the design process for a microfabricated Si high-pressure vessel. Chapter 3 describes experimental work using a Radiused Hubbed Flexure Specimen (RHFS) to analyze the effect of various fabrication techniques on silicon strength. Chapter 4 uses probabilistic design to integrate silicon's brittle nature into pressure vessel design and correlate between material tests and expected pressure vessel behavior. The final chapter makes concluding remarks on the research and recommendations for future research.

Chapter 2

Design of a Silicon Pressure Vessel

This chapter describes the analytical and computational analysis of various single crystal silicon pressure vessel designs. The silicon pressure vessel designs were chosen arbitrarily attempting to explore the possible variations in silicon pressure vessel design. The results of the analysis are compared with traditional titanium pressure vessel designs and a best design is chosen from those analyzed based on design criteria described herein.

2.1 First Order Investigation of Silicon Designs

This section analytically describes four single crystal silicon pressure vessel geometries and three conventional titanium pressure vessel geometries for the purpose of comparing both specific structural volume quantities ((structure volume)/(internal volume)) and specific structural mass quantities or inverse storage efficiency ((structure mass)/(pressurant mass)) versus design pressure for the same internal volume. The first four vessels described are variations of a short and wide cylinder or hollow disk. They are intended to model vessels microfabricated in silicon designed to minimize the packaging length of the vessel or the area it occupies. The following three vessels described are typical spherical, cylindrical, and toroidal vessel geometries with the same volume fabricated in a typical vessel material of titanium. These vessel descriptions are followed by a scaling used to go from specific volume quantities

to specific mass quantities for either a silicon or titanium vessel. The final subsection contains plots of specific volume and specific mass and an explanation of the resulting curves.

The following design criteria were developed based on applications to small and very small spacecraft propulsion, a microlaunch vehicle with a diameters of 4-8", and typical reliability demands of aerospace systems:[22]

- minimize specific structural mass of vessel, $\frac{M_{tank}}{M_{gas}}$
- 50-500 psi operating pressures in external connections
- 8-15 ksi tank design pressure
- Weibull characteristic strengths in the GPa range
- vessel reliability of $10^{-6} - 10^{-8}$
- design compatible with existing microfabrication techniques

The first design criteria is based on the fact that minimizing mass is an important restriction for aerospace applications since more mass to launch requires more propellant. Minimizing packaging length of the vessel and its associated structure is beneficial at a vehicle level. We design for an outlet pressure between 50-500 psi, because this is typical of pressurization needs of rocket engines. A vessel reliability of 10^{-8} is a minimum for most aerospace applications.

2.1.1 Silicon Vessel Designs

An assumption underlying this work is that silicon pressure vessels can be fabricated from available single crystal material using existing microfabrication techniques. This technology has been developed to fabricate mainly 2-D planar features with depths of a millimeter or less on 10-30 cm diameter Si wafers. Thicker structures can be assembled by bonding wafers together without loss of material strength. Most aerospace high pressure vessels are spherical or cylindrical. Spheres of multi-centimeter diameter are beyond the state-of-the-art of microfabrication, as all but very short, wide

cylinders can be made with microfabrication. (Short, wide cylinders can be advantageous in vehicle integration, but this is not considered here.) Since short cylinders with flat plate ends are inefficient structurally, geometries that exploit the ability to fabricate relatively shallow but complex in-plane, extruded-like geometries are considered. In this section, we address the question as to whether the combination of superior strength and complex geometry can compensate for structural inefficiency.

Four silicon vessel geometries representing variations of a short and wide cylinders or hollow disks were analyzed and compared to conventional spherical, cylindrical, and toroidal vessel designs. Figure 2-1 shows the four vessels considered. The leftmost "pancake" vessel is short and wide with no internal structure. The pancake vessel diagram shows a cross-section of the vessel taken perpendicular to the wafer plane surface. The second vessel from the left, a "concentric tori" vessel consists of a sphere surrounded by tori with increasingly larger major diameter. The concentric tori diagram shows a cross-section taken along the wafer surface plane above a cross-section of the vessel taken perpendicular to the wafer surface plane. The third, "honeycomb", vessel consists of spherically capped cylinder cells arranged in a honeycomb pattern. The honeycomb vessel diagram shows a cross-section taken along the wafer surface plane above a cross-section of the vessel taken perpendicular to the wafer surface plane. The rightmost, "wedge" vessel has a spoke-like internal structure which form flat wedge shaped cells. The wedge vessel diagram shows a individual wedge cell above a cross-section of the vessel taken perpendicular to the wafer surface plane. Basic thin shell theory has been used to calculate wall thicknesses needed to construct the various vessels. This theory is accurate for vessels with diameters at least 10 times larger than the wall thickness.[5] Geometry parameters were varied to find a vessel design that minimizes the specific structural mass ((mass of structure)/(mass of gas)) of a vessel. Because the vessel walls are considered to be thin, the stresses and deformations in the vessels are determined by considering the entire complicated shell as a combination of simple elements (cylinder, sphere and triangular flat plate) using membrane solution methods. This analysis is almost identical to the more accurate but complicated bending theory methods with the exception of a narrow strip on the

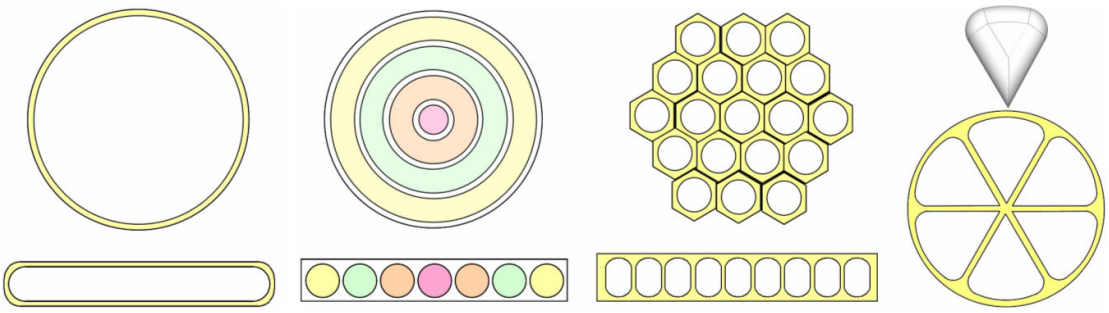

Figure 2-1: Diagram of the four compact vessel geometries considered. From left to right: pancake, concentric tori, honeycomb and wedge vessels respectively.

shell surfaces adjacent to the boundary.[3, 45]

The pressure vessel analysis is presented in order of complexity of the analysis. The sections begin with the more simple designs of the honeycomb vessel and concentric tori vessel and finishes with the more complex analysis of the wedge vessel and the pancake vessel. These analytical descriptions are brief but more detailed calculations can be found in appendix A.

Honeycomb Vessel

This honeycomb vessel analysis consists of thin walled cylinders with spherically capped ends. The cylinders are arranged in a honeycomb pattern with the space in between filled with material. The illustration to the right shows a cross-section perpendicular to the vessel longitudinal direction and longitudinal cross-section. The minimum wall thickness between each cylinder is determined by the material stress relations for a thin-walled cylinder. The cells were arranged so that symmetry is preserved. The construction of the honeycomb begins with a single cell that is then surrounded by layers of cells. Figure 2-2 shows three layers of cells.

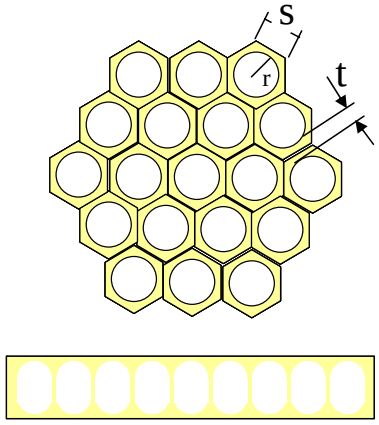

Figure 2-2: Honeycomb vessel cross-sections

Given n layers of cells, we can determine the total number of cells C. The minimum wall thickness between cells can be found assuming thin walled cylinders with spherical end caps which gives:

$$t = \frac{q_{burst} r}{\sigma_f} = FOS \frac{q_{design} r}{\sigma_f} \tag{2.1}$$

where q_{burst} is the maximum internal pressure the vessel can withstand, r is the cell cross-sectional radius, σ_f is the fracture strength of the silicon, FOS is the vessel factor-of-safety, and q_{design} is the maximum operating pressure of the vessel such that $q_{burst} = FOS q_{design}$.[45]

Given relation 2.1, the ratio of structural and internal volume of the vessel in terms of design pressure, dimensions, and material strength can be found. Section 2.1.3 will describe how we can use the volume ratio to determine mass ratio. This ratio can then be used to determine optimal dimensions for a given internal pressure and volume.

Concentric Tori Vessel

This vessel analysis consists of a center spherical tank or radius surrounded by n toroidal tanks such that:

$$r = b_1 = b_2 = b_3$$

where b_i represents the minor radius of each ith torus. Figure 2-3 shows a cross-section perpendicular to the vessel longitudinal direction and longitudinal cross-section. The minimum wall thickness of each cell is determined by the material stress relations for a thin-walled sphere for the center cell and for a thin-walled torus for the

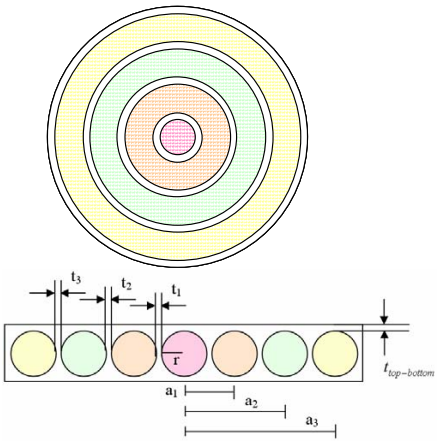

Figure 2-3: Concentric tori cross-sections

other cells as:

$$\begin{aligned} t_{sphere} &= FOS\frac{q_{design}r}{\sigma_f} \\ \text{and} & \\ t_{torus} &= FOS\frac{q_{design}b}{2\sigma_f}\frac{2a-b}{a-b} \\ &= FOS\frac{q_{design}b}{2\sigma_f}\frac{2a-r}{a-r} \end{aligned}$$

where t is the wall thickness for the cell shapes named in the variable subscript, a is the major radius of each toroidal cell illustrated in figure 2-3, r and b are the cell cross-sectional/minor radius, σ_f is the fracture strength of the silicon, FOS is the vessel factor-of-safety, and q_{design} is the maximum operating pressure of the vessel.[45] Given this relation, we can calculate the ratio of structural and internal volumes of the vessel in terms of material strength. Section 2.1.3 will describe how we can use the volume ratio to determine mass ratio. This ratio can then be used to determine optimal dimensions for a given internal pressure and volume.

Wedge Vessel

This tank structure consists of a short cylindrical vessel with triangular wedge sections. Each wedge shaped cell is formed by 3 semi-cylindrical edges (one of which is curved along the tank edge) joined at three corners with 3 spherical arcs closed by 2 flat triangular plates on the top and bottom of the cell. The stresses and deformations in the cells can be determined by considering the entire complicated shell as a combination of simple elements (cylinder, sphere and triangular flat plate) using membrane solution methods. This analysis is almost identical to the more accurate but complicated bending theory methods with the exception of a narrow strip on the shell surfaces adjacent to the boundary.[3] The illustration in figure 2-4 shows a single

Figure 2-4: Wedge cell and vessel cross-section

vessel cell above a cross-section perpendicular to the vessel longitudinal direction

Each cell fits inside the pancake cylinder exterior and has edges flush to a circular wedge with vertex angle 2α. Angle α is determined by the number of cells desired C such that:

$$\alpha = \frac{\pi}{C}$$

Wall thickness is determined by the maximum stress in the cell structure which is either caused by the hoop stress in the cylindrical sections, the stress in the spherical section, or the stress in the triangular plate section. For conditions where the vessel radius, R, is more than 10 time larger than the radius, r, for the cylindrical and spherical cell sections, the plate section stresses will dominate the cell wall thickness (see appendix A for more detailed calculations). The plate wall thickness is determined by the following equation:

$$t_{triangularplate} = R \cdot FOS \sqrt{\frac{3q_{design}}{2\sigma_f} \frac{\sin^2 2\alpha}{1 + 2\cos^2 2\alpha}}$$

where t is the wall thickness for the cell shapes named in the variable subscript, R is the major radius of the vessel, σ_f is the fracture strength of the silicon, FOS is the vessel factor-of-safety, and q_{design} is the maximum operating pressure of the vessel.[45]

Given this relation, we can calculate the ratio of structural and internal volumes of the vessel in terms of material strength and determine optimal dimensions for a given internal pressure and volume.

Pancake Vessel

This vessel consists of the outer cylindrical, circular part of a toroidal vessel with two flat circular plates capping the top and bottom. Figure 2-5 illustrates a view into the vessel from a cross-section taken through the vessel. Again, the stresses and deformations in the vessel can be determined by considering the shell as a combination of simple elements using membrane solution methods. This analysis is almost identical

to the more accurate but complicated bending theory methods with the exception of a narrow strip on the shell surfaces adjacent to the boundary.[3] Wall thickness is

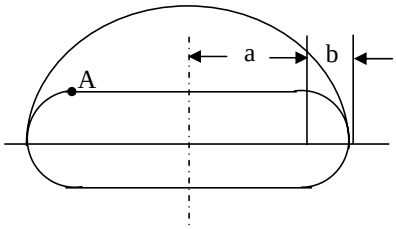

Figure 2-5: Illustration of pancake vessel cross-section

determined by the maximum stress which occurs either in the torus section or in the plate section. The maximum stress in the torus section will occur at point A on the toroidal section as shown in figure 2-5 and is equal to:

$$\sigma_{toroidalsection} = FOS\frac{q_{design}b}{t}$$

where b is the cell minor radius illustrated on figure 2-5.[45] The maximum stress in the plate section also occurs at point A and is proportional to:

$$\sigma_{plate} = \frac{1}{t_{plate}^3}$$

So the wall thickness of this vessel should be determined by the following relation:

$$t = \max\left(FOS\frac{q_{design}}{\sigma_{material}}, t_{plate}\right)$$

Given this relation, we can calculate the ratio of structural and internal volumes of the vessel in terms of material strength and determine optimal dimensions for a given internal pressure and volume.

2.1.2 Conventional Vessel Designs

The silicon pressure vessel designs presented in the last subsection are compared with the typical pressure vessel shapes which are a spherically capped cylinder, a sphere,

and a torus/tube. The designs are considered as monolithic titanium vessels without composite overwrap.

Cylinder

A cylindrical pressure vessel typically consists of a cylinder with spherical hemispheres on each end. The maximum stress in the vessel can be attributed to the hoop stress in the cylindrical portion of the vessel which is twice that of the spherical portion. The stress relation between stress and and wall thickness is:[45]

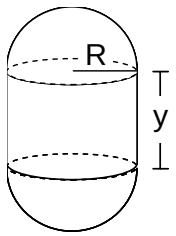

Figure 2-6: Cylinder vessel design

$$t_{cyl} = FOS\frac{q_{design}R}{\sigma_f}$$

where R is the radius of the vessel.[45]

Sphere

As mentioned previously, the wall thickness for a sphere with no cylindrical parts will be half that of the cylinder hoop stress. Thus, the wall thickness of the cylinder is determined by:

$$t_{sph} = FOS\frac{q_{design}R}{2\sigma_f}$$

where R is the radius of the vessel.[45]

Torous/Tube

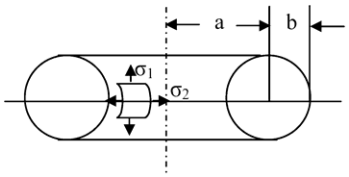

Figure 2-7: Conventional torus design

A toroidal vessel will have a maximum stress similar to the hoop stress in the cylindrical vessel. The max stress is represented by the σ_1 stress illustrated on figure 2-7. This stress can be related to wall thickness by:

$$t_{tor} = FOS \frac{q_{design} b}{2\sigma_f} \frac{2\frac{a}{b} - 1}{\frac{a}{b} - 1}$$

where a is the major radius of the vessel and b is the minor radius of the vessel illustrated in figure 2-7.[45] We can see that if we simply wanted to analyze a tube and let the major radius go to infinity such that $\frac{a}{b} >> 1$, the wall thickness equation for the torus will reduce down to that of a cylinder.

2.1.3 Final Comparison of Analytical Analysis

In this subsection the mass ratio of the vessels presented are compared. In the previous subsection information was given to determine the specific structural volume quantities ((structure volume)/(internal volume)). A scaling factor to determine mass ratio and the results of the the analysis are presented in this subsection.

Vessel Volume to Mass Scaling

The mass efficiency of a pressure vessel is an important figure of merit not only for this research's design criteria but also for general pressure vessel design. Finding volume ratios between the tank material and internal space can be done with the relations from the last subsection. To convert the volume ratio to a mass ratio the following equation is used:

$$\begin{aligned} \frac{M_{tank}}{M_{gas}} &= \frac{V_{tank}}{V_{gas}} \frac{\rho_{tank}}{\rho_{gas}} \\ &= \frac{V_{tank}}{V_{gas}} \frac{\rho_{tank} R_{gas} T_{gas}}{q_{design}} \end{aligned} \tag{2.2}$$

This equation produces a conversion factor with an inverse dependence on design pressure. This inverse dependance on pressure causes the mass ratio versus design pressure of the multi-cell vessels to have a parabolic shape with positive curvature.

The volume ratio for both the multi-cellular and single-cell vessels are polynomial functions of design pressure. The volume ratio equation for the multi-cellular vessels have a constant in the polynomial while the single-cell vessels does not. For this reason, the inverse dependance on pressure of the volume to mass conversion factor will force the mass ratio to a minimum as pressure is increased as can be seen in figure 2-8

Comparison of results

The relations for mass determined in the previous subsections were used to compare all the silicon vessel designs to the standard vessel designs made out of titanium for a constant volume and varying design pressure. Figure 2-8 assumes a maximum silicon stress of 1,000 MPa and a maximum titanium stress of 600 MPa with a 1.5 factor-of-safety. Only the specific tank mass for vessels with wall thickness $t < 10L$ are plotted to satisfy the thin-walled shell assumptions.[5] In this case L represents the smallest internal dimension for example $L = 2b$ for the pancake geometry. The largest obtainable pressure for each tank design so that the thin-walled assumptions are met are indicated with a •.

The plot uses geometry parameters which reduce specific structural tank mass. The titanium vessels are compared to the silicon vessels with quasi-optimum designs. These quasi-optimal designs are determined by exploring the effect of geometry, volume, and pressure variation on specific structural mass. This exploration resulted in a few notable points about each vessel. The honeycomb specific structural mass decreases with increasing cell height. The specific structural mass of the honeycomb vessel decreases with increasing cell number. Structural mass of the concentric tori vessel decreases with increasing cell number but this decrease is small for cell numbers greater than ∼7,000. Increased cell numbers for the wedge vessel caused an increase in structural mass while tank radius values of a few millimeters results in constant structural mass values. For the pancake vessel, a lower aspect ratio, approaching a spherical shape, provides lower mass ratios. Thus, the pancake vessel design with high aspect ratios is suboptimal. The way these quasi-optimal designs were determined

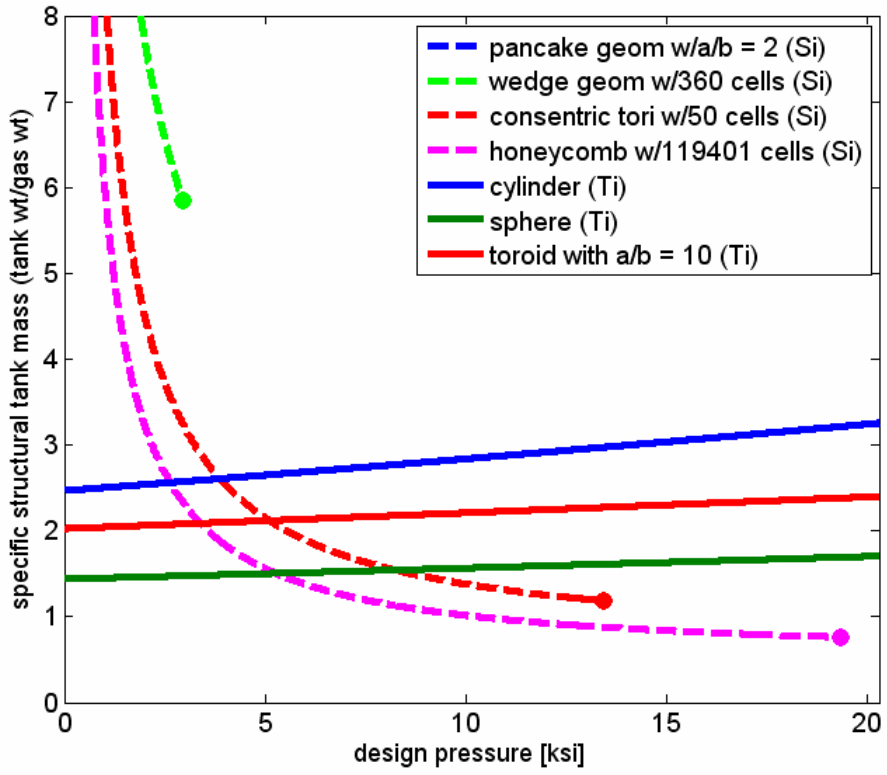

Figure 2-8: Comparison of first order silicon pressure vessel analysis

are further explained in appendix A.

The results of this analysis shows that the honeycomb and concentric tori silicon pressure vessels have lower specific tank masses than conventional vessels at internal tank pressures above 5,000 psi. The pancake vessel design had high stresses for the parameters explored on figure 2-8 and thus had a mass ratio outside of plot. Internal structure is necessary in a compact vessel design and for this reason the pancake vessel design is not considered beyond the first order design phase. The wedge vessel design had higher mass ratios than the honeycomb and concentric tori designs and did not show mass ratios lower than the titanium vessel designs before the thin-wall assumptions broke down. Thus, the wedge vessel design is not considered a strong candidate for the silicon pressure vessel design.

2.2 FEM Refinement of Designs

The finite element modeling (FEM) software ABAQUS was used for second order calculation of stresses in the silicon vessel designs. This analysis was used to verify the results of the first order analysis and give more accurate results for designs more consistent with microfabrication technology than those analyzed in the first order analysis. The vessel geometries were varied to achieve lower stress gradients over the vessels as well as make more realistic microfabricated vessel designs. This analysis assumed a 13 ksi design pressure and a total vessel volume of 10 mm^3. The maximum stress predicted by the conceptual design was limited to 1 GPa with a 1.5 factor-of-safety. With this design stress limit and factor-of-safety, the design was limited to a principal stress no greater than 666 MPa. Maximum principal stress is analyzed to determine failure stress because this is typical for brittle materials and silicon is a brittle material at room temperature.[34]

2.2.1 FEM Evaluation of Honeycomb Vessel

The FEM model for the honeycomb vessel was done with only two layers of cells all pressurized to 13 ksi. Only half of the vessel was modeled cut about the longitudinal cross section with a symmetry boundary condition at that surface. The initial honeycomb design was cylinders arranged in a honeycomb pattern with the space in between filled with material. This initial model was designed to have a maximum stress of 666 MPa (1 GPa with a factor-of-safety of 1.5). This design had a maximum von Mises stress of 960 MPa. Then a lean design without cross section fillets was modeled. This design had large stresses at the sharp corners but only had von Mises stress of about 1 GPa everywhere else. Given this result the sharp corners were filleted, the cell walls there thickened and the end caps were modeled as an etch instead of a revolution. Fillets of $r/2$ and $3r/4$ were considered where r is the spherical cap radius of the initial cell design. Inner wall thicknesses of t, $1.1t$, $1.5t$, and $1.75t$ were considered where t was the initial inner wall thickness of the design. Outer wall thicknesses of t_{out}, $2t_{out}$ and $3t_{out}$ were explored where t_{out} was the initial outer wall

thickness of the design. The final result had a maximum principal stress of nearly 666 MPa (673 MPa) and is shown in figure 2-9. With a $3r/4$ fillet radius, a scaling of $1.75t$ for the inner walls and $3t_{out}$ for the outer walls, relates the first principal theory to the FEM refinement.

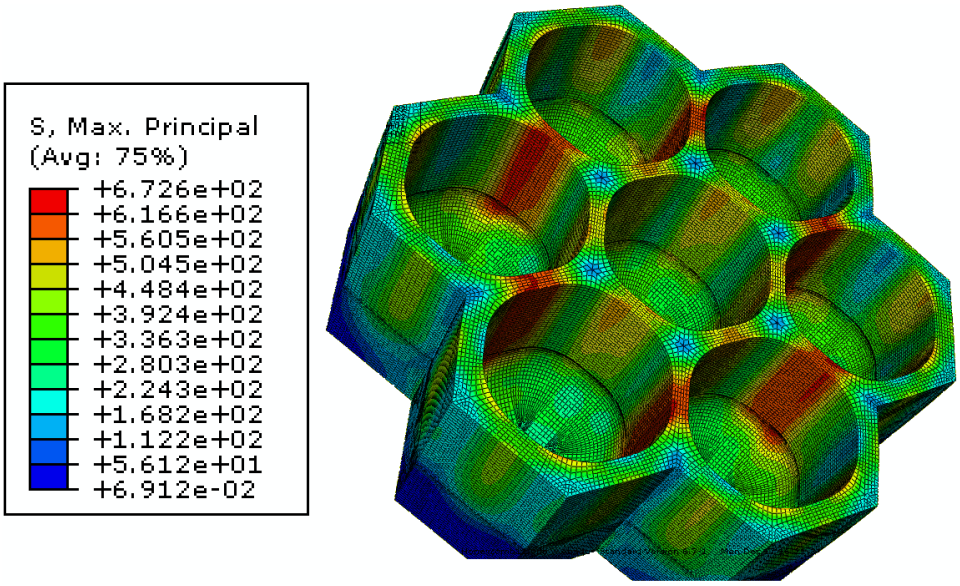

Figure 2-9: FEM results for honeycomb vessel

2.2.2 FEM Evaluation of the Concentric Tori Vessel

The FEM model for the concentric tori vessel was done with only seven layers of cells all pressurized to 13 ksi. Only a quarter of the vessel was modeled cut about perpendicular latitudinal cross sections with a symmetry boundary condition at those surfaces. The initial concentric tori design was a center spherical tank surrounded by toroidal tanks such that the spherical radius is equal to the minor radius of the torus vessels. This initial model was designed to have a maximum stress of 666 MPa (1 GPa with a factor-of-safety of 1.5). This design had a maximum von Mises stress of 1,364 MPa. Then a lean design without cross section fillets was modeled. This design had large stresses at the sharp corners and everywhere else. Given this result the sharp corners were filleted and the cell walls were thickened. Fillets of $r/2$ and $3r/4$ were considered where r is the minor radius of the initial cell design. Inner wall

thicknesses of t, and $1.5t$ were considered where t was the initial inner wall thickness of the design. The outer wall thicknesses t_{out}, was not varied.

Even with a fillet of $3r/4$ and $1.5t$ inner cell wall thickness, the refined design had higher stresses than the original design with a circular cross section and thinner interior walls. The final result with $1.5t$ inner cell wall thickness and a circular cross section is shown in figure 2-10. This model has a maximum von Mises stress of 1,038 MPa. The comparison of this final design with conventional vessels is shown in the plot below. A vessel with fillets less than the cell radius does not handle stress as well as cells with a circular cross section. Producing circular cross sections with microfabrication, however, is difficult.

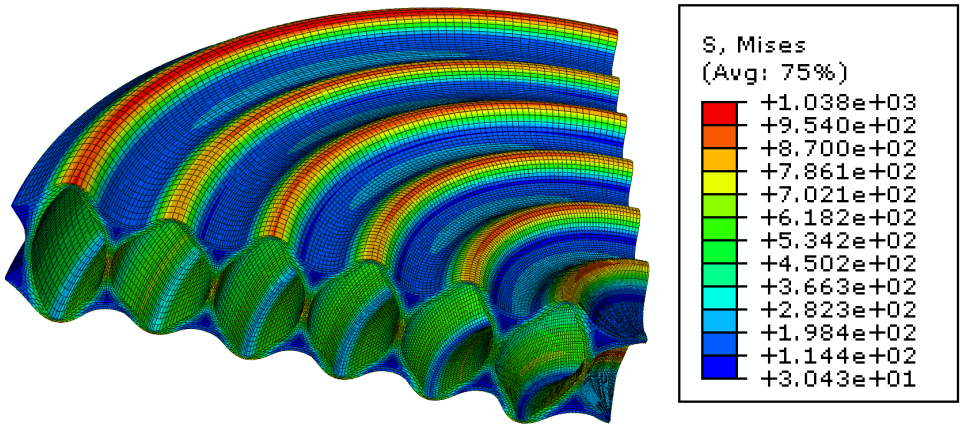

Figure 2-10: FEM results for concentric tori vessel in MPa

2.2.3 FEM Evaluation of the Wedge Vessel

The stresses in the wedge vessel geometry realized using the FEM software had unacceptable deflections and stresses, too large to make this design a viable choice for a vessel with a small aspect ratio and so is not included.

2.2.4 Results of FEM Analysis

The changes in storage efficiency caused by changes in vessel geometry were accounted for in a comparison plot like that from the section 2.1. Scaling factors determined by

the FEM analysis were applied to the analytical equations allowed the comparison of the final designs that are shown in the plot in figure 2-11. The effect of changing the cell fillet radii (which would remove material from the spherical/circular model of the cell) on specific structural mass is not included on this plot meaning, there is a slight overestimate of specific structural mass by assuming spherical shapes as opposed to filleted corners. The plot assumes a maximum silicon stress of 1,000 MPa and a maximum titanium stress of 600 MPa both with a 1.5 factor-of-safety. Only the specific tank mass for vessels with wall thickness $t < 10L$ are plotted to satisfy the thin-wall assumption. In this case L represents the smallest internal dimension. The largest obtainable pressure for each tank design so that the thin walled assumptions are met is indicated with a •. We see that at 13 ksi the honeycomb geometry still has a lower inverse storage efficiency than the conventional vessel designs. The thicker walls on the concentric tori vessel do not satisfy the thin wall assumptions at 13 ksi. These results make the honeycomb vessel design the best choice of the geometries analyzed.

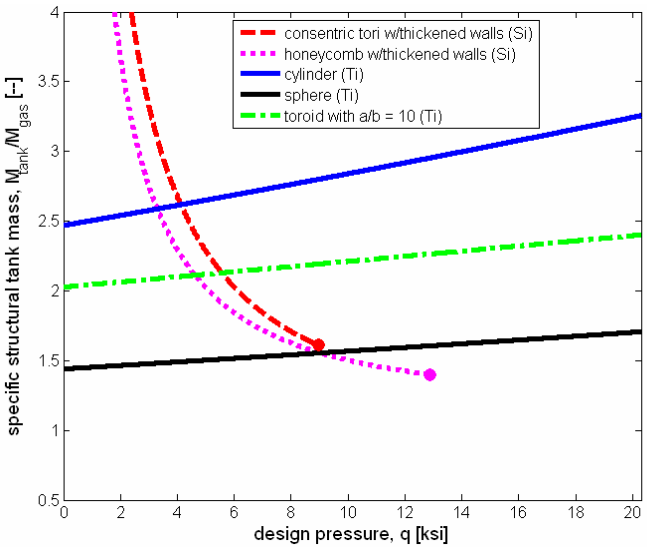

Figure 2-11: Comparison of second order silicon pressure vessel analysis

2.3 Conclusions

This chapter explored stress distributions and specific mass ratios for four microfabricated single crystal silicon pressure vessel designs with first order stress calculations and finite element modelling (FEM). The designs were chosen arbitrarily trying to explore the space of possible designs with design criteria described in section 2.1. The specific mass ratio of the silicon pressure vessel designs were compared with that of conventional pressure vessel geometries made of titanium. The results of the analysis shows that the fundamental hypothesis of this research, that the superior mechanical properties of single crystal silicon can result in silicon pressure vessels which are superior to conventional designs, is only true for design pressures above 5000 psi or more. The geometric limitations of microfabrication which limit the reduction of silicon pressure vessel mass can only be overcome by the superior mechanical properties of silicon material for tank pressures perhaps well above 5000 psi. This result is based on material density and geometry considerations assuming a maximum stress of 1 GPa can be reliability achieved in the silicon vessel. Strength and reliability capabilities of the silicon vessel design will be explored in the following chapters.

Chapter 3

Exploring Usable Silicon Strength with Radius Hubbed Flexure Specimens

This chapter describes experimental work using a radiused hubbed flexure specimen (RHFS) to explore the usable strength of silicon for wafer-scale structural applications and explore the effect of strength recovering techniques. Previous work with RHFS is presented. The device fabrication, modelling, and testing are described. Results from RHFS tests are presented and discussed.

3.1 Radius Hubbed Flexure Specimen Background

The radiused hubbed flexure specimen (RHFS) was developed by Chen to study degraded surfaces on horizontal-vertical transitions in silicon.[8] This same specimen design was also used by Noonan later to analyze strength recovering surface smoothing techniques.[31] The geometry of the RHFS is illustrated in figure 3-1(a). It is simply a square centimeter die of silicon with a toroid shaped well DRIE etched into it. The result is a hub located in the center of the die surrounded by a donut-shaped pit. The thickness of the sample is shown as 650 μm in figure 3-1(a) but this value actually varied between 400 μm and 650 μm in current and previous research. The membrane

thickness that remained after etching was always 150 μm. All other dimensions did not vary. The sample is tested by a load applied to the center of the side of the die that does not have the deep toroid trench. The die is situated on a 7 mm diameter hole in an aluminum holder. The test setup is illustrated in figure 3-1(b). This kind of loading produces a axisymmetric stress distribution with a stress concentration at the hub root at the inside bottom of the DRIE etch.

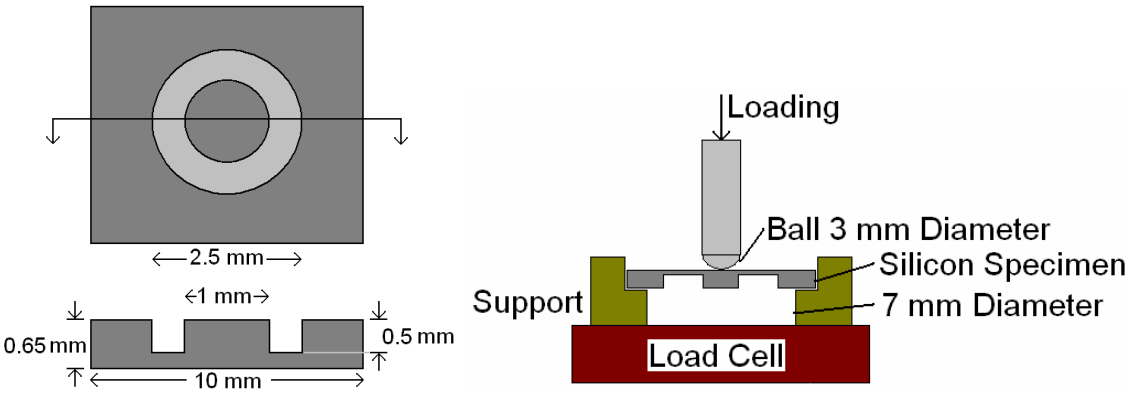

(a) Illustration of RHFS Geometry

(b) Illustration of RHFS test setup

Figure 3-1: Illustration of RHFS geometry and testing procedures (not to scale)

In this research, the RHFS fabrication steps, loading conditions, and failure location does not closely match that of the intended pressure vessel design. In both Chen's and Noonan's work the RHFS fabrication and their target specimen design had loading conditions where the failure was expected to be at the bottom of an etch produced by DRIE similar to the RHFS. In Chen's work, the maximum stress and location of expected failure was at the hub root of the rotating disk and/or the root of a DRIE etched turbine blade. In Noonan's work, the maximum stress and observed failure was at the inner circumference of the pressure vessel which was produced by DRIE. The pressure vessel cells in this research would ideally be fabricated through a combination of DRIE followed by an isotropic etch that would produce large fillets at the ends of the cells.

3.1.1 Strength Recovering Techniques

Previous Work in Strength Recovering

The RHFS is used in this research not necessarily to model the pressure vessel failure conditions but rather to evaluate the effectiveness of new strength recovering techniques in a way that can be done relatively easily and can be compared directly with previous work. Both Chen and Noonan explored isotropic wet and dry smoothing etches done in the last step of the RHFS fabrication process. Chen explored a wet etch which consisted of a combination of 5% HF, 55% HNO_3, and 40% deionized water and 20 seconds of a SF_6 plasma etch to smooth out surface flaws caused by the DRIE. Noonan explored two DRIE etch recipes that were slightly different from Chen's recipe, explored the effect of longer SF_6 plasma etching (up to 2 minutes), and incorporated stress concentration factors into her failure stress values. Table 3.1 lists the results of Chen's and Noonan's RHFS testings and smoothing.

Table 3.1: Previous RHFS testing results

Researcher	**DRIE Recipe**	**Smoothing Technique**	**Characteristic Strength [GPa]**	**Weibull Modulus**
Chen	MIT59	none	1.5	9.04
Chen	MIT59	wet etch	2.9	4.3-5.3
Chen	MIT59	SF_6 (20 sec)	4	3.3-8.8
Noonan	ADAM06	none	3.402	5.014
Noonan	ADAM06	SF_6 (20s-2min)	8.891	2.693
Noonan	MIT69	none	4.691	3.101
Noonan	MIT69	SF_6 (20s-2min)	8.584	2.642

Linear Elastic Fracture Mechanics and Surface Roughness

We hypothesize that silicon wafers are produced in such a ways as to significantly reduce internal flaws and that failure causing critical flaws in silicon structures are produced on the surface through the fabrication process. This is why it is believed that the key to improving silicon strength is reducing the surface flaw size with smoothing techniques. Linear Elastic Fracture Mechanics implies that for a material with

fracture toughness, K_{IC}, and crack size, a,

$$\sigma_f = \frac{K_{IC}}{Y\sqrt{\pi a}} \tag{3.1}$$

such that Y is a shape factor close to unity and σ_f is the fracture strength of the material. This means that the smoother the surface or the smaller the surface roughness, the stronger the material will be. Single crystal silicon has a fracture toughness between 0.8 and 1 MPa$\sqrt{m}$ depending on the orientation of the material.[13] Thus, to obtain a fracture strength of 1 GPa for silicon, cracks in the material can be no larger than $0.3\mu m$. For surface flaw considerations, this means roughness that is no larger than $0.3\mu m$.

Methods to Reduce Surface Roughness

The following methods for smoothing the etched silicon surfaces were considered in this research:

- Wet etch of hydrofluoric acid/nitric acid/DI water (HF/HNO_3)[8]
- Wet etch of potassium hydroxide (KOH)[8]
- Dry etch of SF_6[8, 31]
- Oxidize and remove oxide[37]
- Surface Migration/Hydrogen annealing[25]

According to Chen's work, the HF/HNO_3 wet etch showed a 93% improvement in Weibull reference strength from the baseline but with a reduction between 41% - 52% in Weibull modulus m. Chen also showed strength and modulus improvements with potassium hydroxide wet etching (KOH) on unetched silicon specimens in a biaxial stress state but such an etch on DRIE structures would cause etching along the diagonal crystal planes of the silicon due to the nature of the etch and thus would not be applicable to this work. Both Chen and Noon explored SF_6 plasma etches secondary to the DRIE etches that showed 167% - 525% improvements in

Weibull reference strength but reductions between 2.7% - 71% in Weibull modulus m (Weibull modulus variation was due to full data sets and subsets of data with outlier data omitted). These promising results lead us to include secondary SF_6 etches in our exploration. One of the more promising smoothing etches considered is surface migration which has shown effective ability to smooth silicon surfaces and fillet sharp corners however has yet to prove improvements in silicon strength and modulus. Surface migration was described in more detail in section 1.2.3. Finally, work has been done in a surface smoothing process involving wet thermal oxidation and oxide removal. This oxidation smoothing method has been used for surface roughness on the order of hundreds to thousands of femtometers. So the most promising and practical surface smoothing etches which are considered in testing variations in this research are dry SF_6 etches, silicon oxidation and oxide removal, and surface migration.

The photoresist mask used for the deep trench etching was reinforced with $500nm$ of oxide to reduce the thickness of the roughness band that is produced on the top portion of the trench sidewall from DRIE. This roughness band consists of vertical striations that tend to occur at the top of the etch sidewall and disappear several microns below the top of the etch. This action was taken to reduce sidewall roughness that might contribute to RHFS failure at reduced strengths. This roughness band at the top of the DRIE trench sidewall is thought to be caused by photoresist breakdown during the etch and the oxide reinforcement is thought to reduce the roughness band thickness or depth.[2] Noonan also used a $500nm$ oxide reinforcement while Chen did not.

3.2 Fabrication

RHFS for this research were fabricated in a similar way as those made by Chen and Noonan with a few changes.[8, 31] The processing steps are illustrated in figure B-1 and are listed in detail in appendix B along with the etch recipes. The device starts with a 6 inch double side polished <100> orientation wafer. The wafer is RCA cleaned so that it can be placed in a high temperature tube to have

500 nm of wet thermal oxide grown on it at 1000°C. Once coated with oxide, the front and back of the wafers are coated with a thick layer of AZ4620 photoresist with a thickness of about 8μm. (Both the front and back of the wafer are coated with photoresist to protect the backside from damage during the etching processes.) The front-side of the of the wafer is exposed with a Electronic Visions EV620 system with a mask that is illustrated in figure B-1 as M2 and figure 3-3(b). Mask 2 is intended to serve as alignment marks for the loading during the experiment on the back-side of the wafer and numbers to indicate the die position on the wafer frontside. After the photoresist has been exposed and developed, the exposed oxide underneath is plasma etched with an AME P5000 oxide dry etcher. After the oxide is etched through, the photoresist is stripped off with an oxide plasma and the same photo steps and oxide etch are done on the back-side with mask 2 aligning from front to back with the two alignment marks on the mask. The back-side of the wafer is SF_6 etched with an ICP deep trench etching system that was also used for DRIE for 15 seconds to 1 minute to make a shallow etch ($\sim 1\mu m$) of the alignment marks in the backside silicon. The photoresist is removed one more time. The front-side of the wafer is coated with a thick layer of photoresist and the wafer back-side is coated with an approximately 8μm photoresist

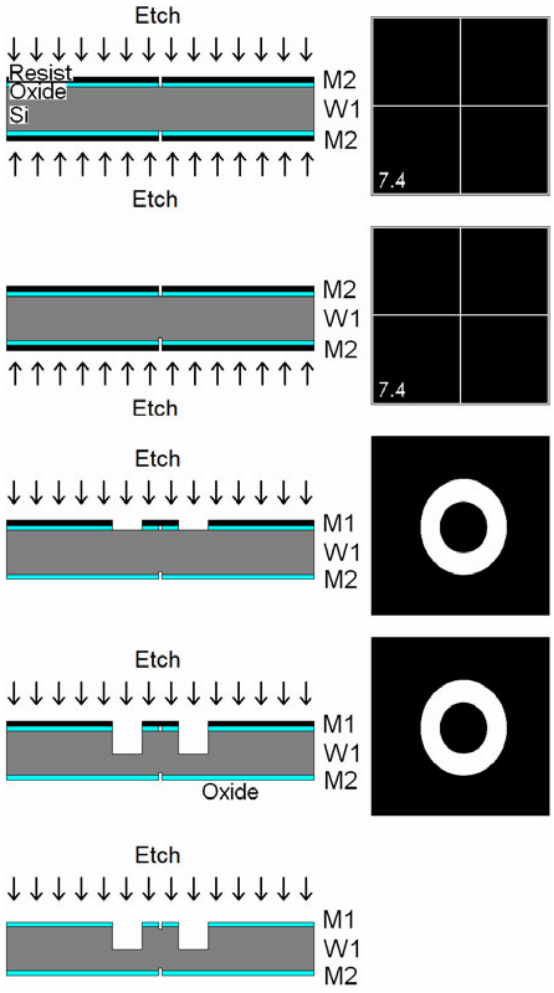

Figure 3-2: Illustration of die cross-section and mask through process

layer for protection. For the $650\mu m$ wafer, a double layer between $16\mu m$ to $20\mu m$ was necessary on the wafer front-side to prevent the oxide layer from being etched through during DRIE. For thinner wafers, from $500\mu m$ or less, a single layer of photoresist around $10\mu m$ was sufficient. The frontside of the wafer is exposed with mask 1 which is aligned with the two alignment marks on the right and left off-center side of the masks. Mask 1 is illustrated in figure B-1 as M1 and figure 3-3(b). The exposed oxide from mask 1 is etched and the wafer is then DRIE etched until a membrane thickness of $150\mu m$ remains. The DRIE recipe used is given in appendix B The photoresist is then removed and the front-side is SF_6 etched to make a shallow mark from the mask 2 marks etched in the the remaining oxide. The oxide is stripped from the wafer with a buffered oxide etch solution (BOE) or a hydrofluoric acid (HF) solution and the wafers are smoothed with SF_6 etching, oxide growth and removal, and/or hydrogen annealing/surface migration. The etch depth of each die is measured using a Wyko NT9800 non-contact profiler and the wafers are cut with a Disco Abrasive System die saw.

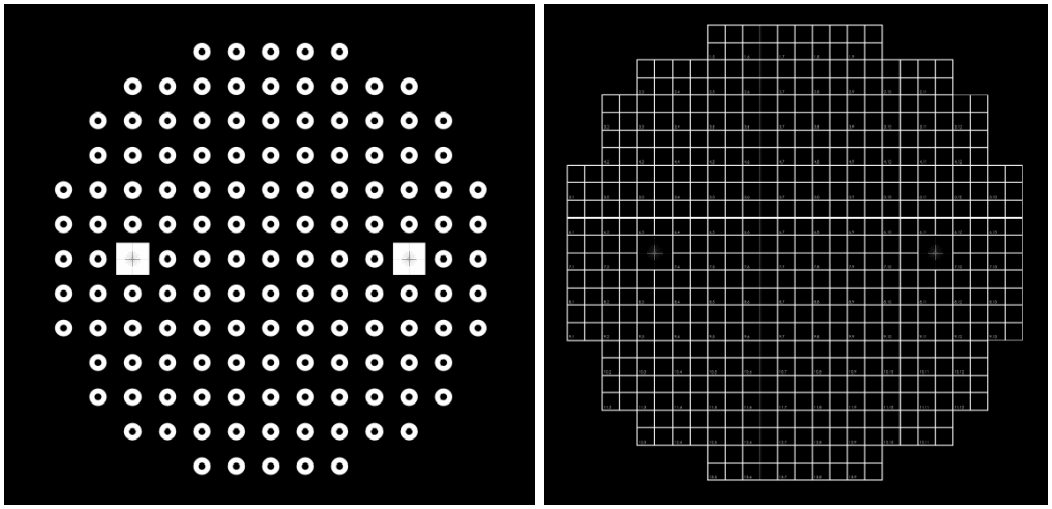

(a) RHFS Mask 1 (b) RHFS Mask 2

Figure 3-3: Illustration of RHFS masks

There was a number of differences between this RHFS fabrication and the fabrication done by Chen and Noonan. Both Chen and Noonan used 4 inch wafers instead of 6 inch wafers. Both Chen and Noonan used mask patterns that were half as dense

with RHFS dies than the masks used in this research illustrated in figure 3-3. Noonan used a wet buffered oxide etch (BOE) to etch the mask reinforcing oxide while Chen did not use an oxide mask reinforcement at all. Noonan mounted her 4 inch wafer onto a handler wafer for the DRIE while Chen used a machine that could accept unmounted 4 inch wafers for DRIE. The thickness of the wafers used varied for each researcher. Chen used wafers that were $500\mu m$ thick with trenches that were etched to a depth of $350\mu m$. Noonan used wafers that were $400\mu m$ thick with trenches that were etched to a depth of $250\mu m$. This research started with wafers that were $650\mu m$ and etched to a depth of $500\mu m$. As the research progressed, it was necessary for 4 inch wafers to be used to include the hydrogen annealing smoothing in the process. The 4 inch wafers used were $450\mu m$ and $600\mu m$ thick due to availability. Wafers that had a 6 inch diameter that were $500\mu m$ thick were used to compare etch depth effects on strength. Finally, the backside alignment marks on the samples were eventually omitted from the fabrication process. These alignment marks were etched on the backside by both Chen and Noonan to center the load in the experiment. As will be described in section 3.3, backside alignment marks were not necessary for centering. The backside alignment marks were only etched on the first few RHFS sets in this research.

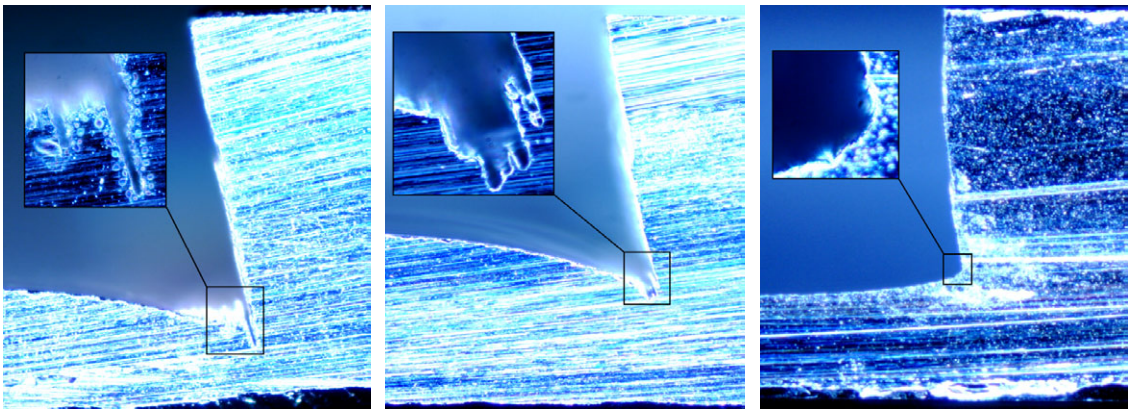

(a) Worst fillet result (b) Better fillet result (c) Best fillet result

Figure 3-4: Cross-sections of RHFS showing inner hub wall and root

The deep reactive ion etching recipe used in this research cannot be compared

directly to previous research because it was done in a different machine than the one used by previous researchers. Finding the optimal DRIE recipe and etching conditions required quite a bit of trial and error. It was decided early on that Chen's MIT59 etch recipe would be the most promising to use because it gave the largest values of Weibull modulus with reasonably high values of characteristic strength. Although there were a few parameters in the recipe that could be changed including etch time, passivation time, platen power, coil power, and gas flow, only pressure was varied until an optimal fillet radius was observed. Figure 3-4 shows a sampling of cross-sections obtained from varying pressure. These figures were obtained with an optical microscope of a RHFS that had been sawed in half with a die saw. During the trial and error development of the deep reactive ion etch, it was determined that rotating the wafer by 90 degrees at evenly distributed times during the etching process helped provide radial symmetry of the etch and reduced risk of overheating. The radial symmetry of the etch can be verified by the radially symmetric failure stress distribution over the wafer illustrated in figure 3-9

3.2.1 Surface Migration and Related Fabrication

Finding a system in which surface migration could be done was difficult. Surface migration requires a system capable of maintaining a high temperatures of at least 1000°C and pressures of at most 10 Torr for minutes to hours. For this reason, epitaxial chambers are required to achieve surface migration. Epitaxial chambers are normally used to deposit a monocrystalline films on a monocrystalline substrates and have strict cleanliness restrictions. DRIE, the main etching step used in this research, is typically thought of as a "dirty" fabrication process since it deposits polymer on the silicon surface and is used for higher contamination micromechanical processes. Due to the "dirty" reputation of DRIE, it is difficult to convince those who own epitaxy chambers for thin films to allow DRIE wafers into their system. Thus, without a dedicated system, research with surface migration for strength recovery of DRIE silicon will be highly limited by the discretion of others. Since this research was done independently and not part of a larger, well-funded project like the micro-engine

project, it had to rely on the stipulations of systems owned by other projects.

Surface migration in this research was conducted by two methods. The first method was by hydrogen annealing on 4" wafers and required changes be made to the process so that 4 inch wafers of RHFS resulted. The second method was with annealing in an ultra-high vacuum (UHV) which could be done on 6" whose fabrication was described above.

Hydrogen annealing was done at Stanford University in Professor Roger T. Howe's Centura epitaxial reactor. The wafers were annealed at 1100°C and 10 Torr H_2 pressure. The 4 inch wafers were fabricated with almost the same steps as the 6 inch wafers with just a few differences. All the oxide etching was done with a BOE etch instead of a dry plasma etch. The wafers were mounted onto a 6 inch quartz handler wafer to be DRIE etched. Wafers were mounted with a target photoresist pattern.

Ultra-high vacuum (UHV) annealing was done here at MIT in Professor Eugene A. Fitzgerald's customized Thomas Swan/AIXTRON low pressure MOCVD system. The results for UHV annealing was with a $3.9E{-}9$ Torr environment at 900°C for just less than 66 hours.

3.3 Experimental Work

As was illustrated in figure 3-1(b), the testing of the RHFS involved a loading mechanism above a RHFS holder resting on a load cell. The RHFS held the centimeter square die centered over a 7 mm hole through which the die could deflect. The test setup is shown in figure 3-5. An Oriel Instruments DC Encoder Mike^{TM}actuator was used to apply the linearly translating load in a controlled way. The actuator could apply a maximum force of 22 lbf (just less than 100N). The loader tip was applied to the RHFS at a speed of $2\mu m$/sec. The loader tip was controlled with its own linear translator controller pictured in figure 3-5. The basis of test setup is Chen's microscope from his research. A special attachment was machined out of aluminum to attach the linearly translating loader to Chen's microscope experimental setup. Aluminum sample and load cell holders were also fabricated to attach to the system.

The load cell used could measure loads up to 50 lbs. A known weight of 10 pounds was used to calibrate the load cell before every experiment. The load cell output was amplified and measured through a National Instruments data acquisition card and LabVIEW^{TM}software.

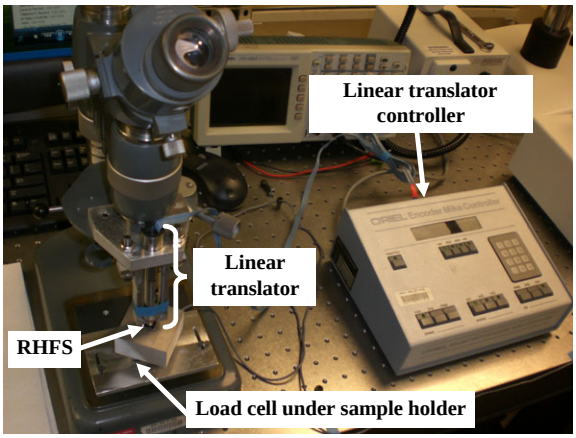

Figure 3-5: RHFS experimental setup

Centering of the loader with respect to the RHFS was done by lowering the loader tip through the 7 mm deflection hole, adjusting the microscope position, and raising the loader tip to place the RHFS into its holder. The first few RHFS had shallow alignment marks etched into the wafer backside to align the loader with the center of the die. The intention was to use the microscope to center the loader. After the experimental system was finished being developed, it was determined that the loader could be centered by simply centering the retracting tip of the loader in the 7 mm deflection hole as is illustrated in figure 3-6.

According to error analysis in appendix C, about 50 samples are needed to have less than 2% error in Weibull parameter estimation. Other sources have stated that 20 to 30 samples are necessary to give accurate estimations as a rule of thumb but do not provide substantiation for this claim.[28, 9] In this research we strive to have 50 - 100 samples per data set.

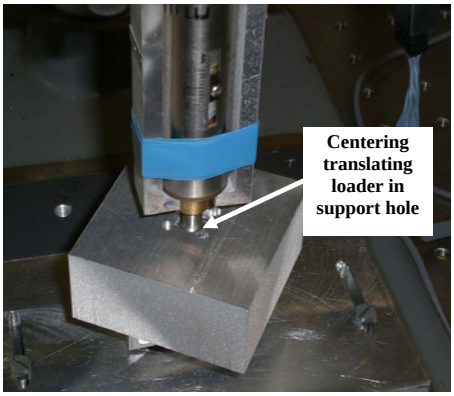

Figure 3-6: Procedure to align translating loader

3.4 FEM Modelling

A finite element model (FEM) was developed of the RHFS and its loading conditions to determine stress distribution in the baseline device geometry and geometry variations. The finite element model allows us to have a reasonably accurate model of the device behavior which can in turn be used to accurately evaluate the experimental results. The baseline RHFS FEM model was made with a toroidal trench with inner

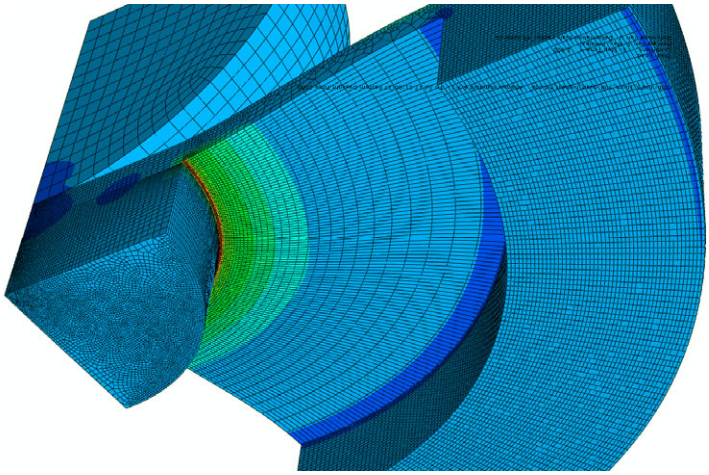

Figure 3-7: Illustration of principal stress distribution in RHFS FEM model from a perspective below RHFS.

and outer diameter of 1mm and 2.5mm respectively, with a wafer thickness of $650\mu m$, and etch depth of $500\mu m$, and a fillet radius of $11\mu m$. Discussion on how fillet radius was measured can be found in appendix C The model had a circular diameter of

7mm. The RHFS model includes a steel 3mm diameter hemisphere which applies a load that is varied to represent the range of loads that the RHFS might experience in the experimental testing. Only a quarter of the RHFS and loading hemisphere is modeled with a symmetry boundary condition on the x-axis and y-axis boundaries. The circumferential edge at the diameter of 7mm is modeled as a pinned boundary condition on the deep etch face. A mesh sensitivity study was done for the baseline RHFS FEM model for loads of 10.74MPa, 35.81MPa, and 57.3MPa. The results of this study are shown in appendix F. Fluctuations in maximum stress with respect to seed sizes smaller than $150\mu m$ showed minimal fluctuations. Seed size in the model represented the distance between seed points which defined distance between grid points. The smaller the seed size the finer the mesh. A seed size of $50\mu m$ was used for geometry variation studies. For the fillet radius area, partitions were manually added to the model to refine the mesh around the small geometry variation.

3.4.1 FEM Calculation of Uncertainty

The model was used to determine uncertainty in the experimental data. The model was used to make a table of varying load and etch depth with a constant fillet radius of $11\mu m$ and a table of varied load and fillet radius with a constant etch depth of $500\mu m$. The tables each varied load between 0 and 29 MPa. The table with varied fillet radius varied the fillet radius between $1\mu m$ and $12\mu m$ in increments of $1\mu m$. The table with varied etch depth varied etch depth between $470\mu m$ and $570\mu m$ in increments of $10\mu m$. The variation showed little dependence of the maximum principal stress measurement on small fillet radius variation and larger dependence of the maximum principal stress measurement on etch depth variation which was taken into account in the experimental data reduction. Wafer thickness variation did not seem to play a major role in maximum stress variation as much as the final membrane thickness did. Error analysis due to geometry variation is described in more detail in appendix C. The results of the error analysis was an uncertainty of 2% in the Weibull parameters derived from the experimental data.

3.5 Results

Tests were performed for a number of conditions. Table 3.2 lists the differences between the different data sets in terms of starting wafer and smoothing techniques and the respective Weibull parameters found with the total data sets. The Weibull plots for this data can be found in appendix D. Figure 3-8 shows a comparison of this data with that of Chen and Noonan. For each data set, variations in strength from binning portions of the data set based on radial position is illustrated with a line spanning maximum and minimum Weibull parameter values in figure 3-8. Lines of constant failure probability are also plotted so improvements in strength can easily be identified by shifts to the right and up of a line.

Table 3.2: RHFS testing results

Wafer ⌀ [in]	**# of data points**	**Wafer Thickness [μm]**	**Smoothing Technique**	**Characteristic Strength [GPa]**	**Weibull Modulus [–]**
6	112	650	1min SF_6	2.33	3.78
6	108	650	1min SF_6+Ox	5.51	2.40
6	68	650	1min SF_6+Ox+UHV	2.9338	5.2955
4	42	450	1min SF_6	1.32	2.12
4	56	450	1min SF_6+0.5hr H_2	0.853	7.05
4	52	600	1min SF_6+2.5hr H_2	1.11	8.04
6	71	500	6min SF_6	4.48	2.90
6	67	500	6min SF_6+Ox	5.23	1.70

Initially, a one minute long SF_6 etch smoothing was explored with and without oxidation and oxide removal smoothing on 6" 650μm wafers. The results appear to lie on the same line of constant failure probability as Chen and Noonan's work as can be seen in figure 3-8. Ways of binning the data was also explored to see if improvements could be made with the Weibull parameters. It was found by only using data between radial positions r such that 35mm < r < 55mm (the unshaded portion in figure 3-9) had much higher values of Weibull modulus. For the case of SF_6 smoothing without oxidation, values of $m = 5.54$ and $\sigma_{RHFS} = 2.37$ (with 55

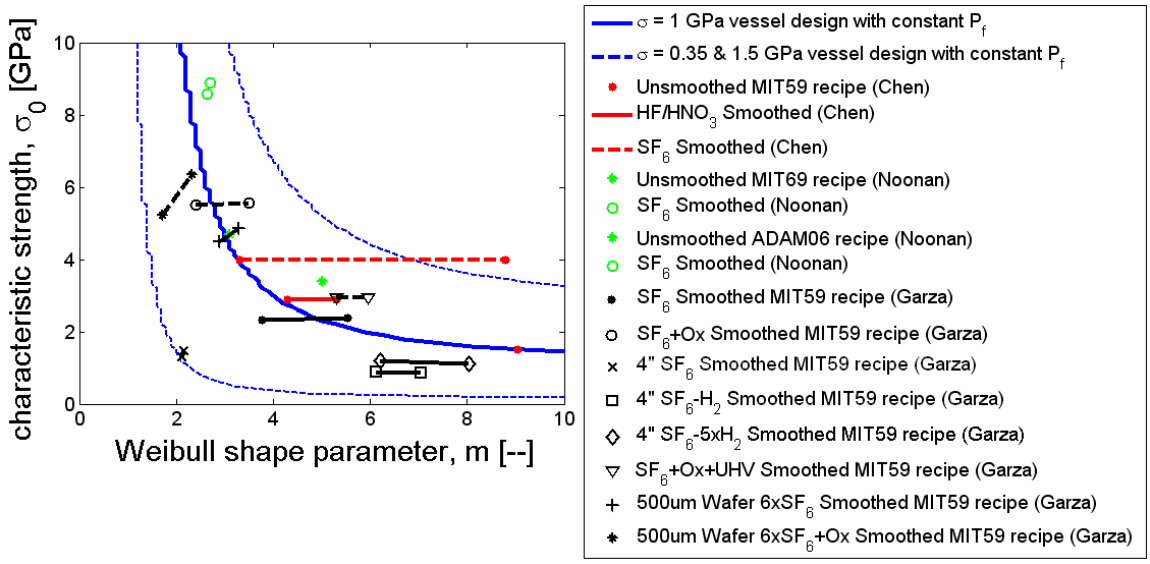

Figure 3-8: Comparison of RHFS results to previous RHFS results.

data points) were obtained with binning as opposed to $m = 3.78$ and $\sigma_{RHFS} = 2.33$ without binning. For the case of SF_6 smoothing with oxidation, values of $m = 3.49$ and $\sigma_{RHFS} = 5.55$ (with 54 data points) were obtained with binning as opposed to $m = 2.40$ and $\sigma_{RHFS} = 5.51$ without binning. Variations in strength with binning are illustrated with a line spanning maximum and minimum Weibull parameter values in figure 3-8. This variation in Weibull modulus depending on the radial position of the dies on the wafer supports a hypothesis that flaw size is affected by radial position of the sample during etching. Another way to say this would be that the **DRIE process produces flaws non-uniformly but predictably across the wafer**.

As described in section 3.2.1, hydrogen annealing was done on 4 inch wafers which were mounted on a handler wafer during DRIE in addition to one minute long SF_6 smoothing. The results of the hydrogen annealing showed significant improvements for longer anneal times around 2.5 hours from the baseline of a 4 inch wafer with no hydrogen annealing. (Note: The baseline 4 inch wafer tested did not have all the etch depths measured so its Weibull parameters will have more uncertainty than other Weibull parameters found experimentally.) However, all the 4 inch wafer results had far lower failure probability than their 6 inch counterparts. This result implies that

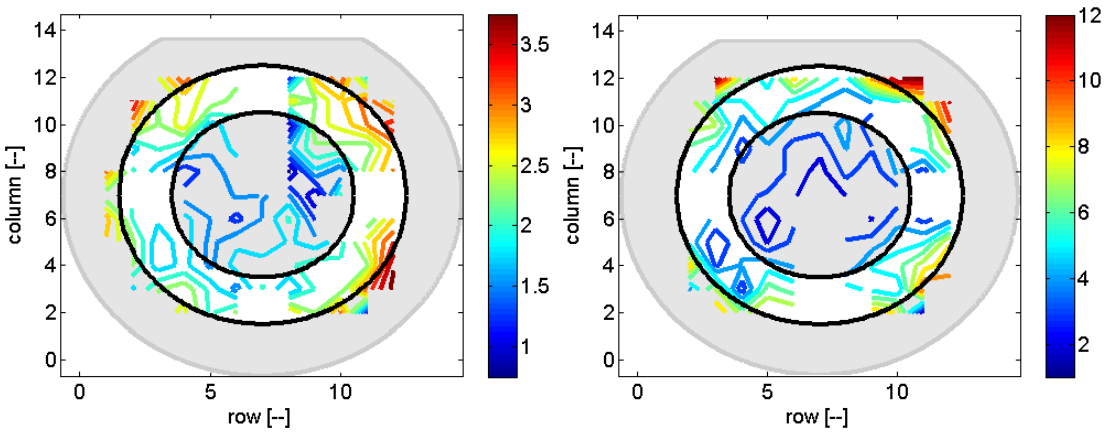

(a) SF_6 RHFS Failure Stress in GPa (b) SF_6+Oxide RHFS Failure Stress in GPa

Figure 3-9: Failure stress distribution over wafer with omitted data represented by grey area

the changes to the process necessary to accommodate 4 inch wafers may have reduced subsequent strength of the RHFSs. It is hypothesized that **the poor thermal contact between the quartz handler wafer and the 4 inch wafers of RHFSs may have led to an increase in flaws and/or flaw sizes**. It was found by only using data between radial positions r such that 35mm < r < 55mm on the 4" wafer data actually led to lower strengths for the hydrogen annealed 4" wafers. For the case of 0.5 hours of hydrogen annealing, values of $m = 6.13$ and $\sigma_{RHFS} = 0.89$ (with 26 data points) were obtained with binning as opposed to $m = 7.05$ and $\sigma_{RHFS} = 0.853$ without binning. For the case of 2.5 hours of hydrogen annealing, values of $m = 6.20$ and $\sigma_{RHFS} = 1.19$ (with 22 data points) were obtained with binning as opposed to $m = 8.0375$ and $\sigma_{RHFS} = 1.11$ without binning.

Ultra-high vacuum (UHV) annealing was done on a 6" $650\mu m$ wafer in addition to a one minute long SF_6 etch and oxidation and oxide removal smoothing. It was necessary to test surface migration on a 6" wafer to verify the hypotheses that surface migration would in fact improve usable strength of DRIE silicon and that mounting 4" wafers on quartz handler wafers during DRIE reduced the overall strength of the silicon (as opposed to the hydrogen annealing). The results of the UHV annealing show the highest strength data of all the testing done in this research. Slight im-

provements in strength were found by only using data between radial positions r such that 35mm $<$ r $<$ 55mm. This data confirms that **surface migration will improve usable strength of DRIE single crystal silicon**.

Finally, six minute long SF_6 etch smoothing was explored with and without oxidation and oxide removal smoothing on 6" $500\mu m$ wafers. Wafers with a thickness of $500\mu m$ were used to explore a theory that $350\mu m$ was an optimal etch depth for RHFS discussed more in section 3.5.2. Six minutes of SF_6 etch smoothing were used after examining the effecting of increased SF_6 etch times on the sidewall roughness under the SEM. As can be seen in figure 3-8, the addition of oxide smoothing to the six minute SF_6 smoothing came with a significant penalty in failure probability even though characteristic strength was improved slightly. It is hypothesized that **oxide growth and removal for strength recovery purposes results in higher characteristic strength because it reduces large flaw sizes but may reduce Weibull Modulus and overall strength by adding greater variation to the flaw distribution**. This could have something to do with the fact that oxide smoothing consumes and removes a thin layer of silicon from the surface of the silicon but may do so by adding variation with non-uniform silicon consumption in oxide growth. Because we see improvement in characteristic strength from oxidation we know there has to be a reduction in large flaw sizes. Reduction in Weibull modulus and overall strength could have something to do with non-uniform silicon consumption during oxidation. It has been shown that small roughness features will oxidize faster than larger features which would change flaw variation of a silicon surface with non-uniform roughness.[26] Research has shown that oxidation will consume less material from sharper edges which results in sharpening of spike geometry and sharp pits that are made more blunt and wide.[27] Although it is not clear how this kind of oxidation sharpening will effect the critical stress of a surface flaw, it is clear that it will change the characteristics of the silicon surface roughness which explains the reductions of Weibull modulus.

3.5.1 SEM Analysis of Smoothing

A scanning electron microscope was used to examine the effects of the smoothing done to improve silicon strength. Figure 3-10 shows SEM images of the sidewalls for various kinds of smoothing. The bottom of the image is the sidewall bottom. The bottom of the trench can barely be seen at this angle because it is smooth and, at this angle, appears dark. It can be seen that hydrogen annealing produces a significant improvement in sidewall smoothness at the hub root.

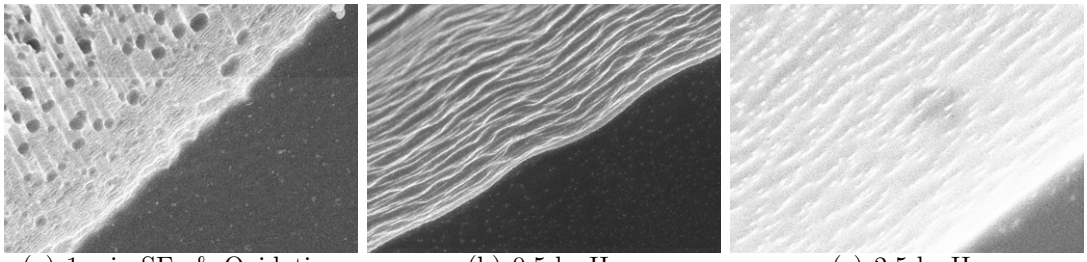

(a) 1 min SF_6 & Oxidation (b) 0.5 hr H_2 (c) 2.5 hr H_2

Figure 3-10: SEM images of various amounts of smoothing (10k magnification)

3.5.2 Exploring Sidewall Roughness

We are interested in understanding the roughness patterns and vertical striations that appear on the trench sidewalls since roughness size can be related to surface flaw size. This phenomenon is shown in figure 3-12. Specifically, why there are patches of striations and patches free of striations. We would like to know if these roughness patterns vary across the wafer and if they vary depending on etch depth.

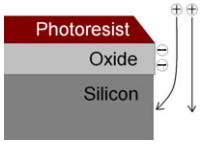

Figure 3-11: Distorted ion flux

What is the cause of these sidewall striations? Vertical striations on DRIE silicon sidewalls often occur on deeper etches. I spoke with Hanqing Lee, a researcher with many years experience with DRIE who worked heavily on the MIT micro-engine project, who says that every wafer with DRIE more than a hundred microns deep will have vertical striations on

the walls. It has been theorized in the literature that pitting and vertical striations on the sidewalls are caused by charging on the dielectric resist and/or oxide that distort the ions during DRIE.[33] Figure 3-11 illustrates how charging on the dielectric resist and/or oxide mask can cause charged ions to be directed to the sidewalls to cause pitting and also develop striations.

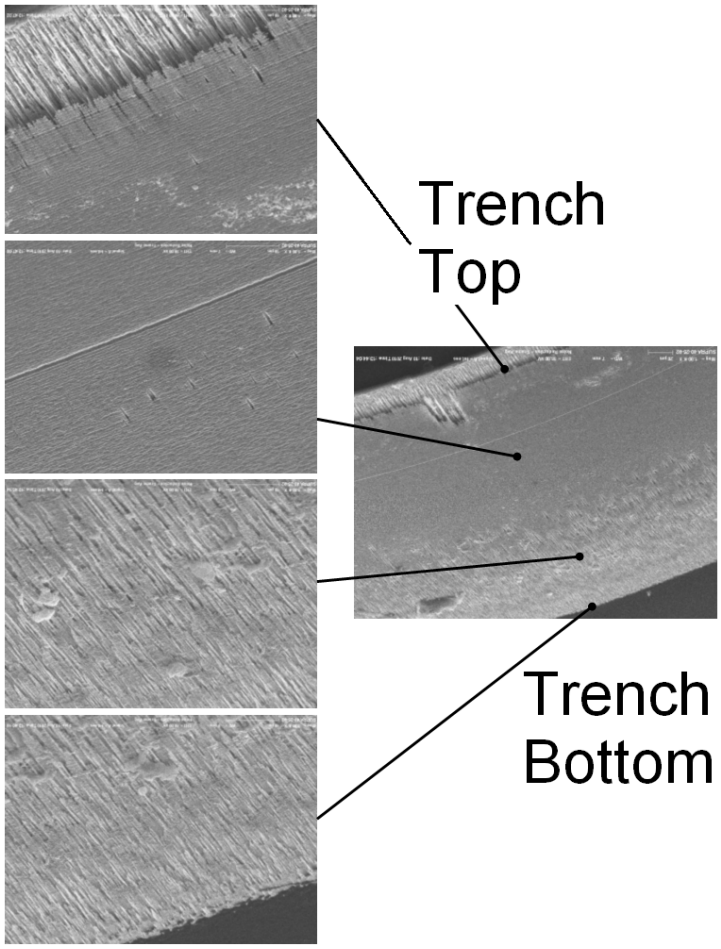

Figure 3-12: RHFS trench sidewall

Etch Depth and Sidewall Roughness

We would like to know if the thickness and pattern of the vertical striations on the sidewall is consistent for different etch depths. In figure 3-13(a) it appears as if vertical striations near the top of the etch do not reach deeper than $250\mu m$. Striations near the trench bottom do not seem to appear abundantly until after $350\mu m$. Thus,

there appears to be a "smooth" belt between $250\mu m$ - $350\mu m$. Closer inspection into this "smooth" region reveals roughness that looks like scallops from the DRIE etch/passivation process as well as smaller roughness less than the order of the scallops (all less than a micron). These "smooth" features are shown magnified with an SEM in figure 3-13(b). This kind of pre-smoothing surface is the best we can hope for.

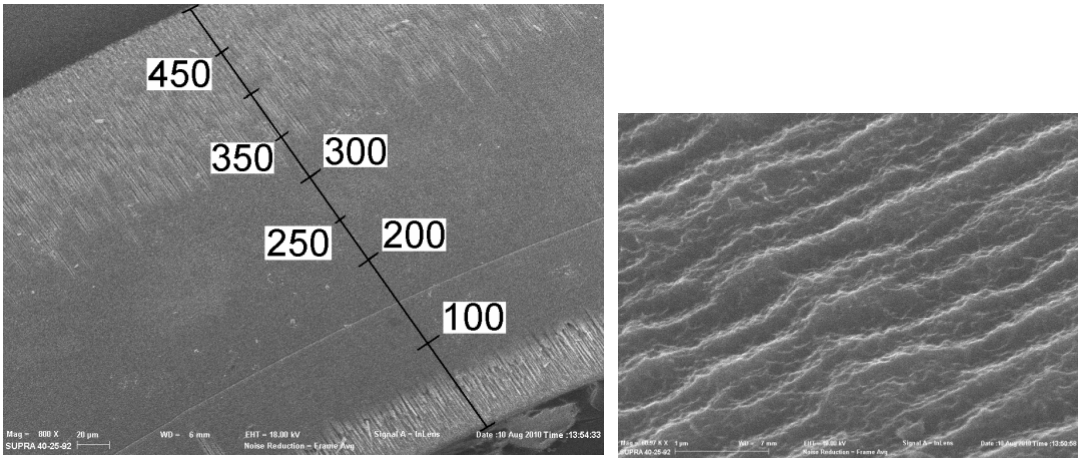

(a) $500\mu m$ etch with 20 second SF_6 smoothing

(b) Magnification of smooth regions between roughness bands

Figure 3-13: Inspection of sidewall at varying etch depths

We noted in the fabrication section 3.2 that Chen etched to a depth of $350\mu m$ and Noonan etched to a depth of $250\mu m$. We noted that $250\mu m$ is the position just below where the striations seem to end and $350\mu m$ is just before the second roughness band begins according to figure 3-13(a). It makes sense then that Chen's work had higher Weibull modulus' m values than Noonan, because the etch depth had a smaller spread of surface flaw sizes. For this reason we tested $500\mu m$ thick wafers etched to a depth of $350\mu m$. As can be seen in figure 3-8 however, this did not result in increased values of Weibull modulus. Therefore, we conclude that **etch depth does not play a large factor in overall silicon strength**.

Looking Underneath Overhanging Walls

Before sidewall roughness can be properly analyzed, we must address overhanging features on the DRIE sidewall and sub-surface roughness. The top portion of both

figure 3-13(a) and particularly figure 3-12 implies striations that are etched below an overhanging surface. One can see etching underneath the surface of the outside wall. For this reason, we analyze the DRIE sidewall surface with various amounts of SF_6 etching to explore below the overhanging walls to look at the solid surface underneath. This can be seen in figure 3-14

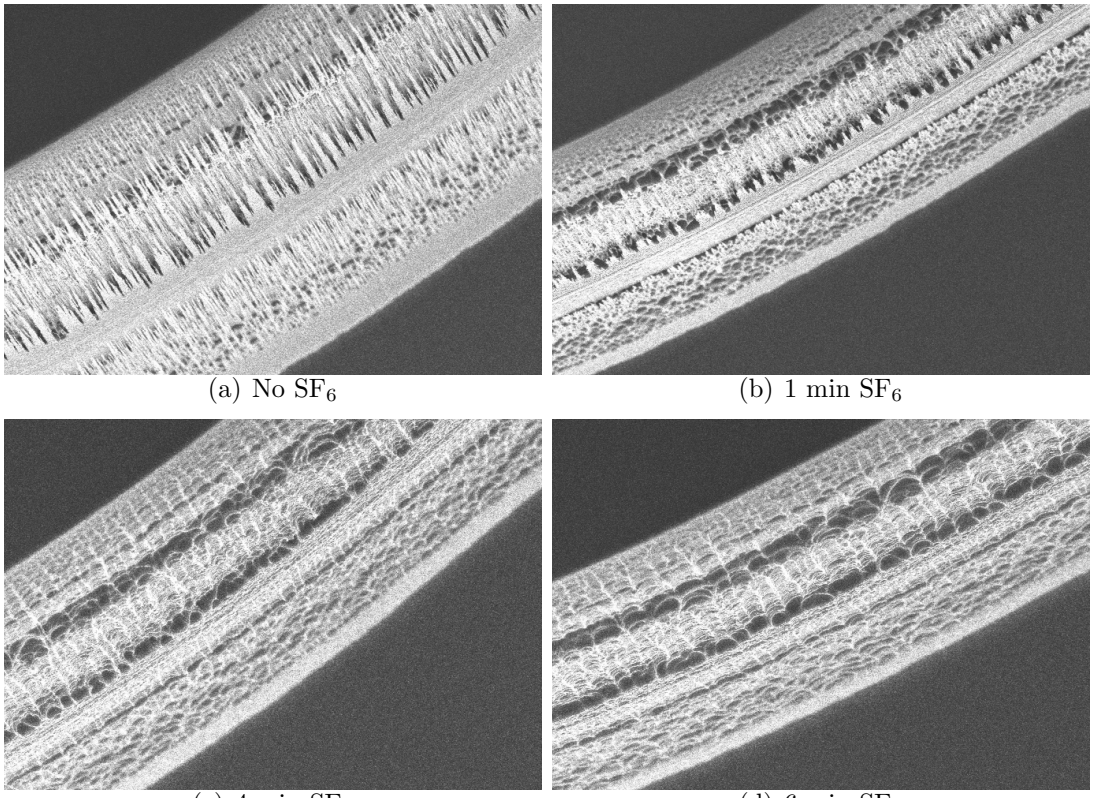

(a) No SF_6 (b) 1 min SF_6

(c) 4 min SF_6 (d) 6 min SF_6

Figure 3-14: Off center die (10.10) with various amounts of SF_6 (1k magnification)

Both Chen and Noonan performed SF_6 smoothing etches that lasted between 20 seconds to 2 minutes. Although we cannot be sure that the etch rates for the SF_6 smoothing etches done by Chen and Noonan were the same as those in this research, it is proposed that the actual sidewall surface roughness of the DRIE sidewall was hidden by a similar "curtain" of silicon overhanging wall that is apparent is figure 3-14. After studying sidewall images from Noonan's work, it appears as if Noonan may have assumed smoother solid surfaces where there was not because she did not do a sufficient amount of SF_6 smoothing to review sidewall roughness below overhanging

walls. Figure 3-15 show the hub root of a RHFS at a 5k magnification with 0 and 6 minutes of SF_6 smoothing. Significant changes in the surface morphology are apparent. Additionally, figure 3-15(a) looks much like the morphology of Noonan's SEM images of DRIE trench corners. In the case of figure 3-15(a), there are not blatant overhanging walls that make hidden solid walls beneath apparent. Thus, **smoothing etches are essential to properly analyze DRIE sidewall morphology in cases with overhanging silicon walls. Furthermore, deceptive sidewall roughness hidden by overhanging silicon walls from DRIE are not always blatantly apparent**. As discussed in section 3.1.1, size of surface roughness can be used to determine silicon strength and thus it is necessary to accurately determine DRIE silicon sidewall morphology.

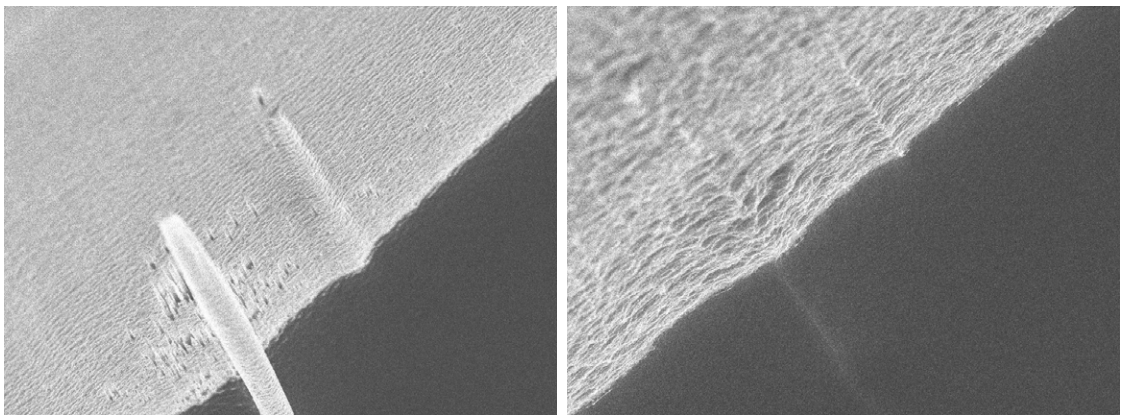

(a) No SF_6 (b) 6 min SF_6

Figure 3-15: Center die (7.7) root morphology with 0 minutes and 6 minutes of SF_6 (5k magnification)

Strength and Sidewall Roughness Variation Across Wafer

Once overhanging sidewall features are removed, we can begin to analyze wafer sidewall geometry across the wafer. It is quite difficult to find the largest or deepest flaw in the RHFS sidewall particularly at the root hub where the maximum stress is expected. The best that can be done is to identify geometric trends and variations in general trends. We believe it is a reasonable assumption to assume that large varia-

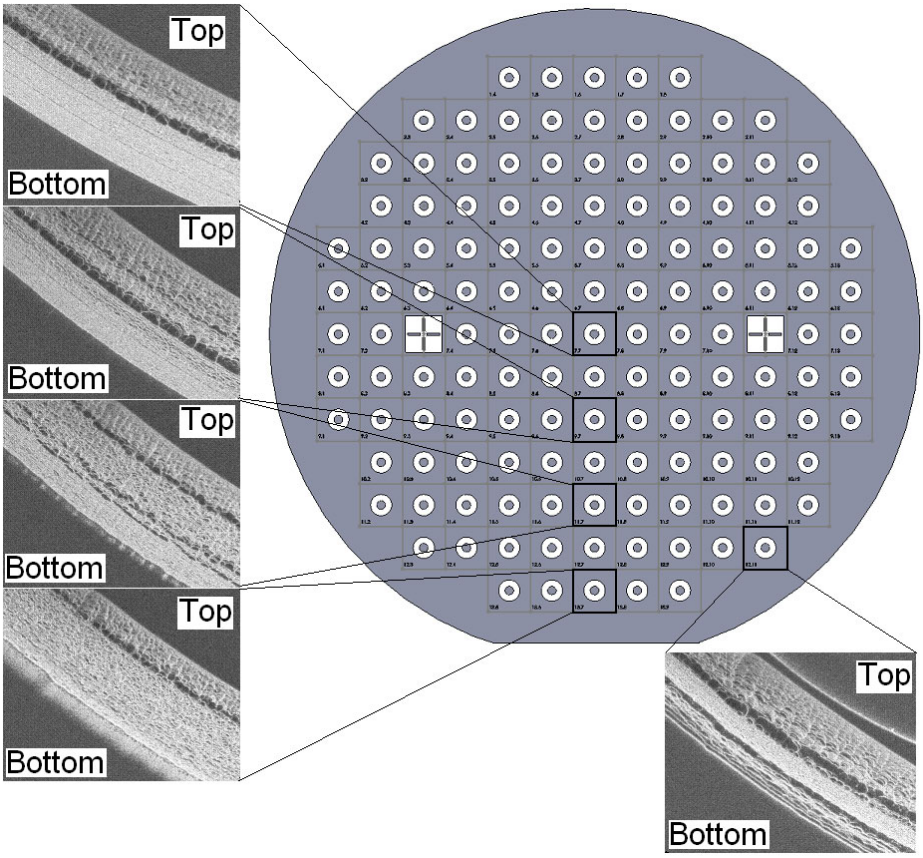

Figure 3-16: SEM images of DRIE sidewall at different wafer locations

tions of sidewall morphology over the length of the etch depth is a reasonable indicator of morphology variation at the hub root. Figure 3-16 depicts 1k magnification SEM images of RHFS sidewalls and the position on the wafer from which the RHFS came from. If you recall from section 3.2 the wafer DRIE etch has radial symmetry because the wafer was rotated 90 degrees evenly through the DRIE etch. One of the outermost specimens (12.11) shown in the lower right hand corner of figure 3-16 has deep notches etched into the sidewall close to the hub root. This geometry explains why Weibull modulus is increased when data from radial positions greater than 55mm are included in the Weibull parameter calculations. This SEM investigation confirms that **DRIE silicon strength with vary radially across the wafer**. Furthermore, we find that **removing the effects on strength of micron-scale geometry variation across the wafer (which was accounted for by the uncertainty analysis in**

appendix C) elucidates submicron scale geometry variation on the DRIE sidewalls which could be correlated to strength variation across the wafer.

Findings of radial strength variation from data binning and SEMs of macro-scale DRIE sidewall morphology brings to light a major difference between micro-scale and macro-scale device design. For micro-scale, die-level design, devices can be separated out preferentially from a single wafer so that higher strengths are obtained. For a macro-scale, wafer size device, we must design around the weakest link or what would have been the weakest die of a wafer full of micro-scale devices. Furthermore, it is important to note that strength variation across the wafer was found after accounting for micron scale geometry variations across the wafer. Thus, **for wafer-scale structural devices, strength uniformity across a wafer is an additional concern to micron scale geometry uniformity across the wafer**.

3.6 Summary

This chapter described experimental work to explore the usable strength of wafer-scale etched single crystal silicon using a radiused hubbed flexure specimen (RHFS). Previous work with RHFS was included in silicon usable strength analysis.

The strength recovery ability of SF_6 plasma etches, silicon oxidation and oxide removal, and surface migration were explored. SF_6 plasma etches also resulted in small amounts of strength recovery in the form of increased characteristic strength with reduced Weibull modulus. Oxidation and oxide removal resulted in both minor improvements and loss in strength with improvements in characteristic strength making oxidation an unreliable method for DRIE silicon strength recovery. Surface migration in the form of hydrogen annealing on 4" wafers resulted in visible smoothing of DRIE sidewalls but gave overall reduced strength due to wafer mounting added to the process to adapt the fabrication process to 4". Surface migration in the form of UHV annealing on 6" wafers gave the highest level of strength recovery but resulted in little visible smoothing to the DRIE sidewall. Overall surface migration has shown promise for strength recovery that could not be fully explored explored due to

limitations of resources and funding in this project.

SEM analysis of DRIE silicon sidewalls with long SF_6 plasma etches revealed differences in observed sidewall roughnesses from DRIE resulting from removal of overhanging silicon "curtain" features. Such differences in sidewall roughness affects correlation of silicon strength to surface flaw size.

Strength variation across a wafer from DRIE was found to be a concern for wafer-scale device design independent of strength variation due to design geometry variation across wafer. By isolating radial subsets of RHFS data that was normalized for geometry variation greater than a micron from a single wafer, DRIE silicon strength was found to vary dramatically across a wafer. Submicron sidewall variation was found to be a likely candidate for strength variation across a DRIE silicon wafer. This implies that the usable strength of DRIE silicon is limited by two across wafer variations, geometry variation (wall thickness, etch depth) and material strength variation from sub-micron geometry.

Chapter 4

Probabilistic Design of Silicon Pressure Vessel

In this section, we examine the impact of the brittle nature of silicon on pressure vessel design. We review statistical methods for characterizing brittle materials and then use these concepts to deduce the material properties needed for a reliable realization of the geometries discussed in chapter 2. The probabilistic design process for the pressure vessel will include an explanation of how material strength testing results will be incorporated into the final design.

4.1 Weibull Statistics

Material strength for brittle materials, such as single crystal silicon, is non-deterministic. This means that, as opposed to ductile materials such as titanium, a silicon structure will not reliably fail at the point of maximum stress or even at the same value of stress for each incidence of failure. Instead, the value and location of the failure stress of a brittle structure will be dependent on populations of flaws in structure. Flaws are any kind of imperfection in the material like cracks or incipient cracks. The kind of flaws in the materials, the size of the flaws, the orientation of the flaws with respect to the internal stresses in the structure, and the location of the flaws is unique to each device and will determine how each individual device will fail. Since flaw populations

in the structure determine its statistical strength, the volume and/or surface area of a given brittle structure will also play a role in the amount of flaws in the structure and thus the strength.

There are various ways to analytically model the probabilistic strength distribution of a given brittle material. The most common approach used for brittle material like ceramics and particularly single crystal silicon and the one used in this research is the Weibull weakest-link theory (WLT).[41] The Weibull WLT theory assumes a brittle structure fails when the equivalent stress at a flaw reaches a critical value depending on a fracture mechanics criterion and flaw details. The Weibull WLT only considers failure in tension because brittle materials have much stronger compressive strengths than tensile strengths. Classical three-parameter Weibull WLT for a material in uniaxial tension is given by

$$P_f = 1 - \exp\left(-\frac{V}{V_0}\left(\frac{\sigma - \lambda}{\sigma_0}\right)^m\right)$$

where V is the volume of the material, V_0 is the reference volume, σ_0 is the Weibull scale parameter or characteristic strength, m is the Weibull shape parameter or the Weibull modulus, and λ is a location parameter or threshold parameter. The characteristic strength, σ_0, is an indicator of average strength defined as the strength at which the probability of failure is approximately $1/3$ ($1/e = 0.37$). The Weibull modulus, m, is an indicator of the spread of strength values or distribution of flaw size. A higher value of Weibull modulus means a smaller spread of strength and flaw size and a higher reliability of the material under a given stress. The threshold parameter, λ, represents a cut-off of the strength and is often taken to be zero for ceramics which gives the two-parameter Weibull distribution described in earlier chapters:[29]

$$P_f = 1 - \exp\left(-\frac{V}{V_0}\left(\frac{\sigma}{\sigma_0}\right)^m\right)$$

This two-parameter Weibull function can also be taken for materials where flaws

only occur on the surface. In this case, surface area replaces volume to give:

$$P_f = 1 - \exp\left(-\frac{A}{A_0}\left(\frac{\sigma}{\sigma_0}\right)^m\right)$$

The equations given above are for uniaxially stressed materials. For samples exposed to multiaxial stress states this equation must be modified. One of the more commonly used techniques to deal with multiaxial stress states is the principle of independent action (PIA) model.[4, 11] This model assumes that principal stress $\sigma_1 \geq \sigma_2 \geq \sigma_3$ act independently and if all principal stresses are tensile then the failure probability is equal to:

$$P_A = 1 - \exp\left(-\frac{1}{A_0}\int_A\left[\left(\frac{\sigma_1}{\sigma_0}\right)^m + \left(\frac{\sigma_2}{\sigma_0}\right)^m + \left(\frac{\sigma_3}{\sigma_0}\right)^m\right] dA\right) \tag{4.1}$$

$$P_V = 1 - \exp\left(-\frac{1}{V_0}\int_V\left[\left(\frac{\sigma_1}{\sigma_0}\right)^m + \left(\frac{\sigma_2}{\sigma_0}\right)^m + \left(\frac{\sigma_3}{\sigma_0}\right)^m\right] dV\right) \tag{4.2}$$

where P_A and P_V are the overall surface flaw and volumetric flaw based failure probabilities.

4.2 Probabilistic Design of Vessel

The design of structures made of a brittle material is done in a iterative way. First, continuum stress analysis is used to determine stress distribution in a structure, and the structure is modified to reduce the overall stress in the structure. Then, the statistical strength of the material is found experimentally to determine the design's reliability or, alternatively, probability of failure. Based on the desired reliability for the structure, the design must be modified to accommodate the reliability restrictions. In chapter 2 continuum mechanics were used to determine the stress distribution in the honeycomb pressure vessel. In this section, the statistical model for the pressure vessel is presented which will enable us to calculate the reliability of the vessel design given statistical strength information.

To enable an analytically solvable model of the honeycomb vessel, we model the

vessel as single cells acting structurally independent of each other. Each cell is constructed as as inner-wall section modeled as a cylindrical section acting independently of a top and bottom wall section modeled as a plate section. The following one-dimensional approximations of equations 4.2 and 4.1 are used to analyze the nearly radially-symmetric stress in the cell.

$$P_A = 1 - \exp\left(-\frac{1}{A_0}\int_A \left[\left(\frac{\sigma(r)}{\sigma_0}\right)^m\right] dA\right) \tag{4.3}$$

$$P_V = 1 - \exp\left(-\frac{1}{V_0}\int_V \left[\left(\frac{\sigma(r)}{\sigma_0}\right)^m\right] dV\right) \tag{4.4}$$

where P_A and P_V are the overall surface flaw and volumetric flaw based failure probabilities, r is the radial position, and A_0 and V_0 are the reference area and volume respectively. The two sections of the cell are illustrated in figures 4-1 and 4-2 respectively.

4.2.1 Cell Inner-Wall Modeled as Cylinder

The inner-walls of the cell are modeled as a cylindrical section with internal pressure in which stress occurs as an axisymmetric hoop stress. In reality, the inner cell walls are not perfectly cylindrical, there are external pressures acting on the wall due to the surrounding cells, and there is tension in the wall in the $z-$direction caused by the pressure on the top and bottom cell walls. It is believed that these forces would act to reduce the stress in the inner-wall section. Thus, the model of the inner-wall as a cylindrical section under internal pressure should give a reasonable estimate of the forces on the wall. The results from the FEM analysis done in section 2.2 showed that is more accurate to use a scaling of $1.75t$ in the place of the inner wall thickness t with a $3r/4$ fillet radius. This was done for the mass ratio calculations but is omitted from these calculations. A 1.5 factor-of-safety was also omitted from this model.

A cylinder with a uniform internal pressure, q, has a maximum principal stress

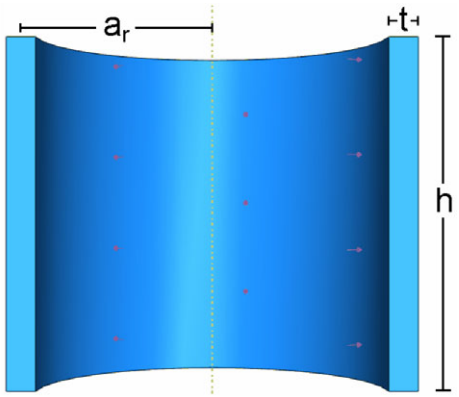

Figure 4-1: Illustration of cell cylindrical section

distribution due to hoop stress equal to the following:

$$\sigma_\theta = \frac{qa}{t} \tag{4.5}$$

For thin-walled cylinders, this stress is assumed to be uniform across the wall thickness. The failure probability of a structure can thus be expressed by substituting equation 4.5 into equations 4.3 and 4.4 to get:

$$\begin{aligned} P_A &= 1 \\ &\quad - \exp\left[\frac{-1}{A_0}\left(\int_0^h\int_0^{2\pi}\left(\frac{\sigma_\theta}{\sigma_0}\right)^m r d\theta\, dz\Big|_{r=a+t/2} + \int_0^h\int_0^{2\pi}\left(\frac{\sigma_\theta}{\sigma_0}\right)^m r d\theta\, dz\Big|_{r=a-t/2}\right)\right] \\ &\approx 1 - \exp\left[-\frac{4\pi ah}{A_0}\left(\frac{qa}{t\sigma_0}\right)^m\right] \end{aligned} \tag{4.6}$$

and

$$\begin{aligned} P_V &= 1 - \exp\left[-\frac{1}{V_0}\int_0^h\int_0^{2\pi}\int_{a-t/2}^{a+t/2}\left[\frac{\sigma_\theta}{\sigma_0}\right]^m r dr\, d\theta\, dz\right] \\ &\approx 1 - \exp\left[-\frac{2\pi ath}{V_0}\left(\frac{qa}{t\sigma_0}\right)^m\right] \end{aligned}$$

4.2.2 Cell Top and Bottom Wall Modeled as Clamped Plate

The top and bottom walls of the cell are modeled as a circular plate section that is clamped on the outer edge. Clamping was chosen in lieu of pinning because this kind of support resulted in the highest stresses. In reality, we expect the stress behavior of the top and bottom wall to be somewhere between a pinned and clamped plate but chose the clamped model in order to be most conservative.

A clamped circular plate with uniform pressure, q, applied from below has a maximum principal stress distribution of

$$\begin{aligned} \sigma_f &= K_t \frac{z M_r}{t^3/12} \\ &= K_t \frac{3q}{4t^3}\left[(3+\nu)\, r^2 z - (1+\nu)\, a^2 z\right] \end{aligned} \tag{4.7}$$

In this case, K_t is the stress concentration factor due to the fillet of the plate edge such as would be in the cell illustrated in figure 4-2

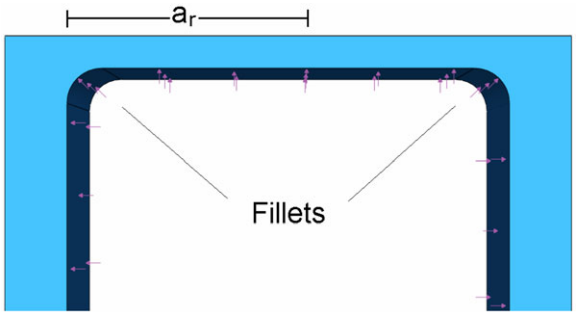

Figure 4-2: Illustration of cell plate section

The failure probability of this structure can thus be expressed by substituting equation 4.7 into equations 4.3 and 4.4 to get:

$$P_A = 1 - \exp\left(-\frac{1}{A_0}\int_0^{2\pi}\int_0^{a}\left[\left(\frac{\sigma_r\,(z=t/2)}{\sigma_0}\right)^m\right] r\,dr\,d\theta\right) \tag{4.8}$$

We only evaluate this equation at $z = t/2$ because the $z = -t/2$ surface will be in

compression. We note that:

$$\left(\frac{\sigma_r\left(z=t/2\right)}{\sigma_0}\right)^m = \left(K_t\frac{3q}{4t^3\sigma_0}\right)^m\left(\frac{t}{2}\right)^m\left[\left(3+\nu\right)r^2-\left(1+\nu\right)a^2\right]^m \tag{4.9}$$

Thus by substituting equation 4.9 into equation 4.8 we get:

$$\begin{aligned} P_A &= 1-\exp\left\{-\frac{1}{A_0}\left(K_t\frac{3q}{8t^2\sigma_0}\right)^m\int_0^{2\pi}\int_0^a\left[\left(3+\nu\right)r^2-\left(1+\nu\right)a^2\right]^m\,r dr\,d\theta\right\} \\ &= 1-\exp\left\{-\frac{2\pi}{A_0}\left(K_t\frac{3q}{8t^2\sigma_0}\right)^m\int_0^a\left[\left(3+\nu\right)r^2-\left(1+\nu\right)a^2\right]^m\,r dr\right\} \end{aligned} \tag{4.10}$$

and

$$\begin{aligned} P_V &= 1-\exp\left(-\frac{1}{V_0}\int_0^{t/2}\int_0^{2\pi}\int_0^a\left[\left(\frac{\sigma_r}{\sigma_0}\right)^m\right]\,r dr\,d\theta\,dz\right) \\ &= 1-\exp\left(-\frac{2\pi}{V_0}\left(K_t\frac{3q}{4t^3\sigma_0}\right)^m\int_0^{t/2}\int_0^a\left[\left(3+\nu\right)r^2-\left(1+\nu\right)a^2\right]^m z^m\,r dr\,dz\right) \end{aligned} \tag{4.11}$$

4.2.3 Multiple Cells

To account for the fact that there are multiple cells the probability must be adjusted. For systems with n cells failure will occur if one or more cells fail which is the same as:

$$\begin{aligned} P_{f_{total}} &= 1-P\left(\text{no vessel failure}\right) \\ &= 1-\left(1-P_f\right)^n \\ &\approx nP_f \end{aligned} \tag{4.12}$$

4.2.4 Designing for the Weakest Cell

As discovered in the chapter 3, an important consideration for a wafer-scale design is the weakest component of the wafer. For our purposes, this means the weakest cell in the cellular pressure vessel design will determine the entire vessel's achievable strength. This means that fabrication variation in geometry values that factor into stress distribution, and thus failure probability calculation, will have significant ef-

fects on the strength of the pressure vessel. These geometry factors include sidewall thickness, top and bottom wall thickness, and cell radius. For these reasons, it is important to monitor and control mask undercutting which affects the cell's sidewall thickness and cell radius. It is important to monitor and control etch depth variation across the wafer which effects the thickness of the top and bottom walls of the cells. The considerations of micron scale geometry variation for failure probability concerns is in addition to submicron geometry that effects strength variation across the wafer described in section 3.5.

4.2.5 Final Design Selection

This subsection goes through the process of determining the necessary material properties to achieve the desired reliability for our design. The equations derived in the last subsections can be integrated for a set of pressure vessel design parameters and over a range of σ_0 and m. In section 2.1 design criteria was made determining that failure probability should be between 10^{-6} and 10^{-8}. By keeping the failure probability a constant value of 10^{-8}, the values of σ_0 and m can be found for a single design. Pressure vessel geometric parameters can be found using the relations from chapter 2 for a given material stress σ_f, design pressure q_{design}, and volume. In other words, by specifying failure probability to be 10^{-8}, specifying material strength, σ_f, specifying a design volume of 5 cc, and specifying design pressure to be $\leq$ 15ksi the equations from the previous section can be solved for necessary Weibull material strength values σ_0 and m.

This computation was done with Matlab$^{\text{TM}}$and plotted against the previous work of Chen and Noonan in figure 4-3(b).[8, 31] Designs with material strengths, σ_f equal to 1 GPa and 1.76 GPa are plotted. Directly next to the Weibull parameters plot is the mass ratio plot for a given design material strength σ_f for comparison. We can see from figure 4-7(b) that the larger material stress σ_f that can be achieved, the lower the specific mass the design will have for the same design pressure. Conversely, the higher material stress, σ_f that is desired, the higher characteristic strength, σ_0, and Weibull modulus, m, must be achieved. A material stress as high as 1 GPa has been

achieved in the past as can be seen in the figure. A material stress of 1.76 GPa would be the material stress achieved if one could obtain both the highest characteristic strength achieved by Noonan with the highest Weibull modulus of Chen in a single material. Thus, reliably achieving a material stress of 1.76 GPa appears to be an achievable goal.

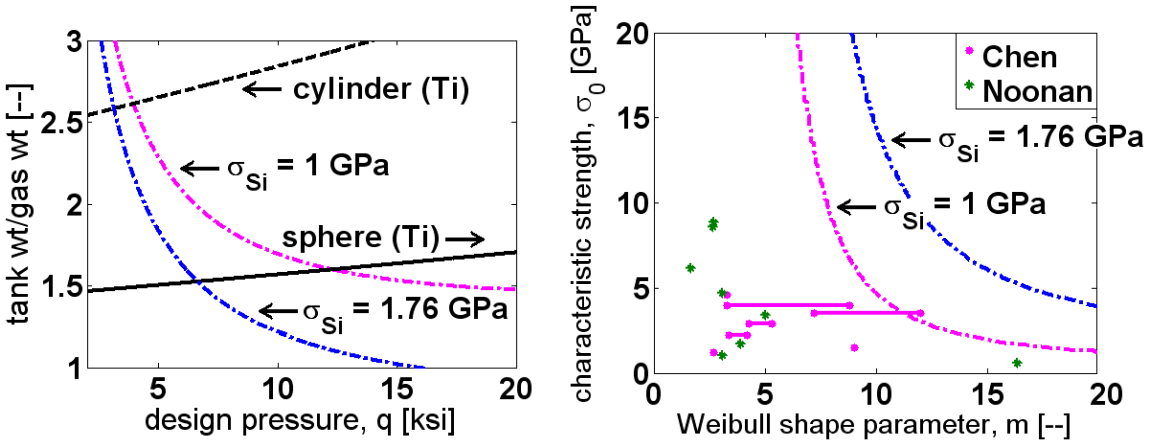

(a) Mass ratio

(b) Weibull parameters

Figure 4-3: Parameters for honeycomb vessel design with a 5 cc volume, failure probability of 10^{-8}, a design pressure $\leq$ 13 ksi, and for silicon strengths of 1 and 1.76 GPa

4.3 RHFS Test Data Reduction

Chapter 3 described the radiused hub flexure specimen (RHFS) testing methods and stress distribution. This section describes how that test data is used to determine material strength of silicon in terms of Weibull strength, σ_0, and Weibull modulus, m. Once σ_0 and m for the RHFS are found, they must be scaled to be applicable to the pressure vessel design since the two geometries vary in stress distribution, volume, and surface area. Once corresponding σ_0 and m values are determined for a given pressure vessel design, they can be substituted into the equations in section 4.2 to determine the probability of failure for any given pressure vessel design.

4.3.1 Correlating RHFS Data to Pressure Vessel

To correlate the RHFS data to the pressure vessel data, the characteristic strength, σ_0, and Weibull modulus, m, for the RHFS respectively represented by m_{RHFS} and σ_{RHFS} must first be found. Once Weibull parameters for the RHFS are found, they then can be scaled for the pressure vessel to predict m_{PV} and σ_{PV}.

Determining Weibull Parameters for the RHFS

To determine the characteristic strength, σ_{RHFS}, and Weibull modulus, m_{RHFS}, for the RHFS tests, the failure stress, σ_f, must be determined for each specimen. After the failure stress is found for each specimen, the data must be plotted and a linear fit must be made to determine the Weibull parameters.

The raw RHFS test data is in the form of maximum applied load which must first be converted to failure stress, σ_f, for each specimen. It is desirable to convert this maximum load data into a critical stress or failure stress, σ_f, and a location on the RHFS where the critical stress occurred. Since the desire of this work is to improve usable silicon strength, the location of the critical stress would prove valuable information to this end. The easiest way to convert the maximum load data into stress would be to assume that the failure for the RHFS occurred at the location of highest stress according to the stress distribution determined by ABAQUS$^{\text{TM}}$which is the hub root. In order to make this kind of assumption however, we would need to confirm in some kind of reliable way that failure in fact occurred at the hub. During actual experiments, it was often observed that the center hub of the RHFS would completely detach from the structure as shown in figure 4-4. As seen in section 3.5, this method has given Weibull strength data consistent with previous work.

Once the failure stress values are determined for the specimens, the Weibull parameters can be found. To calculate the Weibull parameters, the failure stress values are sorted so that they are in ascending order from $i = 1$ to N and they are each assigned a failure probability $P_f(i) = (i - 0.5)/N$, where N is the total number of test specimens. The data is plotted on a log-log scale with $log(1/(1 - P_f))$ on the

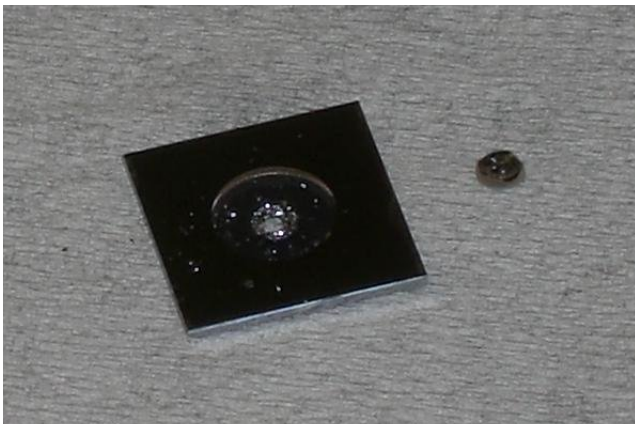

Figure 4-4: Failed RHFS where center hub has been detached

y-axis and $\sigma_f(i)$ on the x-axis. Finally, a linear fit is made to the data using the least-squares method. The resulting slope and intercept are the RHFS Weibull modulus and characteristic strength, m_{RHFS} and σ_{RHFS} respectively. These Weibull plots are provided in appendix D and a sample plot is shown in figure D-1

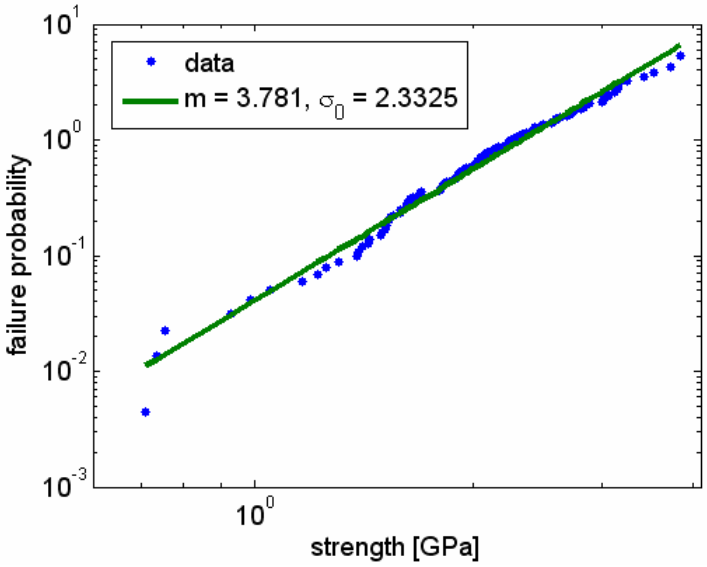

Figure 4-5: Weibull Distribution for 6 inch 650μm Thick Wafer with 1 minute SF_6 Smoothing and 112 Data Points

Scaling Data with Effective Area

After the Weibull parameters are determined for the RHFS, then the data must be scaled to determine Weibull parameters that can be achieved by the pressure vessel design. A structure under non-uniform stress can be considered as the sum of small elements under uniform stress. This way the probability of failure of the structure is simply the sum of the probability of failure of each small element under uniform stress. By considering a structure in this way, we can compare Weibull parameters between two structures made of the same material, with small differences in size, and the same manufacturing methods by a ratio of effective areas or effective volumes. The effective area or effective volume of the material can be defined by:

$$A_{eff} = \left(\frac{1}{\sigma_f}\right)^m \int_A (\sigma_1^m + \sigma_2^m + \sigma_3^m)\, dA \tag{4.13}$$

$$V_{eff} = \left(\frac{1}{\sigma_f}\right)^m \int_V (\sigma_1^m + \sigma_2^m + \sigma_3^m)\, dV \tag{4.14}$$

where σ_f is taken to be the maximum principle (tensile) stress in the model. The Weibull modulus, m, will remain the same between two different geometries. The characteristic strengths will be related in the following ways for surface and volume based flaws respectively:

$$\frac{\sigma_{PV}}{\sigma_{RHFS}} = \left(\frac{A_{eff_{RHFS}}}{A_{eff_{PV}}}\right)^{1/m} \tag{4.15}$$

$$\frac{\sigma_{PV}}{\sigma_{RHFS}} = \left(\frac{V_{eff_{RHFS}}}{V_{eff_{PV}}}\right)^{1/m} \tag{4.16}$$

where σ_x is the characteristic strength for the x geometry such that x is either the pressure vessel (PV) or the radiused hubbed flexure specimen (RHFS) and A_{eff_x} and V_{eff_x} are the effective areas and volumes related with the x geometry .[9] The $A_{eff_{PV}}$ and $V_{eff_{PV}}$ can be found substituting equations 4.5 and 4.7 into equations 4.13 and 4.14.

Determining the effective area of the RHFS requires knowing the stress distribution in the RHFS. This is done using a model for the RHFS given by Noonan.[31]

Noonan modeled the RHFS by superimposing two loading conditions. The first loading condition is a plate with a circular hole in the middle subject to a bending moment. The second case is a plate with a circular hole in the center subject to a shearing force. This combination is illustrated in figure 4-6. This model will result in equations for radial and tangential components of stress, σ_r and σ_t that can then be substituted into equations 4.13 and 4.14. The analysis given by Noonan assumes the membrane

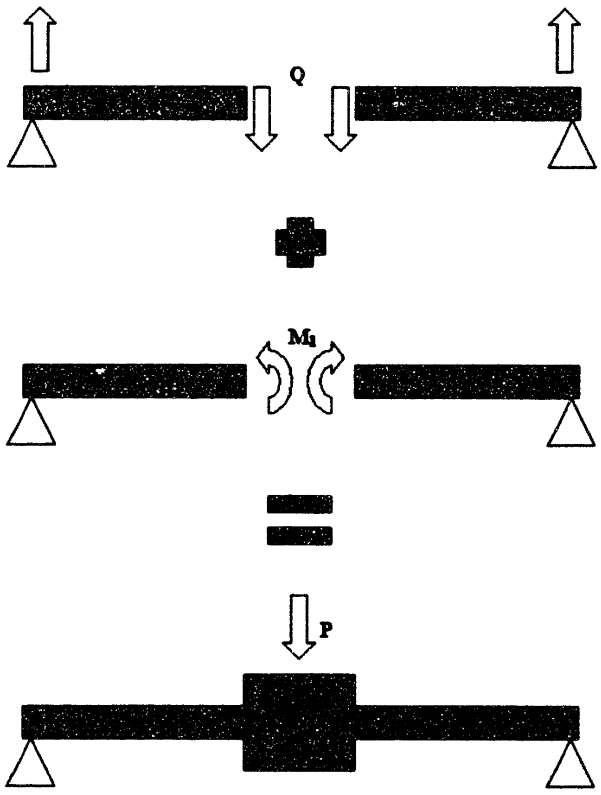

Figure 4-6: Noonan model for RHFS

is thin and does not consider stress variation through the thickness of the membrane plate. Thus, the only principle stresses used in effective area and volume calculations are the radial and transverse principal values while the third principal stress is not used in equation 4.13 and 4.14. The thickness of the plate would thus become a constant multiple difference between the effective area and the effective volume.

Table 4.1: Comparison of RHFS A_{eff} Calculations with Noonan.

Noonan RHFS Data without Kt				
	MIT 69	**MIT69+SF$_6$**	**ADAM06**	**ADAM06+SF$_6$**
m	2.706	2.358	4.542	2.523
σ_{RHFS} **[GPa]**	1.963	3.450	1.493	3.985
$A_{eff_{RHFS}}$ **[m^2]**	$7.26E{-}7$	$1.07E{-}6$	$1.12E{-}7$	$8.73E{-}7$
Garza RHFS Analytical Model Values without Kt				
$A_{eff_{RHFS}}$ **[m^2]**	$2.17E{-}6$	$2.82E{-}6$	$1.01E{-}6$	$2.46E{-}6$
Noonan RHFS Data with Kt				
m	2.961	2.524	4.788	2.572
σ_{RHFS} **[GPa]**	4.691	8.584	3.402	8.821
$A_{eff_{RHFS}}$ **[m^2]**	$5.48E{-}7$	$8.90E{-}7$	$9.07E{-}8$	$8.43E{-}7$
Garza RHFS Analytical Model Values with Kt				
$A_{eff_{RHFS}}$ **[m^2]**	$1.94E{-}6$	$2.46E{-}6$	$9.59E{-}7$	$2.46E{-}6$

Validation of Model

It is valuable to validate the model discussed in the last section by comparing effective areas calculated with the model to Noonan's values found using stress distribution results found through the ABAQUS^{TM}model integrated discretely using the NASA CARES program. The NASA CARES program was originally developed at NASA Glenn to calculate failure probability of macroscopically isotropic ceramic components. The CARES program has subsequently been transferred to a company called Connecticut Reserve Technologies.[29] In this research we hypothesize that the majority of failure causing flaws are those on the surface introduced by the fabrication process. So we consider effective area to validate the model, we substitute the resulting σ_r and σ_t given by Noonan's analytical model into equation 4.13 and compare the results in table 4.1.

The difference between the effective areas calculated by Noonan's CARES calculation and the analytical calculation I did range from a factor of about 3 in most of the cases to a factor of 11 difference in the ADAM06 DRIE recipe case. I believe this difference in the models exist because of the crudity of my model compared with the FEM model used with CARES that Noonan had.

4.3.2 Predictions for Pressure Vessel

The model presented in this chapter is used to predict achievable strength of a honeycomb silicon pressure vessel based on RHFS results. The stress distributions given in equation 4.5 and 4.7 can be substituted into equation 4.13 to calculate the effective area of the pressure vessel design considered in section 4.2.5 which can then be substituted into equation 4.15 with RHFS data and effective area calculations to find the characteristic strength predicted for the pressure vessel design from the RHFS experiments. The results of this analysis is plotted on figure 4-7. Figure 4-7(a) includes scaled RHFS from this work in black, from Chen's work in pink, and from Noonan's work in green. Lines of constant design are depicted for both the strongest results of this work and Chen's work and show a maximum allowable pressure vessel stress of 300MPa and 450MPa respectively. It is apparent from the figure 4-7(b) that **pressure vessel designs with the maximum stresses produced in this work will not be sufficient to produce a competitive silicon pressure vessel design**.

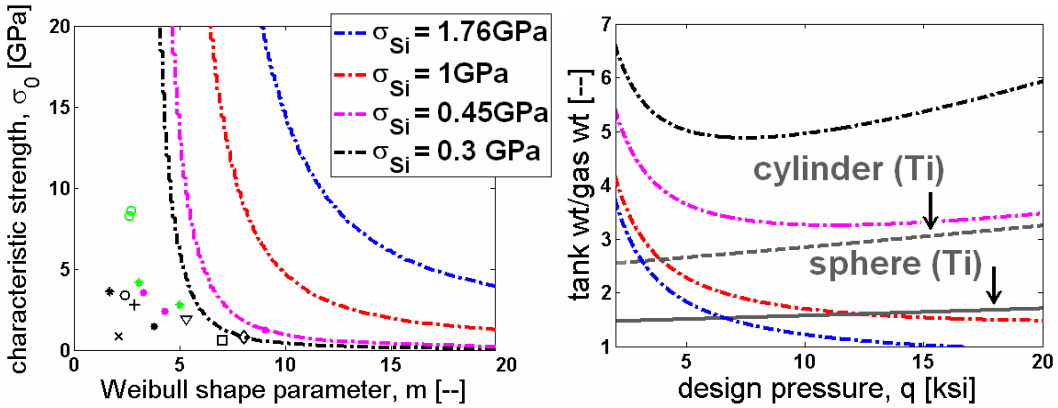

(a) Weibull parameters

(b) Mass ratio

Figure 4-7: Predictions for achievable silicon pressure vessel strength plotted with parameters for honeycomb vessel design with a 5 cc volume, failure probability of 10^{-8}, a design pressure $\leq$ 13 ksi, and for silicon strengths of 1 and 1.76 GPa

4.3.3 Wafer-Scale Implications

This model which correlates RHFS data to pressure vessel data can be used to evaluate across wafer strength variation implications for the strength of a wafer-scale pressure vessel. Using this model and combining it with strength variation results from data subsets taken in section 3.5 we see strength variations as high as 1400% as can be seen in table 4.2 for data taken only from radial positions r such that 35mm $< r <$ 65mm from the full wafer values. These strength improvements for the 35mm $< r <$ 65mm subsections of the wafer were reproducible for all the 6" wafer data.

Table 4.2: Variation in predicted pressure vessel strength across wafer for each RHFS data set

	Full Wafer Data	**35mm $< r <$ 65mm Data**	
RHFS Data Set	**Maximum Pressure Vessel Stress [MPa]**	**Maximum Pressure Vessel Stress [MPa]**	**% increase**
6"+SF_6	60	225	275
6"+SF_6+Ox	13	90	592
4"+SF_6	3	5	67
4"+SF_6 +0.5hr H_2	210	170	-19
4"+SF_6 +2.5hr H_2	300	200	-33
500μm 6" +6xSF_6	27	61	126
500μm 6" +6xSF_6+Ox	1	15	1400
650μm 6"+SF_6 +Ox+UHV	196	289	47

4.4 Conclusions

This chapter has described how the probabilistic nature of single crystal silicon is modeled for the pressure vessel design. The applicability and basic nature of the Weibull statistics used for the design and analysis was described. An analytical model of the

pressure vessel was presented and integrated into a simplified two-parameter Weibull model. That model was used to explore Weibull material parameters characteristic strength, σ_0, and Weibull modulus, m, necessary for pressure vessel designs that vary by achievable silicon strength. Finally, RHFS silicon strength data was used to determine the achievable strength values for the final pressure vessel design. It was found that significant improvements to usable silicon strength are still required for a competitive silicon pressure vessel design to be realized.

Chapter 5

Conclusions and Recommendations

This chapter offers some concluding remarks on the research done and recommendations for future work.

5.1 Summary of Usable Silicon Strength Work

The major results of the RHFS testing are the following. It is believed the SF_6 smoothing is a valuable first order smoothing to improve silicon strength. SF_6 smoothing must be done long enough to remove large visible changes in sidewall roughness such as overhanging, undercut silicon protrusions such as those illustrated on figure 5-1. It is necessary to remove any silicon overhang to properly analyze the solid sidewall morphology produced by DRIE.

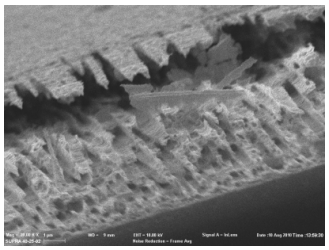

Figure 5-1: RHFS trench sidewall

Silicon oxidation and removal is a possible tool to improve silicon characteristic strength but is not valuable for reliably improving overall strength and reliability of silicon structures. It was shown that oxidation can result in both strength improvement and strength loss. It is believed that this variability in the results of oxidation for strength recovery are result of non-uniform silicon consumption known as oxidation sharpening.[26, 27]

Surface migration is a valuable second order smoothing technique which can be used in addition to SF_6 smoothing to improve silicon strength, however, more favorable annealing conditions and long annealing times are needed to make significant improvement on silicon strength which would be best done with a dedicated annealing system.

Strength of DRIE silicon structures can vary dramatically across the wafer due to submicron sidewall morphology variation across the wafer. Strength uniformity across a wafer is a separate concern from the uniformity of design geometry across the wafer. Etch variation can be clearly seen by sidewall etch variation across the wafer. Submicron DRIE sidewall morphology affecting strength variation over the wafer acts independent of micron scale and larger design geometry variation across the wafer. This strength variation is reproducible and can mean nearly an order of magnitude loss in strength between its strongest and weakest sub-element. Wafer-scale DRIE brittle devices are only as strong as their weakest sub-element given the nature of brittle material. One can obtain higher strengths for die-level silicon devices by omitting silicon devices produced in the central and outer regions of a 6" DRIE silicon wafer.

Finally, as can be seen in figure 3-8, this research did not have sufficient resources to achieve significant improvement in overall usable silicon strength represented by shifts to the right and up of a line of constant failure probability. It is believed that improvements in silicon strength on a wafer-scale macro-structure cannot be done simply with a strength recovering technique following DRIE. Improvements in usable silicon strength must involve careful tuning of DRIE recipes and machine parameters so that submicron sidewall roughness over the wafer does not vary significantly over the wafer in addition to controlling larger micron scale geometry variations over the wafer. Care must also be taken to avoid possible strength reducing steps such as mounting onto a handler wafer during DRIE or to improve resultant strength from the mounting process.

5.2 Summary of Pressure Vessel Design Work

A 5cc single crystal pressure vessel design with a honeycomb array of pressurized cells has been developed. The design utilizes material advances and the unique fabrication abilities of the MEMS industry. The vessel has the potential of lower specific mass ratios than conventional designs for pressures above 6000 psi if the unable strength of single crystal silicon could be substantially improved. Although this work was able to find methods to improve silicon usable strength, it also found limitations that would require more study and resources before strength improvements to microfabricated silicon could produce a pressure vessel design which is advantageous over conventional designs.

5.3 Contributions

This work is the first known to evaluate wafer-scale single crystal silicon for macro-scale structural applications. This research has identified a promising application of macro-scale structural silicon and discovered a number of phenomena that affect wafer-scale structural silicon application.

This research identified cellular microfabricated silicon pressure vessels as a promising wafer-scale silicon device. This work is the first to identify design criteria for brittle pressure vessels and specifically microfabricated silicon pressure vessels. This research has quantified metrics required to be competitive with conventional pressure vessel designs. This work has introduced a graphical way of identifying and comparing improvements and reductions of Weibull strength data for a device design.

Previously unreported mechanisms by which DRIE silicon is compromised were identified. Overhanging, curtain-like silicon structures that were produced by DRIE in this work was shown to mask significantly different sidewall morphology underneath which changes flaw size implications for strength. This research has also elucidated the role of wafer-level strength variation, its effect on usable silicon strength, and its independence from variation of geometric features across a wafer.

Finally, it was determined that promise for competitive silicon pressure vessel designs is dependant on further work on across wafer strength uniformity and strength recovering surface smoothing techniques. The achievement of high useable single crystal silicon strength is likely to result from the accumulation of small improvements of strength from a variety of different adjustments to processing rather than a single strength recovering step.

5.4 Discussion

This work setout to explore usable strength of silicon for macro-world structural applications and aerospace applications. It was hypothesized that the high theoretical strength of silicon combined with its low density could overcome geometric inefficiencies of microfabrication limitations to offer competitive pressure vessel designs. It was also hypothesized that promising surface smoothing techniques such as surface migration could significantly improve usable silicon strength. This section reviews these hypothesis given the research results. This section also identifies what sets this work apart from previous work in this area.

5.4.1 Improvements in Usable Silicon Strength

It is necessary to ask if this research was able to significantly improve on the strength data achieved by previous researchers as was hypothesized. In this case, comparisons could be directly made to the work of Chen and Noonan because the same RHFS structural test sample was used. Figure 3-8 compares RHFS test data found in this research with that of Chen and Noonan. From this plot it would appear that Chen's work was able to achieve the highest strength out of all RHFS work done by a significant amount. His highest strength values were achieved by omitting outlier data points. If values of strength are taken from full data sets for which outlier data have not been omitted, which would be most representative of strength data for a wafer-scale device, we find the the highest values for strength from this work and Noonan's work fall on the same line of constant failure probability. This work and

the work of Noonan is improved from Chen's work where data has not been omitted.

There are a few reasons why this work did not have significantly higher strength values than previous work when improvements from surface migration are omitted. We omit results from surface migration from this comparison because the ability to perform surface migration at optimal conditions could not be done given this research's resources. The first and considered most likely reason proposed for the lack of strength improvement from previous work is the unavoidable differences in the DRIE recipes used. Previous work was done with a different machine in the case of Chen and with a different recipe in the case of Noonan. Even in a case where wafers are etched with the same machine there are drifts over time in the machine input to the results produced. Although some time was spent in this work making the DRIE recipe produce favorable u-shaped trench bottoms, no time was spent tuning the recipe for improved strength results which could have contributed to higher strengths. It is also believed that other variations in the processing between the RHFS in this work and previous work could have played small parts in affecting the DRIE etch that added up to non-negligible differences in maximum obtainable strength. These small differences in the steps could, for example, be differences in photoresist thickness, uniformity, bake times, and exposure dosages that could make the etch mask produce different sidewall morphology. Other possible differences in processing that could have affected resultant strength is the density of RHFS on a wafer which would effect the DRIE as well as the use of oxide mask reinforcement which was not used by Chen. The results for the DRIE strength variation across the wafer makes us believe that each processing step could have played a small part in DRIE and strength differences from this work and that of previous researchers.

5.4.2 Further Comparison to Previous Work

Silicon strength work done by this research differed from that of Chen, Noonan and other researchers in a number of ways. First off, this research analyzed wafer scale silicon strength in addition to device level silicon strength as opposed to previous work which only analyzed device level silicon strength. Although work has been done for

wafer-level strength in the past, this is the first work to analyze wafer-level strength with etched features. This research was the first to analyze silicon oxidation and surface migration for strength recovery. This research also evaluated longer SF_6 etches than previous work for strength recovery which revealed DRIE sidewall morphology that could not be identified from shorter SF_6 etch times. This work also evaluated strength loss from wafer mounting versus no wafer mounting.

This work was not the first to evaluate silicon pressure vessel designs as Noonan looked at important silicon pressure vessel design parameters. This work was first, however, to identify design criteria for brittle material and silicon pressure vessels as well. This research also considered much larger wafer-scale pressure vessel designs and evaluated alternative configurations to the single monocellular convention. Finally, this work was the first to define numerical metrics so that silicon pressure vessel designs might be competitive with conventional pressure vessel designs.

5.4.3 Prospects for Further Research

It is believed that this is a promising field in which to continue research. Although prospects for a silicon pressure vessels may be quite far off, structural applications of silicon are quite abundant in the current market place. Advances in uniformity in across-wafer silicon strength can be useful for higher yield of micro-scale devices and can make way for devices covering bigger areas of a wafer for bigger versions of micro-scale devices. The results of this research lead us to believe that alterations to DRIE recipes and more work with surface migration with dedicated equipment can lead to further improvements to usable silicon strength that can eventually add to significant improvements to usable silicon strength.

5.4.4 Lessons Learned

There were a number of important lessons learned during this research that are worth summarizing.

It was learned that DRIE recipe turning must be done for submicron sidewall

morphology variation in addition to larger geometric features. For this research the DRIE etch recipe was tuned until u-shaped trench bottoms and circular trench fillets were achieved. It was believed that these geometric features would ensure high strength and that surface smoothing strength recovery techniques would take care of surface roughness. We now know however, that DRIE sidewall morphology can vary significantly across the wafer despite little trench shape variation across the wafer. We also know that the DRIE sidewall morphology is the most likely indicator of silicon strength variation across the wafer.

Surface migration in UHV is highly dependent on native oxide removal. It was determined from trial and error that annealing at high temperature in UHV to improve silicon strength cannot occur without completely removing silicon native oxide immediately before annealing with Hydrofluoric acid. Data was taken for wafers which were UHV annealed but for which the native oxide was not sufficiently removed. This data had no strength improvement from the baseline work. This data was not included in the thesis for this reason although provided a valuable lesson on the importance of native oxide removal before annealing.

A final important lesson learned was the value of SEM inspection of submicron features on device areas of high stress. SEM measurements were not taken of RHFS sample sets until later in the research because it was thought that simply looking at sidewall cross-sections with an optical microscope would give a reasonable indication of geometry variation across the wafer when in fact there was discovered to be substantial submicron sidewall variation occurring which shed light on strength variation across the wafer. SEM inspections also elucidated overhanging silicon walls which masked underlying silicon sidewall morphology. All available methods of sample inspection are of value in strength recovery work involving surface smoothing.

5.5 Future Work

This section describes recommendations for future work to continue this research. It is believed that the following suggestions are promising steps towards developing high

strength macro-scale silicon structures, particularly a high pressure vessel design for aerospace applications that is competitive with conventional pressure vessel designs on a small scale.

5.5.1 Tuning Etch Conditions

The strength recovery done in this research could be improved by:

1. adjusting the DRIE etch recipe to improve strength variation over the silicon wafer

2. doing longer surface migration annealing on 6 inch wafers etched without mounting on a handler wafer

Some time was spent on task 1. above working on adjusting the DRIE recipe so that the bottom corner of the DRIE etch gave a round fillet when its cross-section was viewed with an optical microscope. Time was not spent however, looking at the effect of the DRIE etch on the sidewalls with a SEM over a whole radial slice of the wafer. I believe looking at sidewall roughness patterns over all radial points over the wafer while adjusting the DRIE recipe will improve both overall strength and strength variation. Item 2. could not be achieved in this research because obtaining a resource for surface annealing was difficult in itself. Being able to surface migration for long periods of time without having to compromise the wafer with mounting during DRIE is promising for strength recovery.

5.5.2 Experimental Evaluation of Pressure Vessel Features

If sufficient usable silicon strength could be obtained, a microfabricated silicon pressure vessel design may become viable. For such a case, a coupon to test key pressure vessel features was considered and a model for such a specimen was explored. A description of pressure vessel coupon design, fabrication, and computational modelling is described in appendix E

Appendix A

Detailed Si Pressure Vessel Calculations

A.1 Investigation of Designs from First Principles

A.1.1 Honeycomb Vessel

The following calculations determine material and gas volume based on an assumed number of cellular layers n and a cylindrical radius r.

The total number of cells, C can be found as a function of the number of cellular layers n:

$$\begin{aligned} C &= 1(\text{for n=1}), 7(\text{for n=2}), 19(\text{for n=3}), 37(\text{for n=4}), 61(\text{for n=5}), \\ &= 1 + \sum_{i=1}^{n} 6\,(n-1) \\ &= 1 - 6n + 6\sum_{i=1}^{n} n \\ &= 1 - 6n + 6\frac{(n+1)(n)}{2} \\ &= 3n^2 - 3n + 1 \end{aligned}$$

The total number of outer edges of the vessel will be:

$$\begin{aligned} E &= 6(\text{for n=1}), 18(\text{for n=2}), 30(\text{for n=3}), 42(\text{for n=4}) \\ &= 12(n-1)+6 \\ &= 12n-6 \end{aligned}$$

Assuming each individual cell is a cylinder with spherically capped ends implies the maximum material stress will be given by equation 2.1:

$$t = FOS\frac{qr}{\sigma_f}$$

where r is the cell cross-sectional radius, σ_f is the fracture strength of the silicon, FOS is the vessel factor-of-safety, and q is the maximum operating pressure of the vessel.

For a hexagonal cell the side length s will be:

$$s = \frac{2r+t}{\sqrt{3}}$$

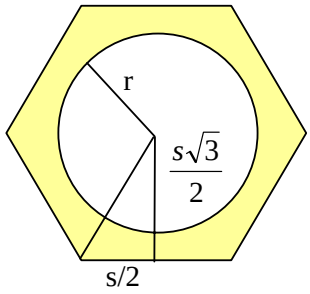

Figure A-1: Single honeycomb cell

Taking a cross-section parallel to the wafer plane, reveals a cell open area and material area of:

$$\begin{aligned} A_{open} &= C\pi r^2 \\ A_{material} &= C\left(\frac{3\sqrt{3}}{2}s^2\right) + E\frac{t}{2}s - A_{open} \end{aligned}$$

respectively.

The longitudinal stress in the individual cells is half that of the hoop stress which implies that:

$$t_{top-bottom} = t$$

will be twice as effective as needed to withstand internal pressure.

In order for these cell to be considered "thin-walled" structures, the following restriction must be met:

$$h \leq 5t$$

This implies that the open area volume will be:

$$V = A_{open}h + C\frac{4}{3}\pi r^3$$

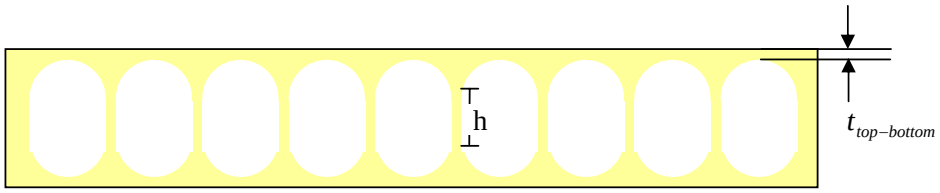

Figure A-2: Illustration of honeycomb vessel cross-section through wafer plane

The structural volume SV thus will equal:

$$\begin{aligned}
SV &= \left(A_{material} + A_{open}\right)\left(h + 2r + 2t_{top-bottom}\right) - V \\
&= \left(\frac{C\sqrt{3}}{2}\left(4r^2 + 4rt + t^2\right) + E\frac{2rt + t^2}{2\sqrt{(3)}}\right)(h + 2r + 2t) - V \\
&= \left(\left(\frac{C\sqrt{3}}{2} + \frac{E}{2\sqrt{3}}\right)t^2 + \left(2C\sqrt{3} + \frac{E}{\sqrt{3}}\right)rt + 2C\sqrt{3}r^2\right)(h + 2r + 2t) - V \\
&= \left(C\sqrt{3} + \frac{E}{\sqrt{3}}\right)t^3 + \left[(h + 2r)\left(\frac{C\sqrt{3}}{2} + \frac{E}{2\sqrt{3}}\right) + \left(4C\sqrt{3} + \frac{2E}{\sqrt{3}}\right)r\right]t^2 \\
&\quad + \left[(h + 2r)\left(2C\sqrt{3} + \frac{E}{\sqrt{3}}\right)r + 4C\sqrt{3}r^2\right]t + 2\left(h + 2r\right)C\sqrt{3}r^2 - V \\
&= \left(C\sqrt{3} + \frac{E}{\sqrt{3}}\right)\left(\frac{FOS \cdot r}{\sigma_f}\right)^3 q^3 \\
&\quad + \left[(h + 2r)\left(\frac{C\sqrt{3}}{2} + \frac{E}{2\sqrt{3}}\right) + \left(4C\sqrt{3} + \frac{2E}{\sqrt{3}}\right)r\right]\left(\frac{FOS \cdot r}{\sigma_f}\right)^2 q^2
\end{aligned}$$

$$+\left[(h+2r)\left(2C\sqrt{3}+\frac{E}{\sqrt{3}}\right)r+4C\sqrt{3}r^2\right]\left(\frac{FOS\cdot r}{\sigma_f}\right)q$$
$$+2\,(h+2r)\,C\sqrt{3}r^2-V$$

Thus, the specific volume will be;

$$\begin{aligned}\frac{SV}{V} &= \frac{\left(C\sqrt{3}+\frac{E}{\sqrt{3}}\right)(FOS\cdot r)^3}{V\sigma_f^3}q^3 \\ &+\frac{\left[(h+2r)\left(\frac{C\sqrt{3}}{2}+\frac{E}{2\sqrt{3}}\right)+\left(4C\sqrt{3}+\frac{2E}{\sqrt{3}}\right)r\right](FOS\cdot r)^2}{V\sigma_f^2}q^2 \\ &+\frac{\left[(h+2r)\left(2C\sqrt{3}+\frac{E}{\sqrt{3}}\right)r+4C\sqrt{3}r^2\right](FOS\cdot r)}{V\sigma_f}q \\ &+\left[\frac{2\,(h+2r)\,C\sqrt{3}r^2}{V}-1\right]\end{aligned}$$

Specific volume can be converted to specific mass using the conversion 2.2.

The following plots show the variation in specific tank mass for various internal volumes with a constant internal pressure and various internal pressure with a constant internal volume.

From these plots we see that the specific structural mass increases with increasing internal volume. The structural mass of the tank decreases as pressure is increased. The structural mass of the vessel decreases with cell height. the specific structural mass of the tank decreases with increasing cell number.

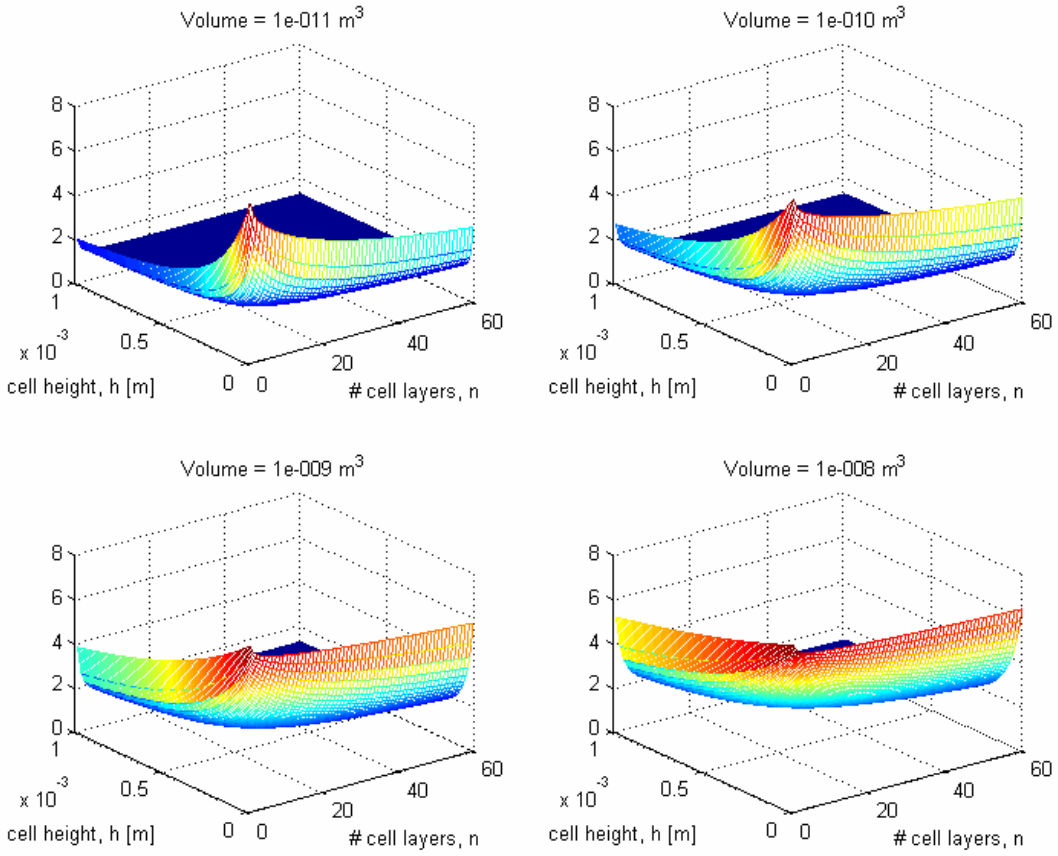

Figure A-3: Specific Tank Mass versus Cell # and Height for Honeycomb Design (varied volume and constant pressure)

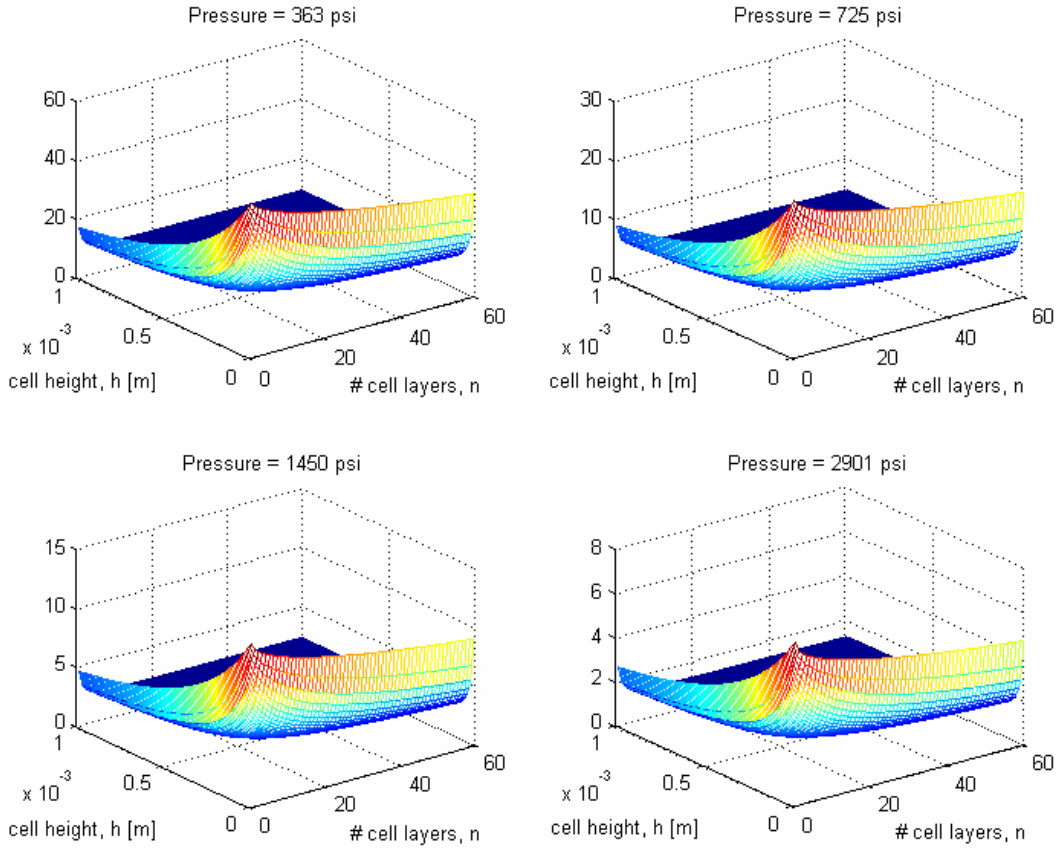

Figure A-4: Specific Tank Mass versus Cell # and Height for Honeycomb Design (varied pressure and constant volume)

A.1.2 Concentric Tori Vessel

This tank structure consists of a center spherical tank or radius r surrounded by n toroidal tanks such that:

$$r = b_1 = b_2 = b_3$$

The first wall thickness t_1 should be such that:

$$\begin{aligned} t_1 &= max[t_{sphere}, t_{torus1}] \\ t_{sphere} &= FOS\frac{qr}{\sigma_f} \\ t_{torus1} &= FOS\frac{qb_1}{2\sigma_f}\frac{2a_1 - b_1}{a_1 - b_1} \\ &= FOS\frac{qr}{2\sigma_f}\frac{2(2r + t_1) - r}{(2r + t_1) - r} \\ &= FOS\frac{qr}{2\sigma_f}\frac{2(r + t_1) + r}{r + t_1} \\ &= FOS\frac{qr}{\sigma_f}\frac{r}{r + t_1} \end{aligned}$$

Since $\frac{r}{r+t_1} < 1$, this implies:

$$t_1 = t_{sphere}$$

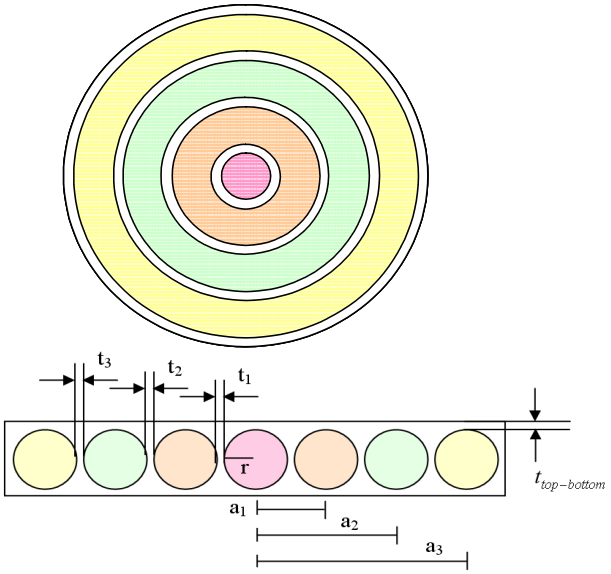

Figure A-5: Illustration of planer and through plane cross-sections of concentric tori vessel

For the general equation:

$$t_{torus} = FOS\frac{qb}{2\sigma_f}\frac{2a - b}{a - b}$$

t_{torus} decreases as a increases which implies that:

$$t_i = t_{torus(i-1)} = FOS\frac{qb_{(i-1)}}{2\sigma_f}\frac{2a_{(i-1)} - b_{(i-1)}}{a_{(i-1)} - b_{(i-1)}}$$

for $i > 1$. Now that b_i and t_1 is known, we can solve for

$$a_1 = r + t_1 + b_1 = 2r + t_1$$

and continue with

$$\begin{aligned} b_i &= r \\ t_i &= FOS\frac{qb_{(i-1)}}{2\sigma_f}\frac{2a_{(i-1)} - b_{(i-1)}}{a_{(i-1)} - b_{(i-1)}} = FOS\frac{qr}{2\sigma_f}\frac{2a_{(i-1)} - r}{a_{(i-1)} - r} \\ a_i &= r + \sum_{k-1}^{i} t_k + \sum_{k=1}^{i-1} 2b_k + b_i = 2ir + \sum_{k=1}^{i} t_k \end{aligned}$$

Thus, to maintain a sufficiently strong upper and lower wall, the following must be true:

$$t_{top-bottom} = max\left[t_{sphere}, t_{torus(i)}\right] = t_{sphere} = FOS\frac{qr}{\sigma_f}$$

The internal volume of the tank thus will be:

$$V = \frac{4}{3}\pi r^3 + 2\pi^2 r^2 \sum_{k=1}^{n} a_k$$

The structural volume will be:

$$\begin{aligned} SV &= \pi\left(a_n + r + t_{n+1}\right)^2\left(2r + 2t_{top-bottom}\right) - V \\ &= 2\pi r\left(r\left(2n+1\right) + \sum_{k=1}^{n+1} t_k\right)^2\left(1 + \frac{FOS}{\sigma_f}q\right) - V \\ &= 2\pi r^3\left(\left[\frac{FOS}{\sigma_f}\beta\right]q + \left(2n+1\right)\right)^2\left(1 + \frac{FOS}{\sigma_f}q\right) - V \end{aligned}$$

where $\beta = \sum_{k=1}^{n+1}\left(\frac{a_{(k-1)} - \frac{r}{2}}{a_{(k-1)} - r}\right)$. Thus we continue the derivation to get:

$$SV = \left(2\pi r^3\left(\frac{FOS}{\sigma_f}\right)^2\beta^2 q^2 + 4\pi\left(2n+1\right)r^3\left(\frac{FOS}{\sigma_f}\right)\beta q + 2\pi\left(2n+1\right)^2 r^3\right)$$

$$
\begin{aligned}
&\cdot \left(\frac{FOS}{\sigma_f} q + 1\right) - V \\
= \;& 2\pi r^3 \left(\frac{FOS}{\sigma_f}\right)^3 \beta^2 q^3 + 4\pi \left(2n+1\right) r^3 \left(\frac{FOS}{\sigma_f}\right)^2 \beta q^2 + 2\pi \left(2n+1\right)^2 r^3 \left(\frac{FOS}{\sigma_f}\right) q \\
& + 2\pi r^3 \left(\frac{FOS}{\sigma_f}\right)^2 \beta^2 q^2 + 4\pi \left(2n+1\right) r^3 \left(\frac{FOS}{\sigma_f}\right) \beta q + 2\pi \left(2n+1\right)^2 r^3 - V \\
= \;& 2\pi r^3 \left(\frac{FOS}{\sigma_f}\right)^3 \beta^2 q^3 + 2\pi r^3 \left(\frac{FOS}{\sigma_f}\right)^2 \left[\beta^2 + 2\left(2n+1\right)\beta\right] q^2 \\
& + 2\pi \left(2n+1\right) r^3 \left(\frac{FOS}{\sigma_f}\right) \left[2n + 1 + 2\beta\right] q + 2\pi \left(2n+1\right)^2 r^3 - V
\end{aligned}
$$

Thus, the specific volume for the concentric tori vessel will be:

$$
\begin{aligned}
\frac{SV}{V} = \;& \frac{2\pi r^3}{V} \left(\frac{FOS}{\sigma_f}\right)^3 \beta^3 q^3 + \frac{2\pi r^3}{V} \left(\frac{FOS}{\sigma_f}\right)^2 \left[\beta^2 + 2\left(2n+1\right)\beta\right] q^2 \\
& + \frac{2\pi \left(2n+1\right) r^3}{V} \left(\frac{FOS}{\sigma_f}\right) \left[2n + 1 + 2\beta\right] q + \left[\frac{2\pi \left(2n+1\right)^2 r^3}{V} - 1\right]
\end{aligned}
$$

Specific volume can be converted to specific mass using the conversion 2.2.

The following plots show the variation in specific tank mass for various internal volumes with a constant internal pressure of 200 bar and various internal pressures with a constant internal volume of 10^{-10} m^3.

The specific structural mass increases with increasing internal volume. The structural mass of the tank decreases as pressure is increased. The structural mass of the vessel decreases with cell height. The specific structural mass of the tank decreases with increasing cell number.

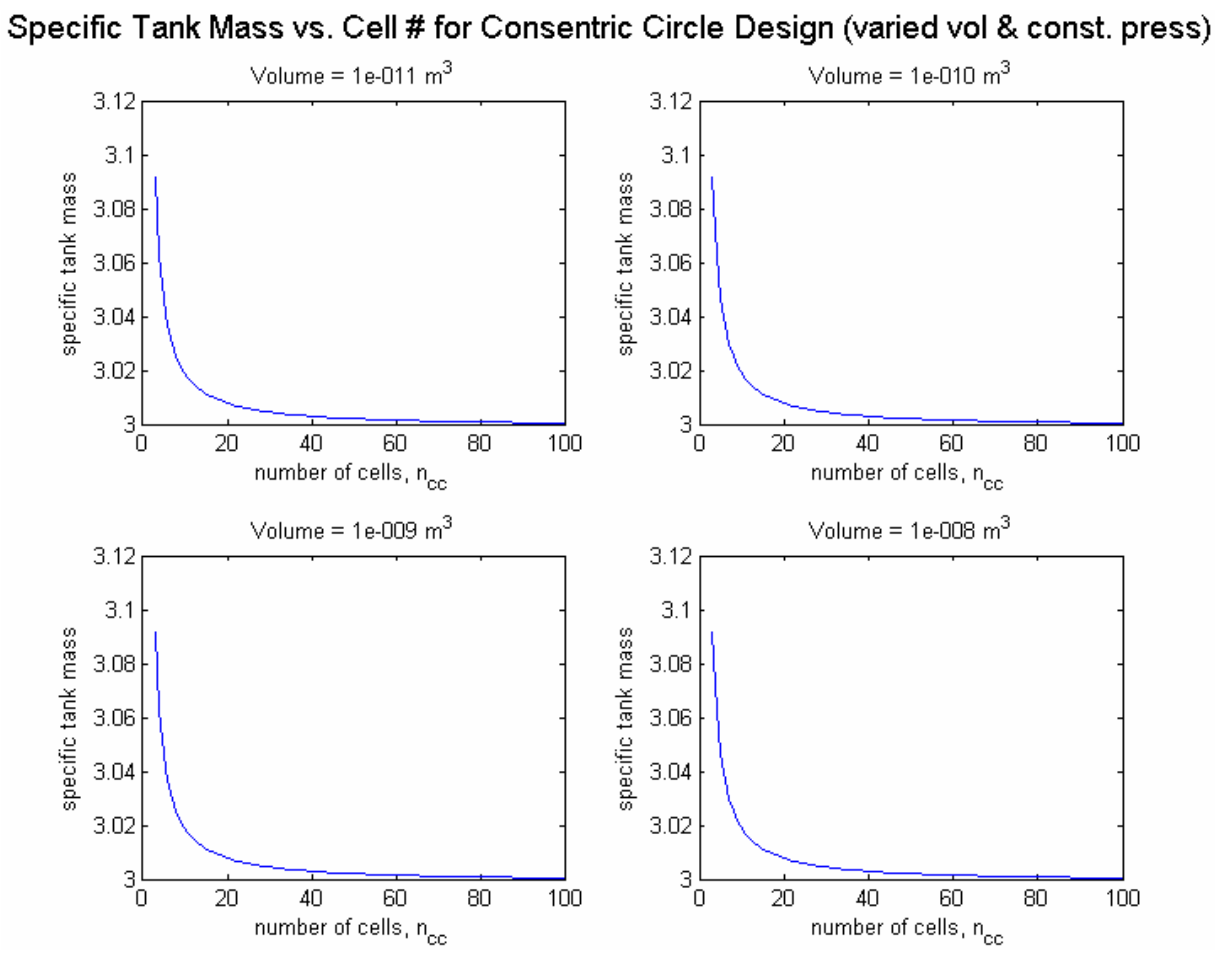

Figure A-6: Specific Tank Mass versus Cell # and Height for Concentric Tori Design (varied volume and constant pressure)

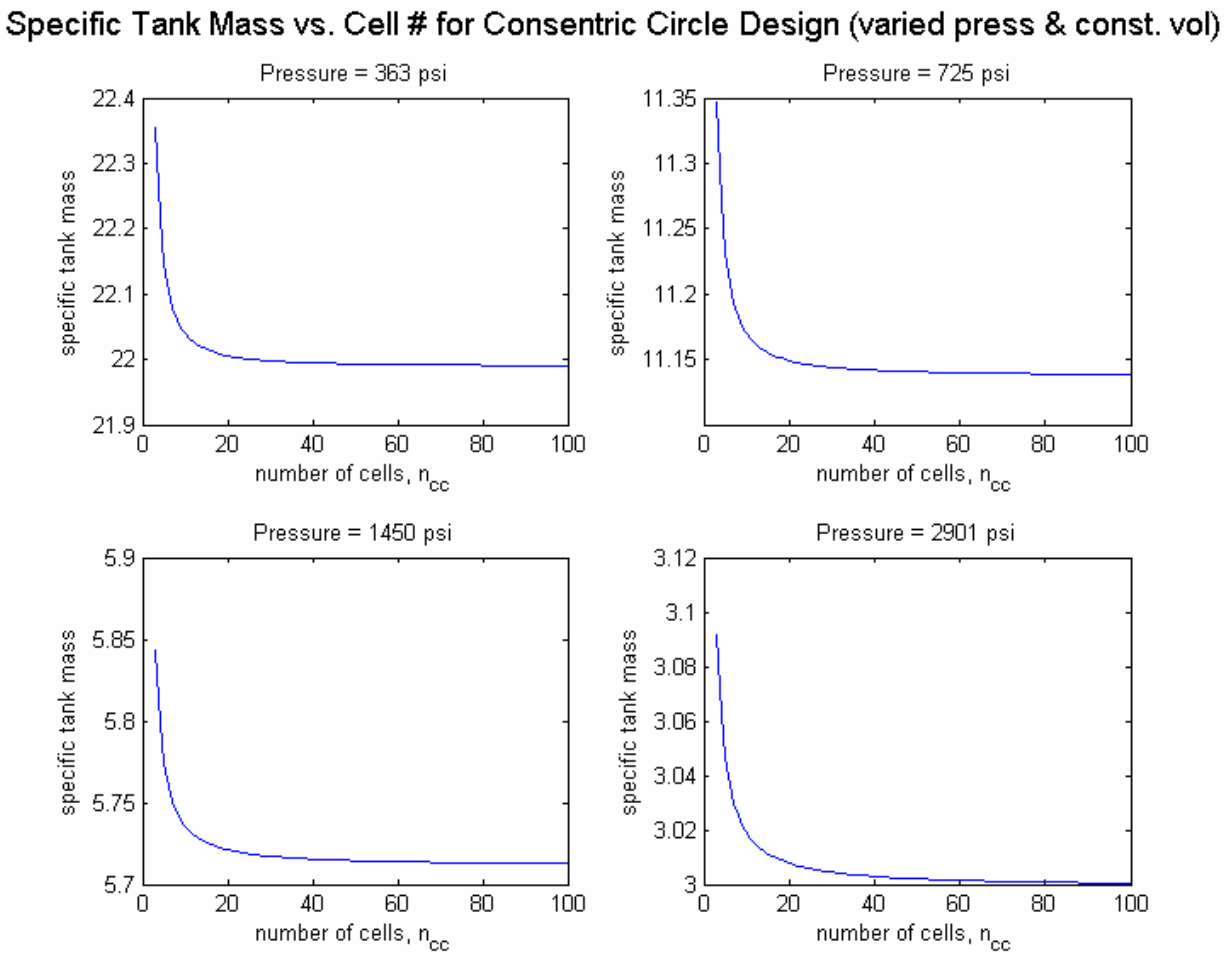

Figure A-7: Specific Tank Mass versus Cell # and Height for Concentric Tori Design (varied pressure and constant volume)

A.1.3 Wedge Vessel

This tank structure consists of a nearly cylindrical vessel with triangular wedge sections. Each wedge shaped cell is formed by 3 semi-cylindrical edges (one of which is curved along the tank edge) joined at three corners with 3 spherical arcs closed by 2 flat triangular plates on the top and bottom of the cell. The stresses and deformations in the cells can be determined by considering the entire complicated shell as a combination of simple elements (cylinder, sphere, and triangular flat plate) using membrane solution methods. This analysis is almost identical to the more accurate but complicated bending theory methods with the exception of a narrow strip on the shell surfaces adjacent to the boundary.[3]

To determine cell and structural volumes, we first define key parameters of the figure which will determine all other geometric values. Each cell fits inside and has edges flush to a wedge of a short cylinder with a vertex angle of 2α and a vertex edge length R. The angle α is determined by the number of cells desired C such that:

$$\alpha = \frac{\pi}{C}$$

The dimensions of an individual cell like that illustrated to the

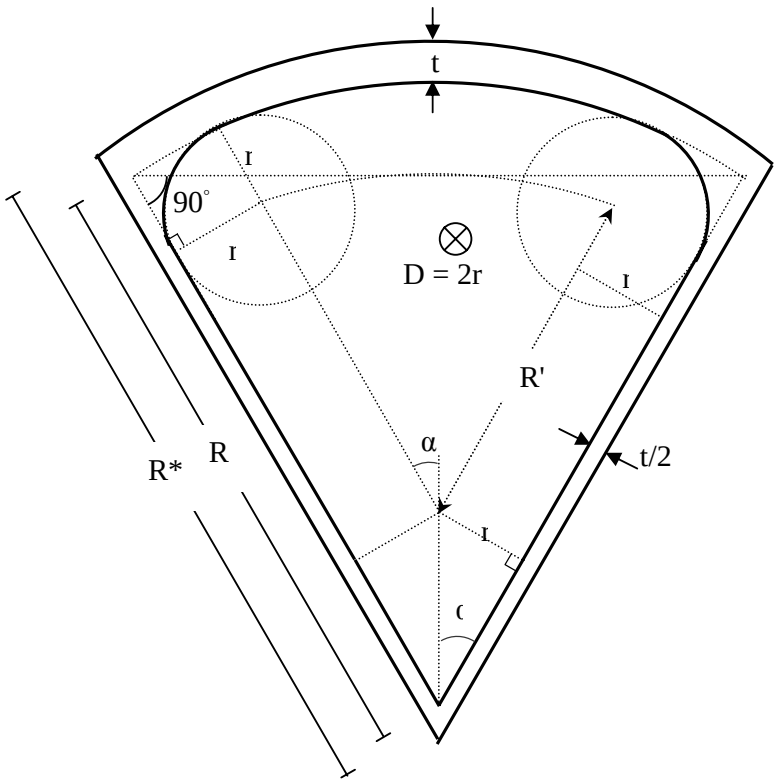

Figure A-8: Single wedge vessel cell

right can be found with basic geometry and are as follows:

$$\begin{aligned}
R &= R' + r\left(1+\cot\alpha\right) \\
R^* &= R + t + \frac{t}{2\sin\alpha} = R + \frac{t}{2}\left(2+\csc\alpha\right) \\
V_{cell} &\approx \frac{1}{2}\left(\pi r^2\right)(\text{perimeter}) = \left(A_{inner-periemeter}\right)D \\
&= \frac{1}{2}\left(\pi r^2\right)\left[\left(2+2\alpha\right)R'\right] + \left(\frac{\alpha}{\pi}\pi R'^2\right)(2r) \\
&= \pi\left(1+\alpha\right)r^2R' + 2\alpha r R'^2 = \left(\pi\left(1+\alpha\right)r + 2\alpha R'\right)rR' \\
SV_{cell} &= 2\left(r+t\right)\alpha R^{*2} - V_{cell} = 2\alpha r\left(R^{*2} - R'^2\right) + \pi\left(1+\alpha\right)r^2R' \\
V &= CV_{cell} = \frac{\pi}{\alpha}V_{cell} = \left[\frac{\left(1+\alpha\right)\pi^2}{\alpha}R'\right]r^2 + \left[2\pi R'^2\right]r = ar^2 + br \\
SV &= C\cdot SV_{cell} = \frac{\pi}{\alpha}SV_{cell}
\end{aligned}$$

The wall thickness should be determined by the highest stress component such that:

$$t = max\left[t_{triangular-plate}, t_{spherical-section}, t_{cylindrical-section}\right]$$

The thickness associated with the spherical and cylindrical sections are as follows:

$$\begin{aligned}
t_{spherical-section} &= FOS\frac{qr}{2\sigma_f} \\
t_{cylindrical-section} &= FOS\frac{qr}{\sigma_f}
\end{aligned}$$

If we treat the plate section as a plate clamped on the two vertex sides with infinite radius, the maximum stress will be along the edges of the plate at the largest radius giving a necessary plate thickness of:

$$t_{triangular-plate} = R'\cdot FOS\sqrt{\frac{3q}{2\sigma_f}\frac{\sin^2\theta}{1+2\cos^2\theta}}$$

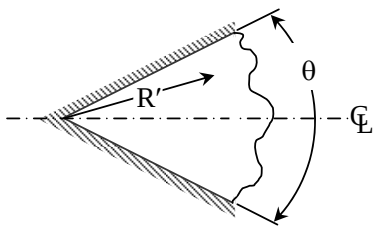

Figure A-9: Plate model

Given these equations, we see that the cell wall

thickness will be determined by either $t_{cylindrical-section}$ or $t_{triangular-plate}$. The ratio of these two quantities yields:

$$\frac{t_{cylindrical-section}}{t_{triangular-plate}} = \frac{r}{R'}\sqrt{\frac{q}{\sigma_f}}\frac{1}{\sqrt{\beta}}$$

where $\beta = \frac{3}{2}\frac{\sin^2\theta}{1+2\cos^2\theta}$.

Given the limitation that this vessel should be short and wide, we know $\frac{r}{R'} < 1$. We predict that the fracture strength of silicon will be something on the order of $\sigma_f \approx 1$ GPa and the internal pressure of the vessel will be not much larger than industry pressures which have a maximum of about $q_{design} \approx 10,000\text{psig} \approx 70$ MPa. Thus, we expect $\frac{1}{4} < \sqrt{\frac{q}{\sigma_f}} < 1$. We can see the rlation between the last factor, $1/\sqrt{\beta}$, and cell vertex angle, θ, in the plot to the right.

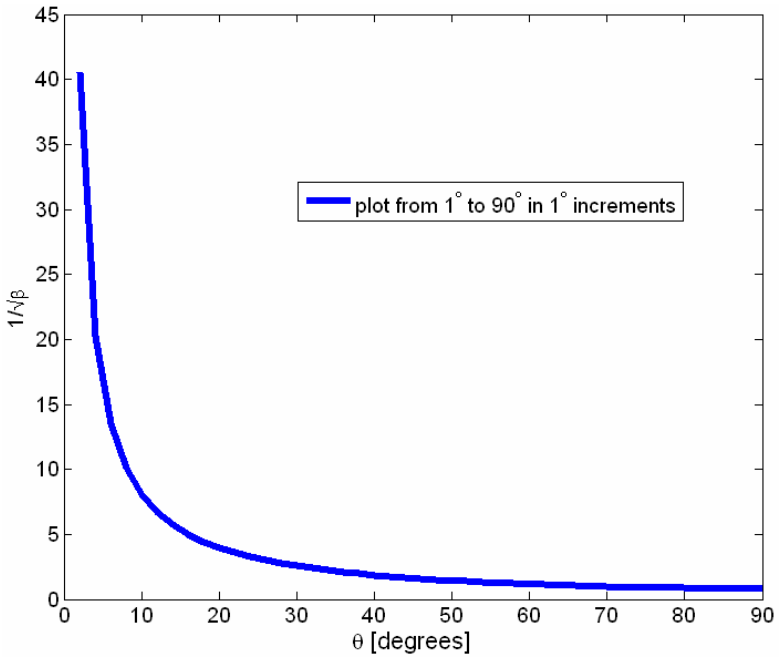

Figure A-10: $1/\sqrt{\beta}$ factor for various values of θ

For these conditions and small values of $\frac{r}{R'}$ $\left(< \frac{1}{10}\right)$, we expect the plate thickness to be the limiting thickness for the vessel. In fact, for the values of $\frac{r}{R'}$ predicted for a vessel omitting considerations for stress in the plate sections of the vessel, as are shown in the following plots, we see that $\frac{r}{R'} < 10$ is still predicted implying a plate thicknesses thicker than those necessary for the cylindrical sections.

The following plots model a wedge cell using a wall thickness determined by

$t_{cylindrical-section}$ varying pressure, volume and geometry to see their effect on mass ratio.

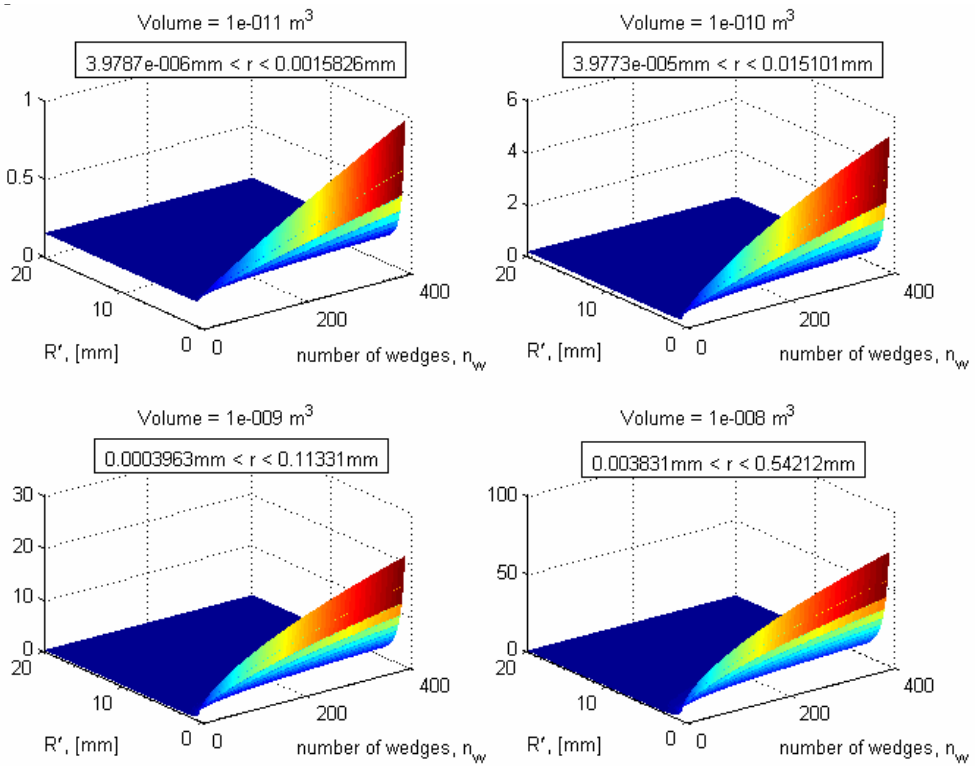

Figure A-11: Specific Tank Mass versus Cell # and Height for Wedge Design w/o Plate Section Model (varied volume and constant pressure)

These plots imply that vessel mass ratio decreases with decreasing volume, increasing pressure, and reduced cell numbers.

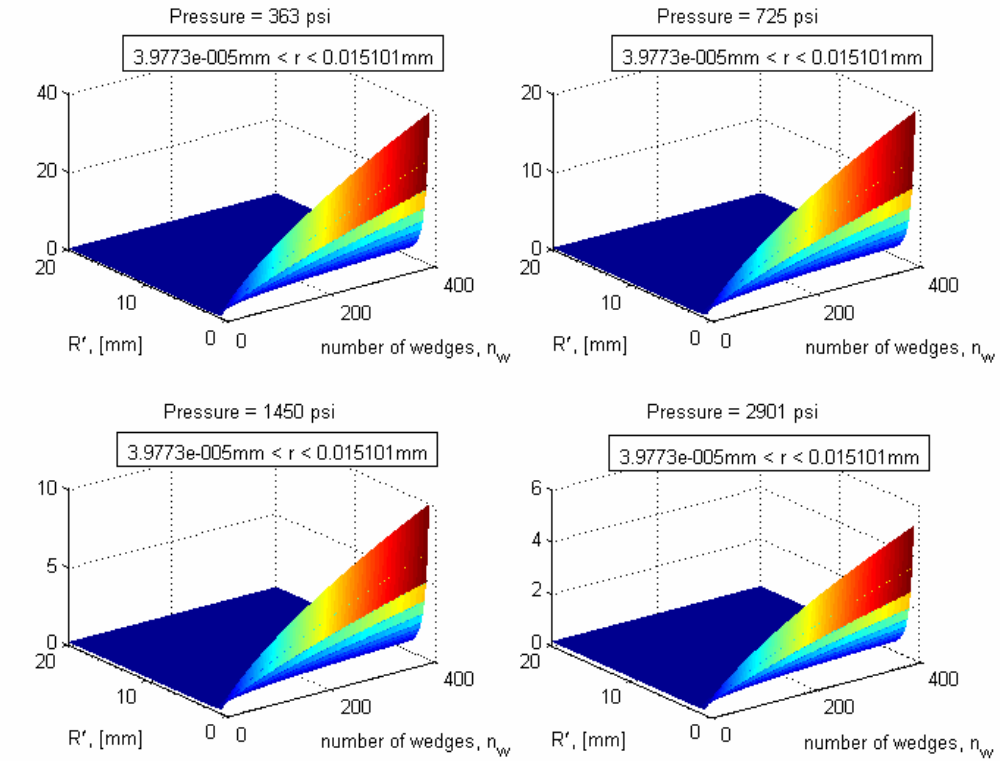

Figure A-12: Specific Tank Mass versus Cell # and Height for Wedge Design w/o Plate Section Model (varied pressure and constant volume)

A.1.4 Pancake Vessel

This tank structure consists of the outer circular part of a toroidal vessel with two flat circular plates capping the top and bottom. Again, the stresses and deformations in the vessel can be determined by considering the shell as a combination of simple elements using membrane solution methods. This analysis is almost identical to the more accurate but complicated bending theory methods with the exception of a narrow strip on the shell surfaces adjacent to the boundary.[3]

The wall thickness of the shell will be determined by the wall thickness required to withstand the maximum stress in the vessel. The maximum stress in the vessel will be equal to:

$$\sigma_{design} = max\left(\sigma_{toroial-section}, \sigma_{plate-section}\right)$$

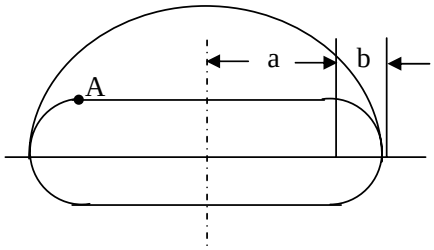

Figure A-13: Cross-section view of pancake vessel taken through the wafer plane

The maximum stress for a torus is:

$$\sigma_{toroial-section} = \frac{qb}{t}$$

and will be located at a point A on the toroidal section.

The solution for maximum stress in a circular plate can be found from solving the generalized displacement equation for a circular plate for specified boundary conditions:

$$\frac{D}{q}w = \frac{r^4}{64} + \frac{c_1 r^2}{4}\left(\ln r - 1\right) + \frac{c_2 r^2}{4} + c_3 \ln r + c_4$$

where D is the bending rigidity of the plate such that $D = \frac{Et^3}{12(1-\nu^2)}$, q is a pressure uniformly distributed over the plate, w is the plate deflection, r is the radius measured from a coordinate system in the center of the plate, and $c_{1,2,3,4}$ are constants of

integration. The equations for principle moments for a circular plate are:

$$\begin{aligned} M_r &= -D\left[\frac{d^2w}{dr} + \frac{\nu}{r}\frac{dw}{dr}\right] \\ M_\theta &= -D\left[\frac{1}{r}\frac{dw}{dr} + \nu\frac{d^2w}{dr^2}\right] \end{aligned}$$

For a clamped plate the boundary conditions will be $w = 0$ and $\frac{dw}{dr} = 0$ at $r = a$. For this case $c_1 = c_3 = 0$ to avoid infinite plate deflection at the plate center. To satisfy the given boundary conditions we find $c_2 = -a^2/8$ and $c_4 = a^4/64$. thus, the deflection must be:

$$w = \frac{q}{64D}\left(r^2 + a^2\right)^2$$

For the clamped plate, the deflection equation gives the following moments:

$$\begin{aligned} M_r &= \frac{q}{16}\left[(1+\nu)\,a^2 - (3+\nu)\,r^2\right] \\ M_\theta &= \frac{q}{16}\left[(1+\nu)\,a^2 - (1+3\nu)\,r^2\right] \end{aligned}$$

This gives a maximum stress of:

$$\sigma_{max} = \left(\frac{zM}{t^3/12}\right)_{max} = -\frac{3}{4}\frac{qa^2}{t^2}$$

at the edge of the plate

For a simply supported plate the boundary conditions will be $w = 0$ and $M_r = 0$ fat $r = a$. We see in this case $c_1 = c_3 = 0$ to avoid infinite plate deflection at the plate center. Thus the deflection will be:

$$\frac{D}{q}w = \frac{r^4}{64} + \frac{c_2 r^2}{4} + c_4$$

To satisfy the given boundary conditions we find:

$$M_r\,(r=a) = -D\left[\left.\frac{d^2w}{dr^2}\right|_{r=a} + \frac{\nu}{a}\left.\frac{dw}{dr}\right|_{r=a}\right] = 0$$

$$\text{which} \quad \Rightarrow \quad \left.\frac{d^2w}{dr}\right|_{r=a} = -\frac{\nu}{a}\left.\frac{dw}{dr}\right|_{r=a}$$
$$\text{which} \quad \Rightarrow \quad c_2 = -\frac{a^2}{8}\frac{(3+\nu)}{(1+\nu)}$$

Thus,

$$\begin{aligned}\frac{a^4}{64} - \frac{a^2}{8}\frac{(3+\nu)}{(1+\nu)}\frac{a^2}{4} + c_4 &= 0 \\ \text{which } \Rightarrow c_4 &= \frac{a^4}{64}\frac{(5+\nu)}{(1+\nu)}\end{aligned}$$

Thus, the deflection must be:

$$w = \frac{q}{64D}\left[r^4 - 2a^2r^2\frac{(3+\nu)}{(1+\nu)} + a^4\frac{(5+\nu)}{(1+\nu)}\right]$$

For the simply supported plate deflection equation this gives moments:

$$\begin{aligned}M_r &= -D\left[\frac{d^2w}{dr^2} + \frac{\nu}{r}\frac{dw}{dr}\right] \\ &= -\frac{q}{16}\left[\left(3r^2 - a^2\frac{3+\nu}{1+\nu}\right) + \frac{\nu}{r}\left(r^3 - a^2r\frac{3+\nu}{1+\nu}\right)\right] \\ &= \frac{q\,(3+\nu)}{16}\left[a^2 - r^2\right] \\ M_\theta &= -D\left[\frac{1}{r}\frac{dw}{dr} + \nu\frac{d^2w}{dr^2}\right] \\ &= -\frac{q}{16}\left[\frac{1}{r}\left(r^3 - a^2r\frac{3+\nu}{1+\nu}\right) + \nu\left(3r^2 - a^2\frac{3+\nu}{1+\nu}\right)\right] \\ &= \frac{q}{16}\left[a^2\,(3+\nu) - r^2\,(1+3\nu)\right]\end{aligned}$$

This gives a maximum stress of:

$$\sigma_{max} = \left(\frac{zM}{t^3/12}\right) = -\frac{3}{8}\frac{qa^2\,(3+\nu)}{t^2}$$

at the center of the plate.

It is believed that the actual behavior of the plate section of the pancake vessel will be between these two boundary conditions. For modelling purposes, we take the worse

case scenario (highest maximum stress scenario) where the plate is simply supported at the edges and has a maximum stress in the center of the plate of:

$$\sigma_{plate-section} = \frac{3}{8}\frac{qa^2\left(3+\nu\right)}{t^2}$$

Thus,the thickness of the vessel will be determined as the maximum stress in the vessel which is determined by:

$$\begin{aligned} t &= max\left(FOS\frac{qb}{\sigma_f}, \left[\frac{3}{8}a^2 FOS\frac{q\left(3+\nu\right)}{\sigma_f}\right]^{1/2}\right) \\ &= max\left(FOS\frac{qb}{\sigma_f}, \left[\frac{3}{8}b^2 FOS\frac{q\left(3+\nu\right)}{\sigma_f}\right]^{1/2}\frac{a}{b}\right) \end{aligned}$$

The internal volume will be;

$$V = \left(\frac{\pi b^2}{2}\right)\left(2\pi a\right) + 2b\left(\pi a^2\right) = \pi b^3\frac{a}{b}\left[\pi + 2\frac{a}{b}\right]$$

The structural volume will be:

$$SV = \left(\pi b\right)t\left(2\pi a\right) + 2\left(\pi a^2\right)t = 2\pi\frac{a}{b}b^2 t\left[\pi + \frac{a}{b}\right]$$

Given a starting volume, we can determine the vessel dimensions by first deciding what the ratio $\frac{a}{b}$ should be. We not that $\frac{SV}{V} \propto \frac{\pi+\frac{a}{b}}{\pi+2\frac{a}{b}}$ which decreases with increasing $\frac{a}{b}$. Se we optimize by finding $\frac{a}{b}$ such that the toroidal section and the plate section have equal thickness:

$$\begin{aligned} FOS\frac{qb}{\sigma_f} &= \left[\frac{3}{8}b^2 FOS\frac{q\left(3+\nu\right)}{\sigma_y}\right]^{1/2}\frac{a}{b} \\ \Rightarrow \frac{a}{b} &= 2\left[FOS\frac{2q}{3\sigma_f\left(3+\nu\right)}\right]^{1/2} \end{aligned}$$

For silicon with $\nu = 0.17$, $FOS = 1.5$, $q \approx 7$ksi, and $\sigma_f = 600$MPa this equation implies $\left(\frac{a}{b}\right) = 0.32$. So the optimal, such that $\frac{a}{b}$ must be an integer, is a sphere, $\frac{a}{b} = 0$. Because we know this already, we vary $\frac{a}{b}$ greater than 1 for comparison purposes.

When $\frac{a}{b}$ is chosen, we can find dimensions of the vessel given a volume by:

$$\begin{aligned} b &= \left[\frac{V}{\frac{a}{b}\pi\left[\pi + 2\frac{a}{b}\right]}\right]^{1/3} \\ a &= b\frac{a}{b} \\ t &= max\left(FOS\frac{qb}{2\sigma_f}\frac{2\frac{a}{b}-1}{\frac{a}{b}-1}, \left[\frac{3}{8}b^2 FOS\frac{q\left(3+\nu\right)}{\sigma_f}\right]^{1/2}\frac{a}{b}\right) \end{aligned}$$

The Effect of Plate Section Tension on Maximum Stress

As the internal pressure of the vessel is increased, tension will appear in the circular plate section equal to the stress at the plate/toroid section boundary. This stress we know is equal to;

$$\sigma_r = \sigma_A = \frac{qb}{t}$$

This is equivalent to a normal force per unit length applied tension of:

$$N = t\sigma_r = qb$$

The approximate solution for a plate with applied tension N and uniform applied lateral load q is given by Timoshenko and Woinowsky-Krieger as the following:[40]

$$w = \frac{w_q}{1+\alpha}$$

where w_q is the displacement solutioni for a uniform load q alone and

$$\alpha = \frac{Na^2}{4.20D} \text{ , for a simply supported plate}$$

and

$$\alpha = \frac{Na^2}{14.68D} \text{ , for a clamped plate}$$

The maximum moments due to curvatures on the simply supported plate occurring at the plate center will be:

$$\begin{aligned}(M_r)_{max} &= \frac{1}{1+1.0480\alpha}\left(M_r\left(r=0\right)\right)_q = \frac{D}{D+0.2495qba^2}\frac{q\left(3+\nu\right)a^2}{16}\\ (M_\theta)_{max} &= \frac{1}{1+1.0480\alpha}\left(M_\theta\left(r=0\right)\right)_q = \frac{D}{D+0.2495qba^2}\frac{q\left(3+\nu\right)a^2}{16}\end{aligned}$$

Where $\left(M_r\right)_q$ and $\left(M_\theta\right)_q$ are the moments due only to the uniform load q. This gives the following maximum stress:

$$\begin{aligned}\sigma_{max} &= \left(\frac{zM}{t^3/12}\right)_{max} = \frac{3q\left(3+\nu\right)a^2}{8t^2}\frac{D}{D+0.2495qba^2}\\ &= \frac{3q\left(3+\nu\right)a^2}{8}\frac{Et}{Et^3+2.9940\left(1-\nu^2\right)qba^2}\end{aligned}$$

Given material fracture stress and factor of safety we can solve the following polynomial for material thickness:

$$t_{plate}^3 - \frac{3q\left(3+\nu\right)a^2}{8\sigma_f}FOS\cdot t_{plate} + 2.9940\frac{\left(1-\nu^2\right)qba^2}{E} = 0$$

The maximum moments due to curvatures on the clamped plate occurring at the plate edge will be:

$$(M_r)_{max} = \frac{1}{1+0.527\alpha}\left(M_r\left(r=a\right)\right)_q = \frac{D}{D+0.03590qba^2}\frac{qa^2}{8}$$

This gives the following maximum stress:

$$\begin{aligned}\sigma_{max} &= \left(\frac{zM}{t^3/12}\right)_{max} = \frac{3qa^2}{4t^2}\frac{D}{D+0.03590qba^2}\\ &= \frac{3qa^2}{4}\frac{Et}{Et^3+0.03590\cdot 12\left(1-\nu^2\right)qba^2}\end{aligned}$$

Given material fractures stress and factor-of-safety, we can solve the following poly-

nomial for material thickness:

$$t_{plate}^3 - \frac{3qa^2}{4\sigma_f} FOS \cdot t_{plate} + \frac{0.4308\,(1-\nu^2)\,qba^2}{E} = 0$$

For the simply supported case with the maximum stress at the center of the plate section, the thickness of the vessel will be determined as the maximum stress in the vessel which is determined by:

$$t = max\left(FOS\frac{qb}{\sigma_f}, t_{plate}\right)$$

The following plots show the variation in specific tank mass for various internal volumes with a constant internal pressure and various internal pressures with a constant internal volume.

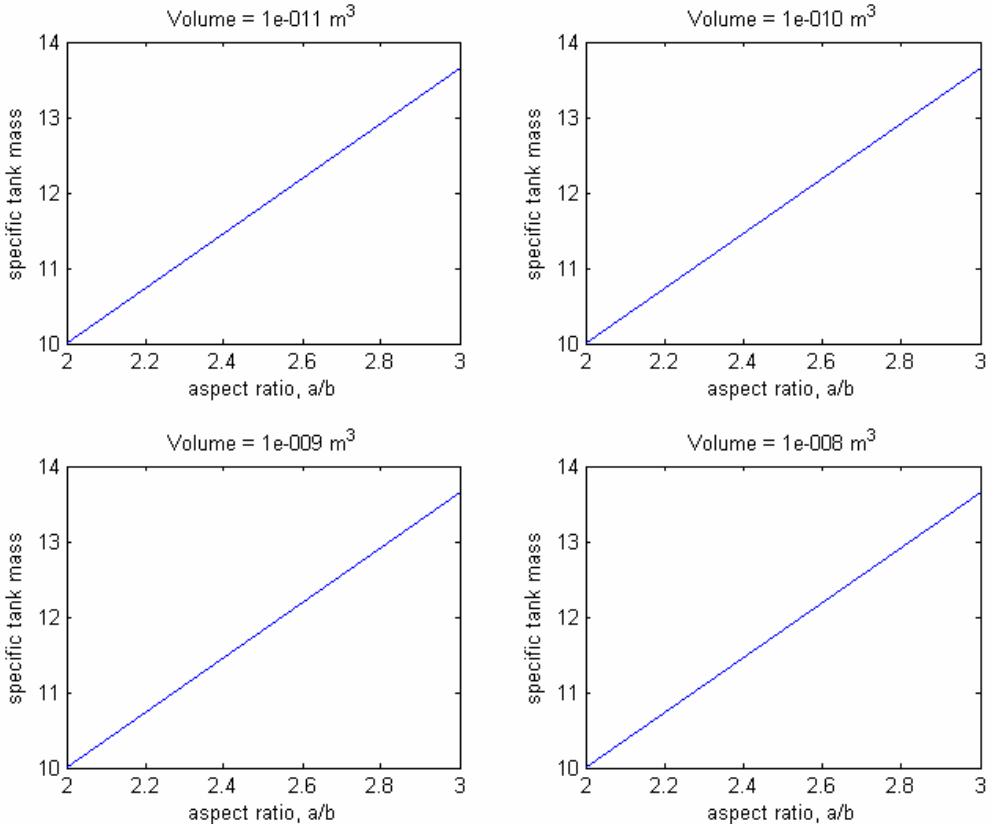

Figure A-14: Specific Tank Mass versus Cell # and Height for Pancake Design (varied volume and constant pressure)

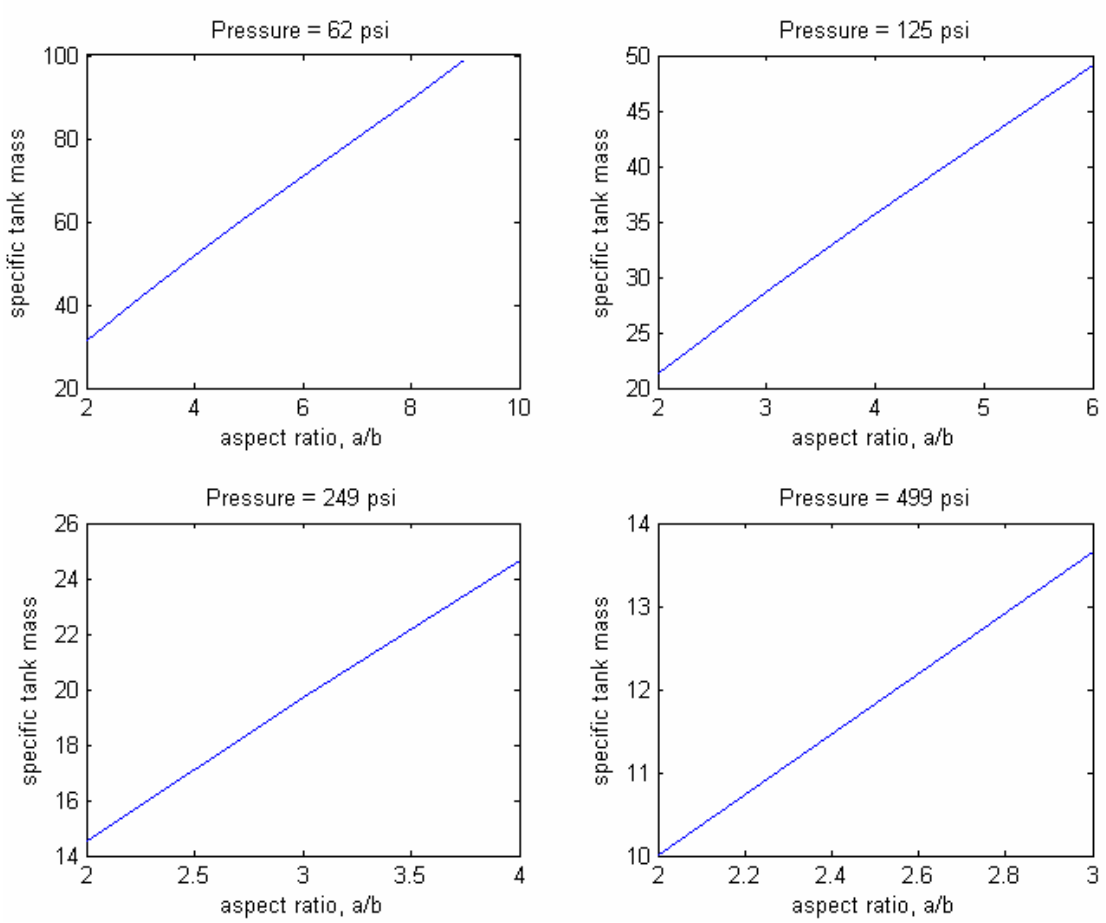

Figure A-15: Specific Tank Mass versus Cell # and Height for Pancake Design (varied pressure and constant volume)

We note that the specific structural mass does not seem to vary with variation in internal volume. The structural mass of the tank decreases with decreasing aspect ratio and increasing internal pressure.

A.1.5 Conventional Vessel Geometries

Cylinder

An ordinary cylinder with spherical caps like the cells of the honeycomb design will have internal volume,

$$V = \frac{4}{3}\pi R_x^3 + \pi H_c R_c^2$$

and wall thickness,

$$T_c = FOS\frac{qR_c}{\sigma_f}$$

We arbitrarily consider $R_c = H_c$ which implies $V = \frac{7}{3}\pi R_c^3$ which can be solved from R_c which gives H_c and can thus find the structural volume as:

$$\begin{aligned} SV &= \left[\frac{4}{3}\pi\left(R_c + T_c\right)^3 + \pi\left(R_c + T_c\right)^2 H_c\right] - V \\ &= \left[\frac{4}{3}\pi\left(R_c + \frac{FOS\cdot R_c}{\sigma_f}q\right)^3 + \pi\left(R_c + \frac{FOS\cdot R_c}{\sigma_f}q\right)^2 H_c\right] - V \\ &= \frac{4}{3}\pi\left(\frac{FOS}{\sigma_f}\right)^3 R_c^3 q^3 + \pi\left(\frac{FOS}{\sigma_f}\right)^2 R_c^2\left[4R_c + H_c\right]q^2 \\ &\quad + \left[4\pi\left(\frac{FOS}{\sigma_a}\right)R_c^3 + 2\pi\left(\frac{FOS}{\sigma_f}\right)R_c^2 H_c\right]q \end{aligned}$$

Thus, the specific volume will be:

$$\begin{aligned} \frac{SV}{V} &= \frac{4\pi R_c^3}{3V}\left(\frac{FOS}{\sigma_f}\right)^3 q^3 + \frac{\pi R_c^2\left[4R_c + H_c\right]}{V}\left(\frac{FOS}{\sigma_f}\right)^2 q^2 + \frac{\left[2R_c + H_c\right]2\pi R_c^2}{V}\left(\frac{FOS}{\sigma_f}\right)q \\ &= \frac{4\pi R_c^3}{3V}\left(\frac{FOS}{\sigma_f}\right)^3 q^3 + \frac{\left[\frac{8}{3}\pi R_c^3 + V\right]}{V}\left(\frac{FOS}{\sigma_f}\right)^2 q^2 + \frac{\left[\frac{4}{3}\pi R_c^3 + 2V\right]}{V}\left(\frac{FOS}{\sigma_f}\right)q \end{aligned}$$

Sphere

An ordinary sphere with the same volume as the honeycomb design will have a radius,

$$R_{sphere} = \left[\frac{V}{4/3\pi}\right]^{1/3}$$

and wall thickness,

$$T_{sphere} = FOS\frac{qR_{sphere}}{2\sigma_f}$$

Thus will have a structural volume,

$$\begin{aligned} SV &= \frac{4}{3}\pi\left(R_{sphere}+T_{sphere}\right)^3 - V \\ &= \frac{4}{3}\pi T_{sphere}^3 + 4\pi R_{sphere}T_{sphere}^2 + 4\pi R_{sphere}^2 T_{sphere} \\ &= \frac{4}{3}\pi R_{sphere}^3\left(\frac{FOS}{2\sigma_f}\right)^3 q^3 + 4\pi R_{sphere}^3\left(\frac{FOS}{2\sigma_f}\right)^2 q^2 + 4\pi R_{sphere}^3\left(\frac{FOS}{2\sigma_f}\right) q \end{aligned}$$

Thus, the specific volume will be:

$$\begin{aligned} \frac{SV}{V} &= \frac{\frac{4}{3}\pi R_{sphere}^3}{V}\left(\frac{FOS}{2\sigma_f}\right)^3 q^3 + \frac{4\pi R_{sphere}^3}{V}\left(\frac{FOS}{2\sigma_f}\right)^2 q^2 + \frac{4\pi R_{sphere}^3}{V}\left(\frac{FOS}{2\sigma_f}\right) q \\ &= \left(\frac{FOS}{2\sigma_f}\right)^3 q^3 + 3\left(\frac{FOS}{2\sigma_f}\right)^2 q^2 + 3\left(\frac{FOS}{2\sigma_f}\right) q \end{aligned}$$

Torus/Tube

A torus/tube with major radius to minor radius ratio $\frac{a}{b}$ with the same volume as the honeycomb structure will have minor radius,

$$b = \left[\frac{V}{2\pi^2\frac{a}{b}}\right]^{1/3}$$

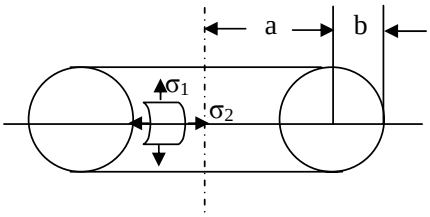

Figure A-16: Cross-section view of torus vessel

wall thickness,

$$T_{torus} = FOS\frac{qb}{2\sigma_f}\frac{2\frac{a}{b}-1}{\frac{a}{b}-1}$$

internal volume,

$$V = 2\pi^2\frac{a}{b}b^3$$

structural volume,

$$SV = 2\pi^2\frac{a}{b}b\left(b+T_{torus}\right)^2 - V$$

$$
\begin{aligned}
&= 2\pi^2 \frac{a}{b} b \left(b + T_{torus}\right)^2 - 2\pi^2 \frac{a}{b} b^3 \\
&= \left(2\pi^2 \frac{a}{b} b^3\right) \left(\frac{FOS \frac{a}{b} - \frac{1}{2}}{\sigma_f \frac{a}{b} - 1}\right)^2 q^2 + 2 \left(2\pi^2 \frac{a}{b} b^3\right) \left(\frac{FOS \frac{a}{b} - \frac{1}{2}}{\sigma_f \frac{a}{b} - 1}\right) q
\end{aligned}
$$

Thus, the specific volume will be:

$$
\begin{aligned}
\frac{SV}{V} &= \frac{\left(2\pi^2 \frac{a}{b} b^3\right)}{V} \left(\frac{FOS \frac{a}{b} - \frac{1}{2}}{\sigma_f \frac{a}{b} - 1}\right)^2 q^2 + 2 \frac{\left(2\pi^2 \frac{a}{b} b^3\right)}{V} \left(\frac{FOS \frac{a}{b} - \frac{1}{2}}{\sigma_f \frac{a}{b} - 1}\right) q \\
&= \left(\frac{FOS \frac{a}{b} - \frac{1}{2}}{\sigma_f \frac{a}{b} - 1}\right)^2 q^2 + 2 \left(\frac{FOS \frac{a}{b} - \frac{1}{2}}{\sigma_f \frac{a}{b} - 1}\right) q
\end{aligned}
$$

Appendix B

Fabrication Details and Etch Recipes for Radiused Hubbed Flexure Specimen

This appendix details the fabrication steps for the RHFS and the etch recipes.

B.1 RHFS Fabrication Process Steps

The purpose of this process is to fabricate a test structure for mechanical bi-axial flexure testing.

Start with DSP 650 um 6" wafer

1. RCA clean [rca-ICL]
2. 0.5 μm wet thermal oxidation growth for 1.5 hours at 1000°C [ICL tube 5C]
3. Photo Resist Cycle
   (a) HMDS [HMDS]
   (b) Spin thin resist on back [coater]
   (c) Pre-bake 30 min [prebakeovn]
   (d) Expose back [EV]

(e) Develop mask 2 [photo-wet]

(f) Post-bake [postbake]

4. RIE etch oxide from back [ICL-AME5000]

5. Ash [asher-TRL]

6. DRIE 1 μm back [sts2]

7. Photo Resist Cycle

   (a) HMDS [HMDS]

   (b) Spin thin resist on front [coater]

   (c) Pre-bake 30 min [prebakeovn]

   (d) Align and Expose front [EV]

   (e) Develop mask 2 [photo-wet]

   (f) Post-bake [postbake]

8. RIE etch oxide from front [ICL-AME5000]

9. Ash [asher-TRL]

10. Photo Resist Cycle

    (a) HMDS [HMDS]

    (b) Spin thick resist on front [coater]

    (c) Pre-bake 10 min [prebakeovn]

    (d) Spin thick resist on front [coater]

    (e) Pre-bake 10 min [prebakeovn]

    (f) Spin 2nd layer of thick resist on front [coater]

    (g) Pre-bake 50 min [prebakeovn]

    (h) Align and Expose front [EV]

(i) Develop mask 1 [photo-wet]

(j) Post-bake [postbake]

11. RIE etch oxide from front [ICL-AME5000]

12. DRIE 500μm from front [sts2]

13. BOE oxide [oxEtch-BOE]

14. 500 $\mathring{A}$ wet thermal oxidation growth at 900°C to smooth [TRLtube A2]

15. BOE thermal oxide [oxEtch-BOE]

16. Measure etch depth [wykoICL]

17. Diesaw [diesaw-ICL]

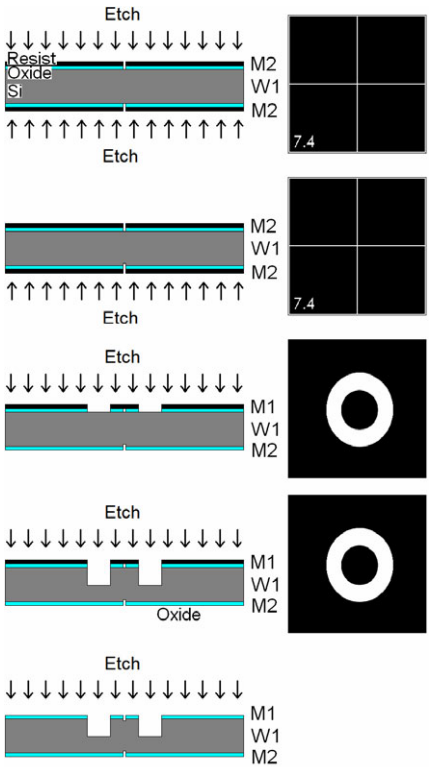

Figure B-1: Illustration of die cross-section and mask through process

B.2 Etch Recipes

This section gives the etch recipes used for DRIE and SF_6 smoothing below.

Table B.1: DRIE Recipe for RHFS

	Etch Step	**Passivation Step**
Time [sec]	15	11
Planten Generator Power [Watts]	120	60
Coil Generator Power [Watts]	750	600
SF_6 Flow [sccm]	105	0
C_4F_8 Flow [sccm]	0	40
APC Angle [% of 90°]	72.22	
Overrun	0.5	0

Table B.2: SF_6 Smoothing Etch Recipe for RHFS

	Etch Step
Time [sec]	15
Planten Generator Power [Watts]	120
Coil Generator Power [Watts]	950
SF_6 Flow [sccm]	30
C_4F_8 Flow [sccm]	0
APC Angle [% of 90°]	75
Overrun	0

Appendix C

Error Analysis

C.1 RHFS Error Analysis

This section describes potential sources of error in the RHFS experiments along with estimates of error. Error sources are divided into two groups. The first group is error due to geometry variation from the fabrication. The second group in error due to the experimental setup.

C.1.1 Geometry Error

Effects of Etch Depth Variation

Due to etch variation across the silicon wafer and limitation of DRIE etch depth precision, we expect for the etch depth to vary for each RHFS. ABAQUS^{TM}was used to look at the effects of varied fillet radius variation on maximum stress in the RHFS. A table was made with with the maximum stress output from ABAQUS^{TM}for varied etch depth between $470\mu m$ and $570\mu m$ in increments of $10\mu m$. Figure C-1 shows the error from assuming a $500\mu m$ etch depth (on a $650\mu m$ thick wafer) when the actual etch depth is something between $470\mu m$ and $530\mu m$. This figure shows significant error, $> 10\%$, due to etch depth variations greater than $\pm 10\mu m$

Etch depth was measured to significantly reduce error from unknown etch depth variation in experimental data reduction. Etch depth was measured at the greatest

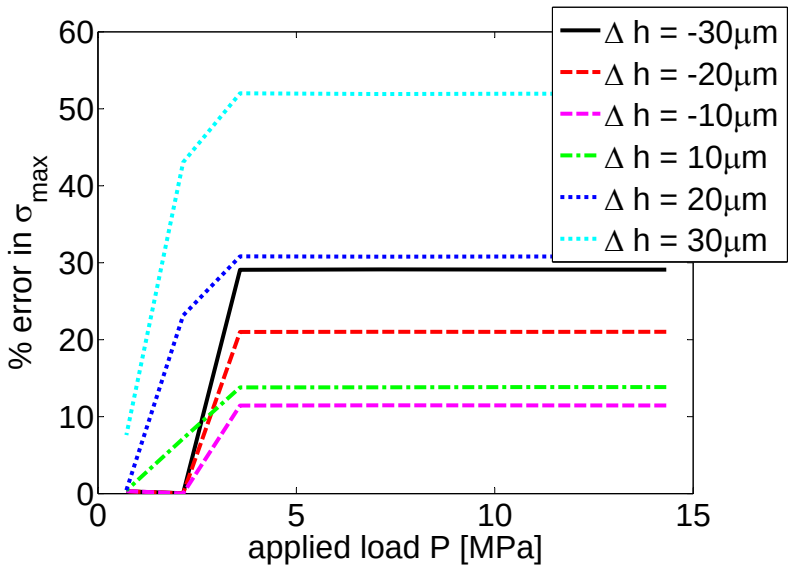

Figure C-1: Percent error in σ_{max} estimate for various etch depth variation $\pm$ 30 μm. (Maximum load considered is maximum loader load ability)

depth in the trench area furthest from the shallow-etched number label on each die. The etch depth variation was measured for every single sample on the first wafer set. The results of this measurement are illustrated in figure C-2. This figure shows that the DRIE etch depth gives a radially symmetric distribution of etch depths which is expected from the periodic 90° rotation of the wafer during etching. Based on this result, only a quarter of the etch depths are measured for the remaining wafers etched with RHFSs. The quarter of the etch depths that are measured are then used during data reduction assuming symmetry over the wafer. We expect error no greater than $\pm 10 \mu m$ after quarter-wafer etch depth measurements have been taken. From section C.1.2 and minor effects of 10% error in failure stress in the next subsection, we expect this to amount to no more than a 2% total error in the final data reduction of the Weibull parameters.

Effects of Fillet Radius Variation

Due to etch variation across the silicon wafer we expect for the fillet radius at the hub root to vary as well. Figures C-3 and C-4 show a radial sampling of fillet variation across the wafer for the 6" 650μm thick wafers with 1min SF_6 with and without

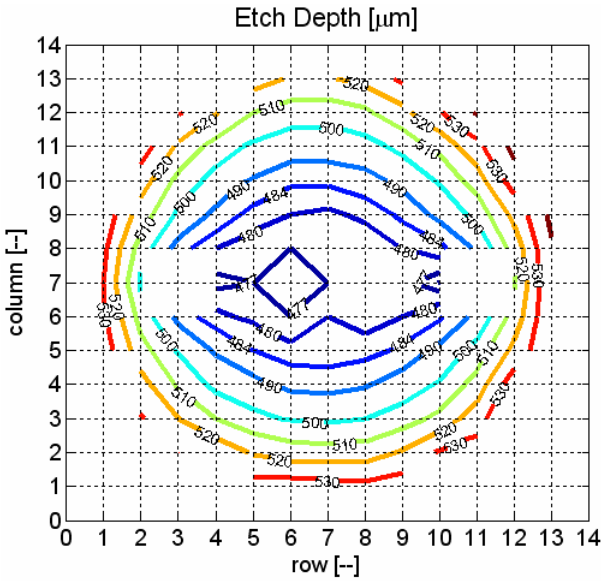

Figure C-2: Nearly radially symmetric etch depth across 6" 650μm thick wafer with 1min SF_6

oxide smoothing. These figures also show loosely estimated fits of the radius using Matlab^{TM}and the resultant estimations of the radius. You can see from the images that the circles used to estimate the fillet radius are not always well fit.

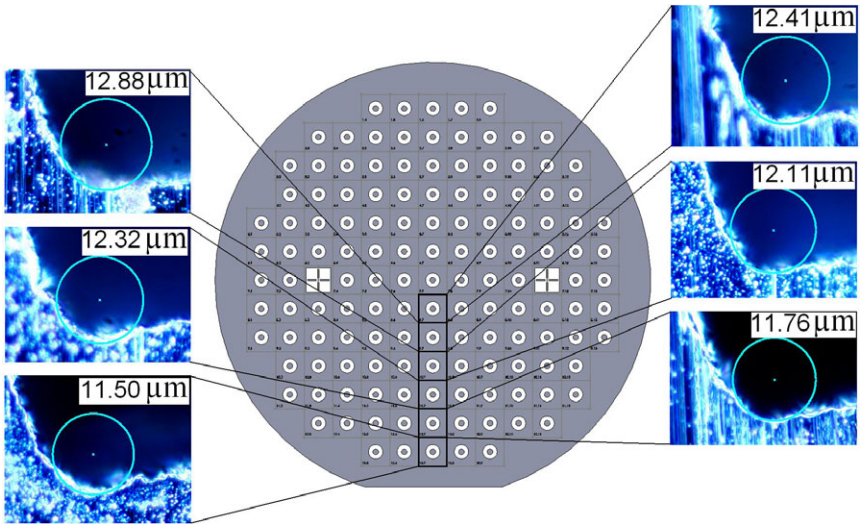

Figure C-3: Cross-section views of hub root fillets at various radial wafer locations and circular fits 6" 650μm thick wafer with 1min SF_6 and oxide smoothing

ABAQUS^{TM}was used to look at the effects of varied fillet radius variation on

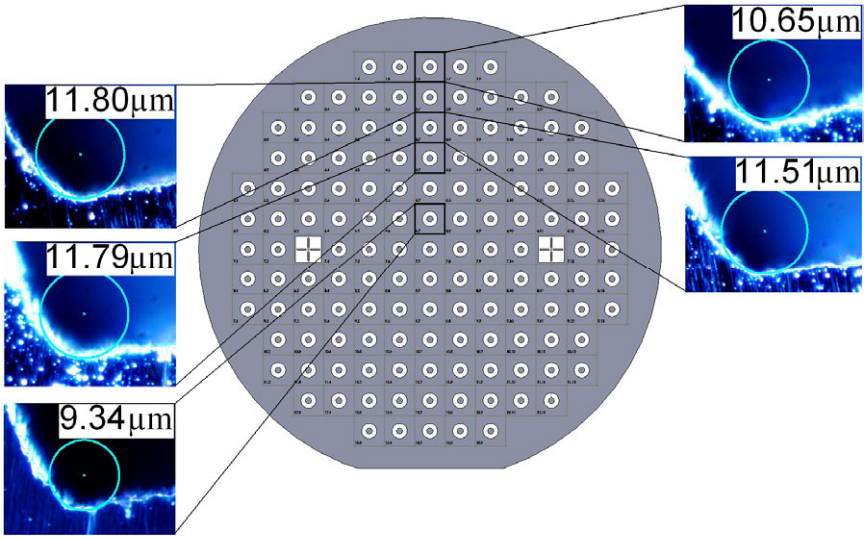

Figure C-4: Cross-section views of hub root fillets at various radial wafer locations and circular fits of 6" $650\mu m$ thick wafer with 1min SF_6 and oxide smoothing

maximum stress in the RHFS. A table was made with with the maximum stress output from ABAQUS^{TM}for fillet radius between $1\mu m$ and $12\mu m$ in increments of $1\mu m$ and varied applied load. Figure C-5 shows the error from assuming a $11\mu m$ fillet radius when the actual radius is something between $1\mu m$ and $12\mu m$.

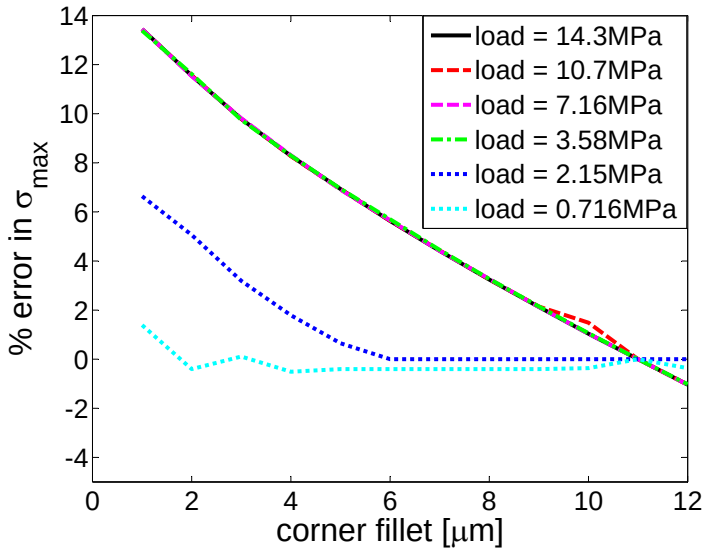

Figure C-5: Percent error in σ_{max} estimate by assuming fillet radius of 11 μm for actual fillets of 1-12 μm (Maximum load considered is maximum loader load ability)

Although the error in the σ_{max} estimate can be as high as 10%, it has little effect on the resultant Weibull parameters. Figure C-6 shows results of RHFS data tests for previous researchers, my work accounting for etch depth variation over the wafer, and my work accounting for maximum and minimum results from assuming a fillet radius variation between $1\mu m$ to $12\mu m$. The larger single symbols on the plot are for the etch depth variation results and the smaller pairs of symbols on the plot represent the $1\mu m$ to $12\mu m$ radius results. Because the pairs of symbols for $1\mu m$ to $12\mu m$ do not account for etch variation over the wafer, they are not always around the same area as the point that does. I cannot account for both varied fillet radius and etch depth at the same time without spending a significant amount of time on ABAQUS^{TM}. I think the results sufficiently show however how insensitive the Weibull parameters are to variations in radius about the average as well as to show that there is no significant improvement in strength and reliability for larger fillet radii.

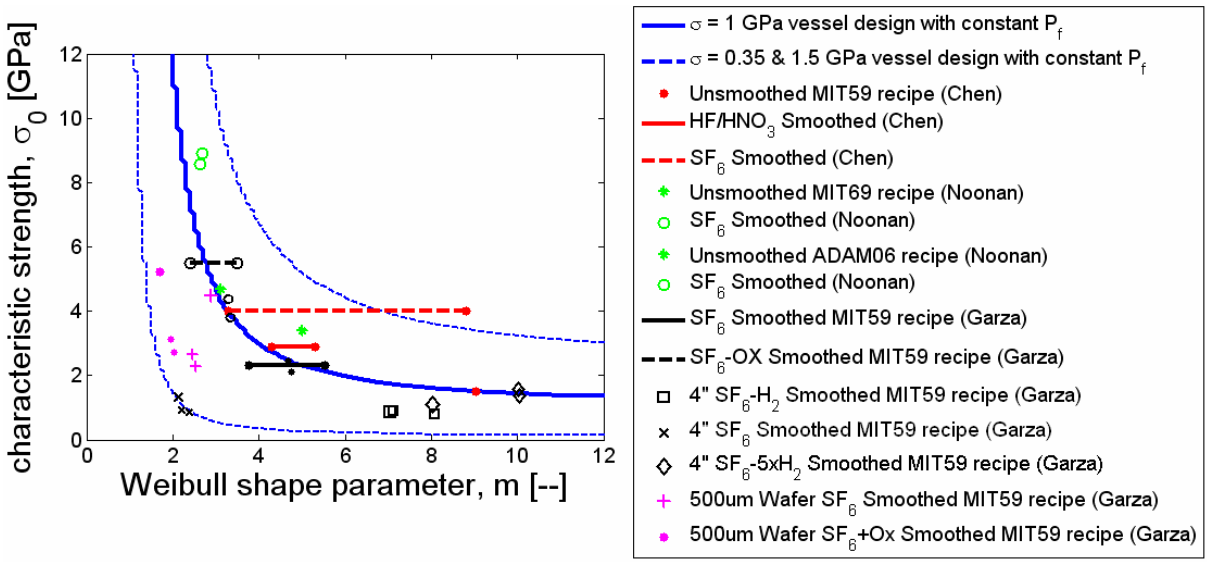

Figure C-6: Comparison of RHFS Data including variation due to varied fillet radius neglecting the effect of varied etch depth

Effects of Wafer Thickness Variation

A number of wafer thicknesses were used in this research. Possible error due to using a different wafer thickness was a concern and so ABAQUS^{TM}was used to make a table

of maximum stress in RHFS made from $450\mu m$ wafers for etch depths of $300\mu m$, $310\mu m$, $320\mu m$, and $330\mu m$ and varying applied loads. The error associated finding maximum stress from applied load assuming the $450\mu m$ wafer was actually a $650\mu m$ wafer for the Δh etch depths of $0\mu m$, $10\mu m$ wafer, $20\mu m$ wafer, and $30\mu m$ were found and are shown in figure C-7. From this figure we see the error is less than a percent which would have a negligible effect on the resultant Weibull parameters.

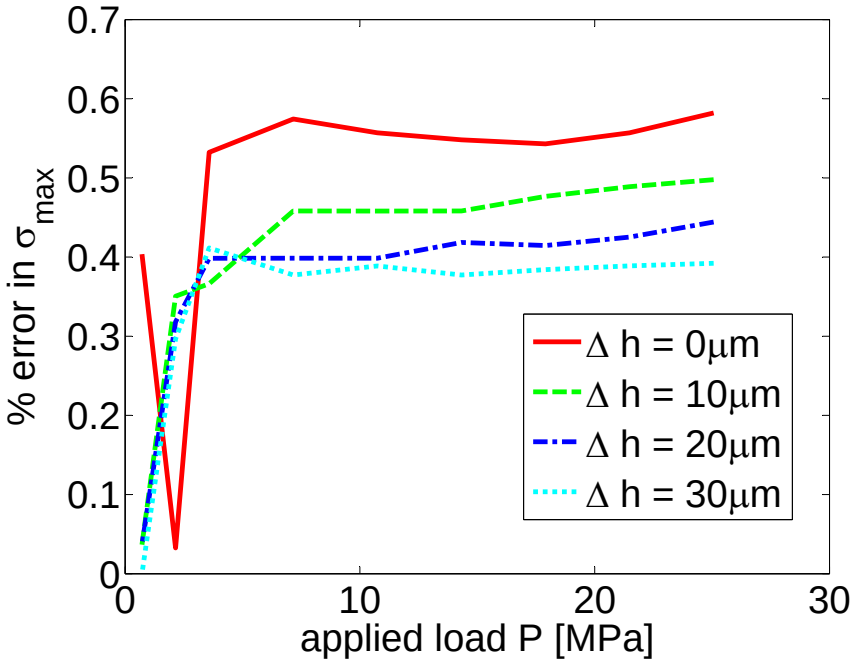

Figure C-7: Error in σ_{max} by using $650\mu m$ wafer data for a $450\mu m$ wafer

C.1.2 Experimental Error

Effects of Number Data Points with Virtual Experiment

This subsection describes how error in Weibull parameter estimations associated with the number of samples tested was determined. We use Matlab^{TM}to run a virtual experiment for a range of different sample set sizes. For each sample set size n, the virtual experiment is run 100 times and an average of the experimental error in Weibull parameter estimations is found.

We first define a Weibull distribution with characteristic strength σ_0 and Weibull

parameter m. Using these parameters, we randomly choose n strengths σ in this distribution with the probability defined by this Weibull distribution. We then use the method described in section 4.3.1 to find the Weibull parameters from the virtual experimental data $\sigma_{estimate}$ and $m_{estimate}$. The error in the estimation of the Weibull parameters from the virtual experimental data if found by comparting the parameters to those defined for the simulation σ_0 and m. Figure C-8 illustrates the average virtual error versus data set size. We can see that for sample sets with more than 50 data points, error is Weibull parameter estimation will be about 2%.

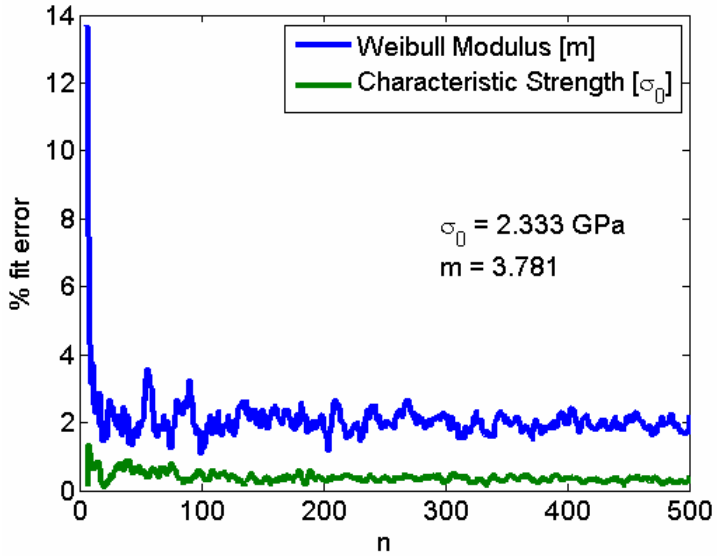

Figure C-8: Simulated Weibull experiments estimate of error for varied data points

Further Validation of Etch Depth and Fillet Error with Virtual Experiment

Using this virtual experiment, we looked at the effects of RHFS fillet radius variation of $11\pm2\mu m$ and an etch depth of $500\pm10\mu m$ (on a $650\mu m$ thick wafer) results in the same 2% for more than 50 data points.

Appendix D

Weibull Plots

D.1 RHFS Weibull Plots

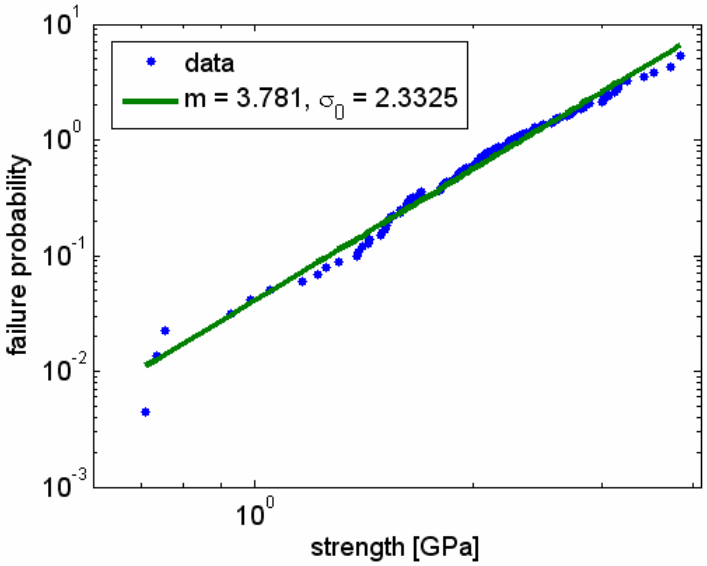

Figure D-1: Weibull Distribution for 6 inch 650μm Thick Wafer with 1 minute SF_6 Smoothing and 112 Data Points

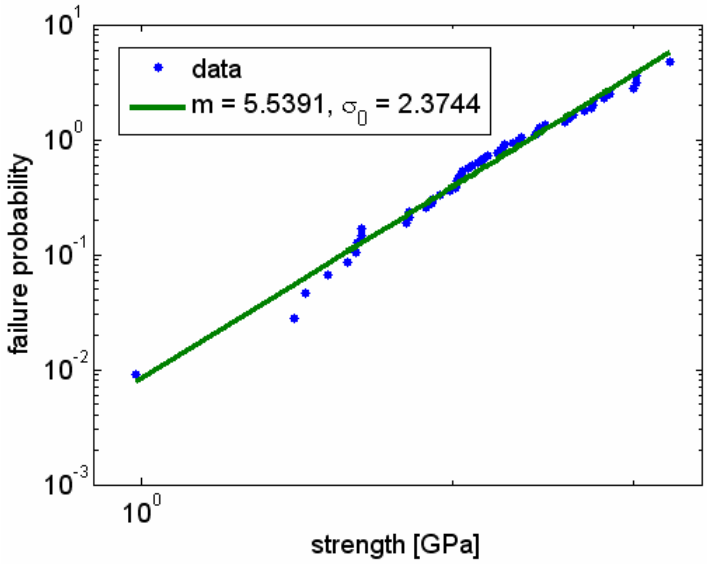

Figure D-2: Weibull Distribution resulting from data binning for 6 inch 650μm Thick Wafer with 1 minute SF_6 and 55 Data Points

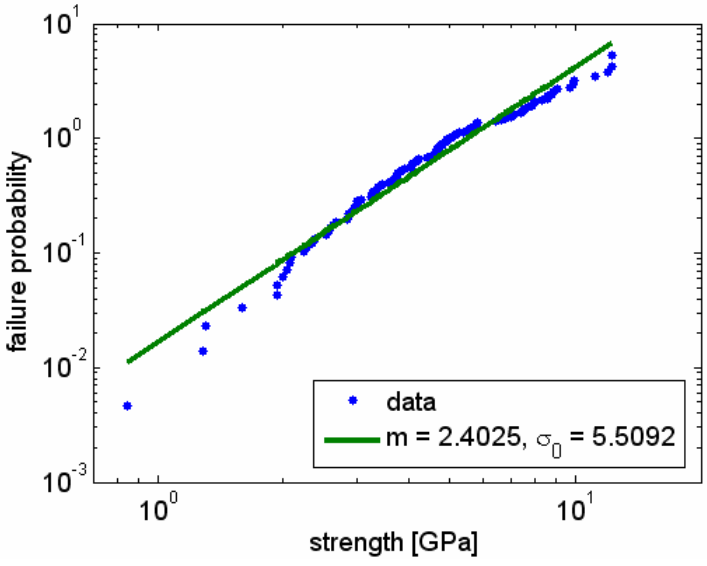

Figure D-3: Weibull Distribution for 6 inch 650μm Thick Wafer with 1 minute SF_6 and Oxidation and 108 Data Points

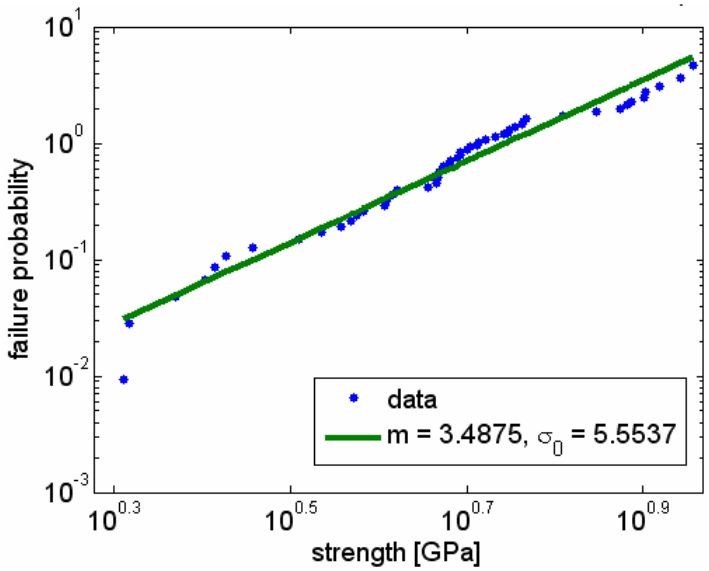

Figure D-4: Weibull Distribution resulting from data binning for 6 inch 650μm Thick Wafer with 1 minute SF_6 and Oxidation and 54 Data Points

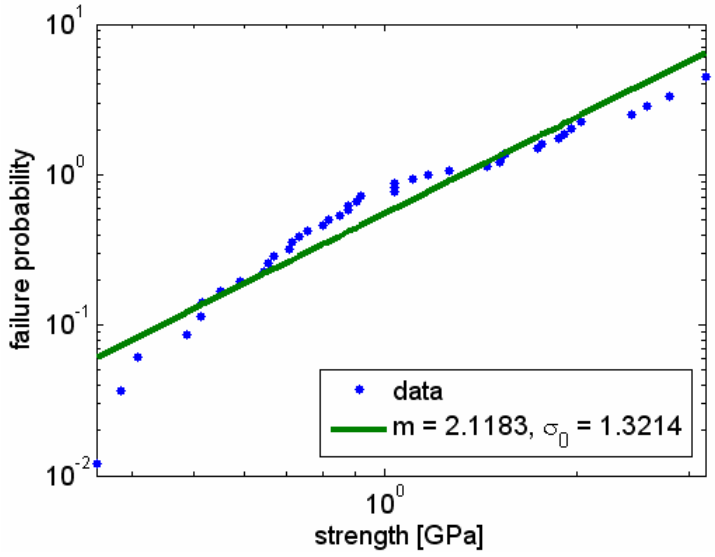

Figure D-5: Weibull Distribution for 4 inch 450μm Thick Wafer with 1 minute SF_6 and 42 Data Points

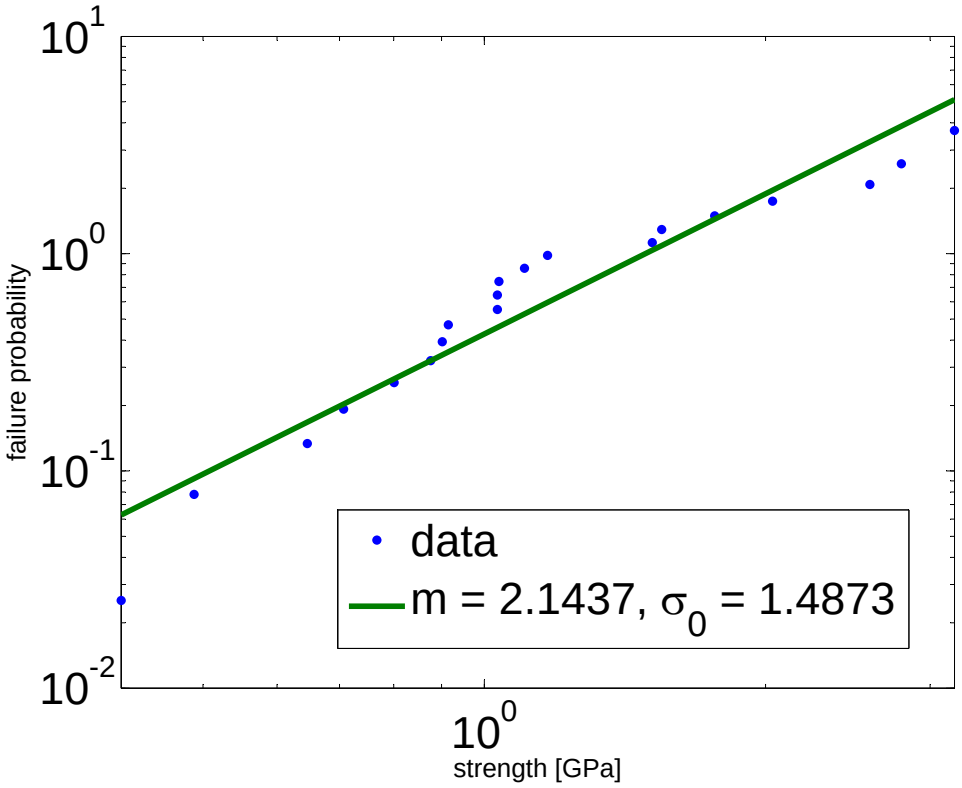

Figure D-6: Weibull Distribution resulting from data binning for 4 inch 450μm Thick Wafer with 1 minute SF_6 and 20 Data Points

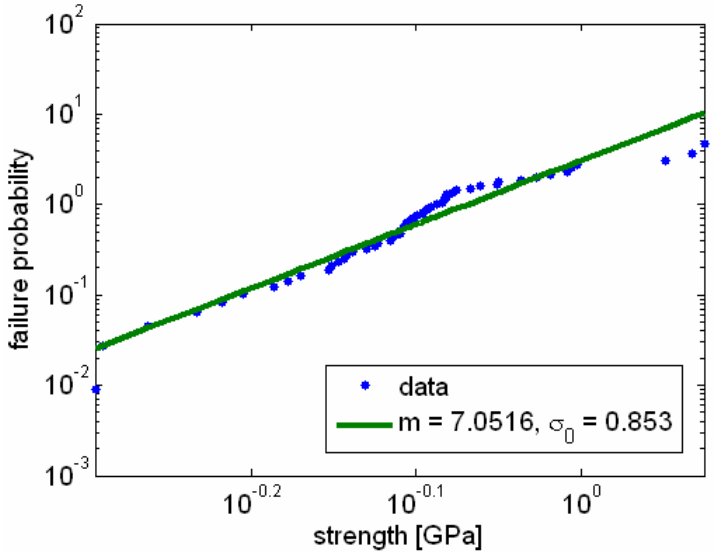

Figure D-7: Weibull Distribution for 4 inch 450μm Thick Wafer with 1 minute SF_6 and 0.5 hours H_2 Annealing and 56 Data Points

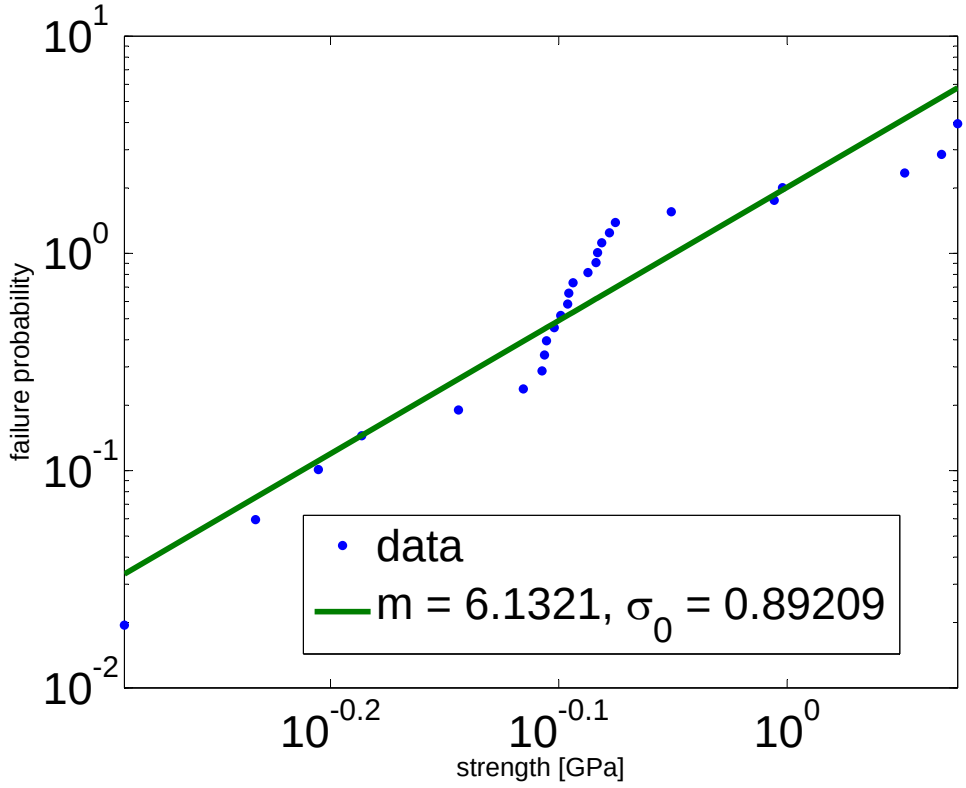

Figure D-8: Weibull Distribution resulting from data binning for 4 inch 450μm Thick Wafer with 1 minute SF_6 and 0.5 hours H_2 Annealing and 26 Data Points

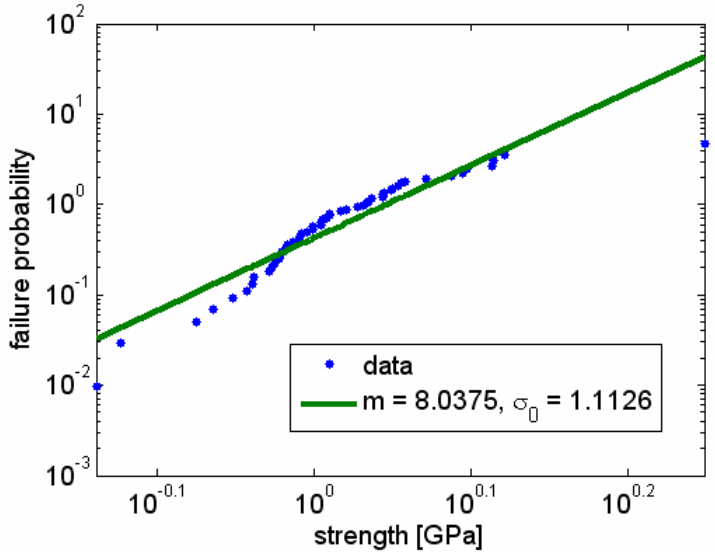

Figure D-9: Weibull Distribution for 4 inch 600μm Thick Wafer with 1 minute SF_6 and 2.5 hours H_2 Annealing and 52 Data Points

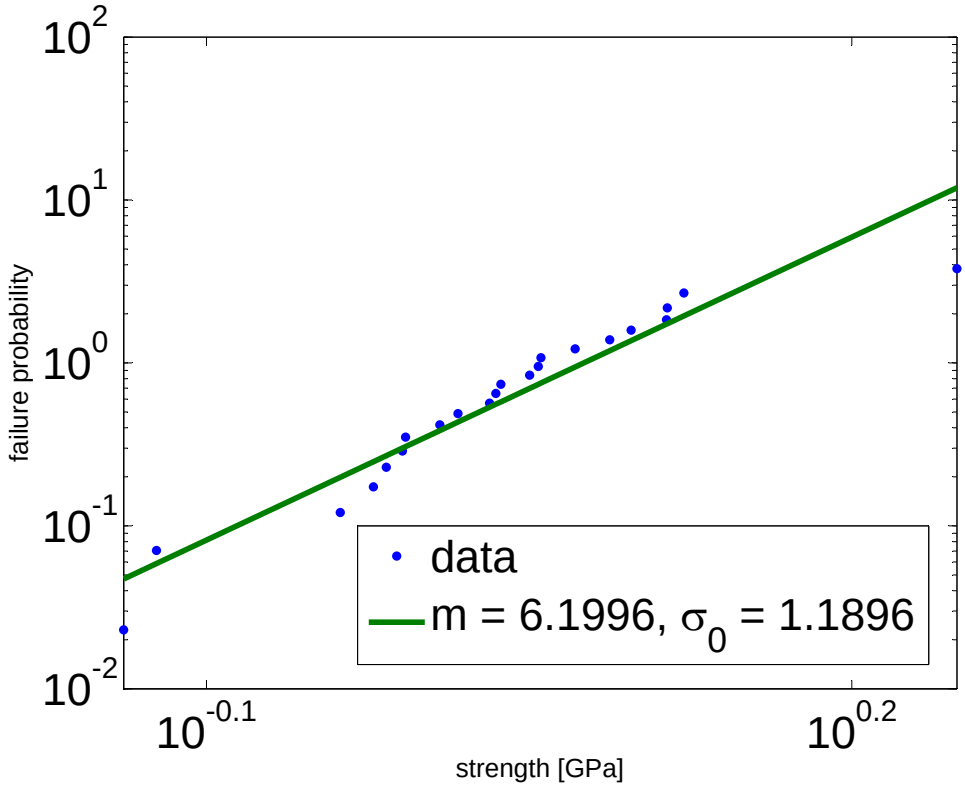

Figure D-10: Weibull Distribution resulting from data binning for 4 inch 600μm Thick Wafer with 1 minute SF_6 and 2.5 hours H_2 Annealing and 22 Data Points

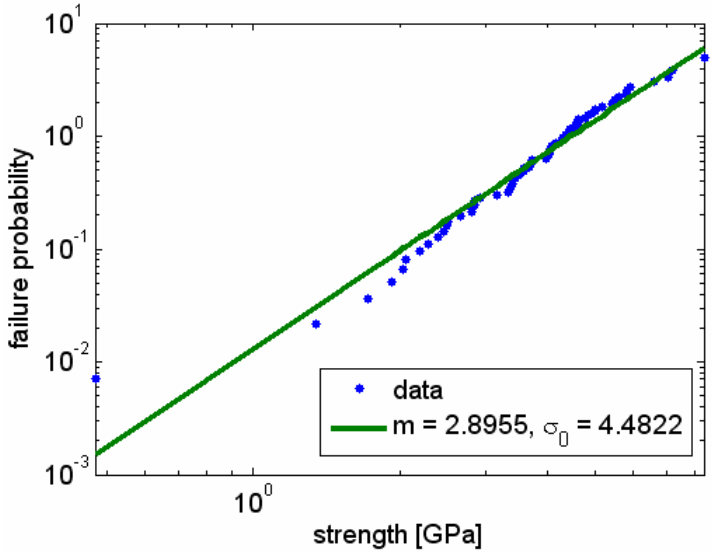

Figure D-11: Weibull Distribution for 6 inch 500μm Thick Wafer with 6 minutes SF_6 and 71 Data Points

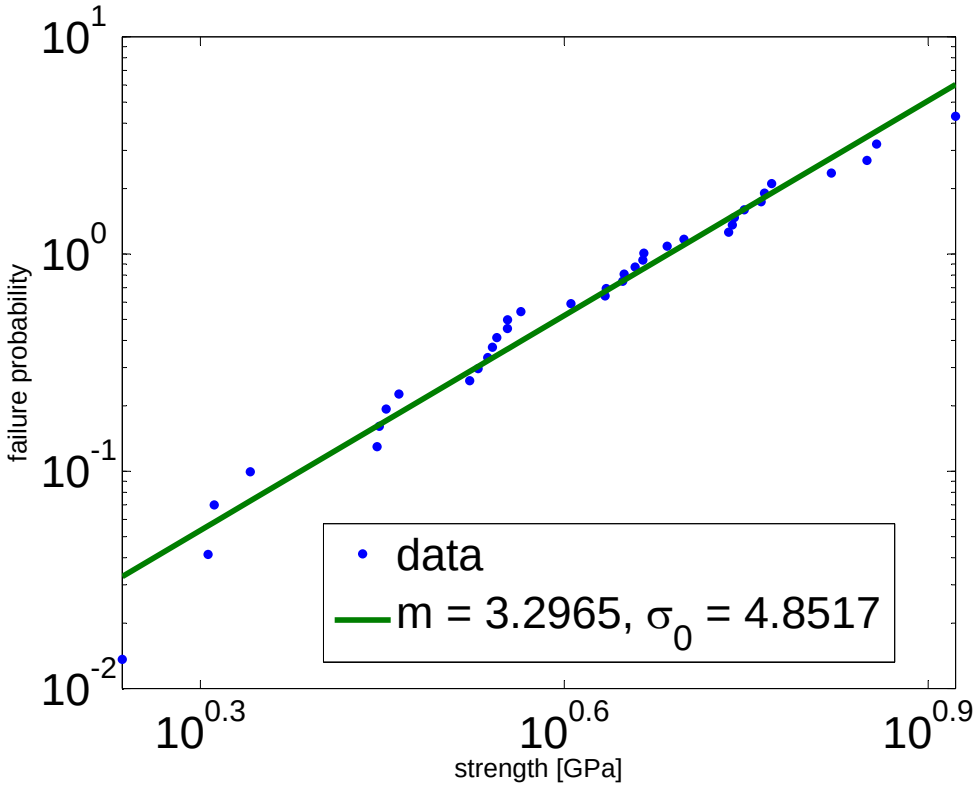

Figure D-12: Weibull Distribution resulting from data binning for 6 inch 500μm Thick Wafer with 6 minutes SF_6 and 37 Data Points

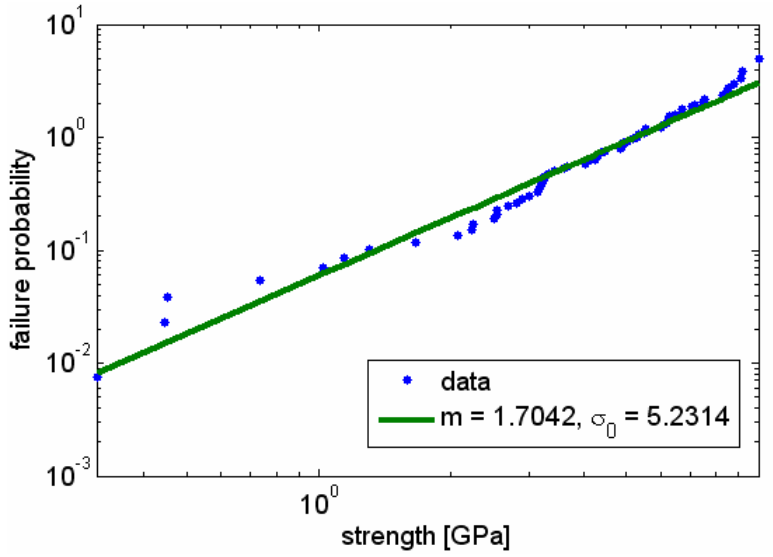

Figure D-13: Weibull Distribution for 6 inch 500μm Thick Wafer with 6 minutes SF_6 and Oxidation and 67 Data Points

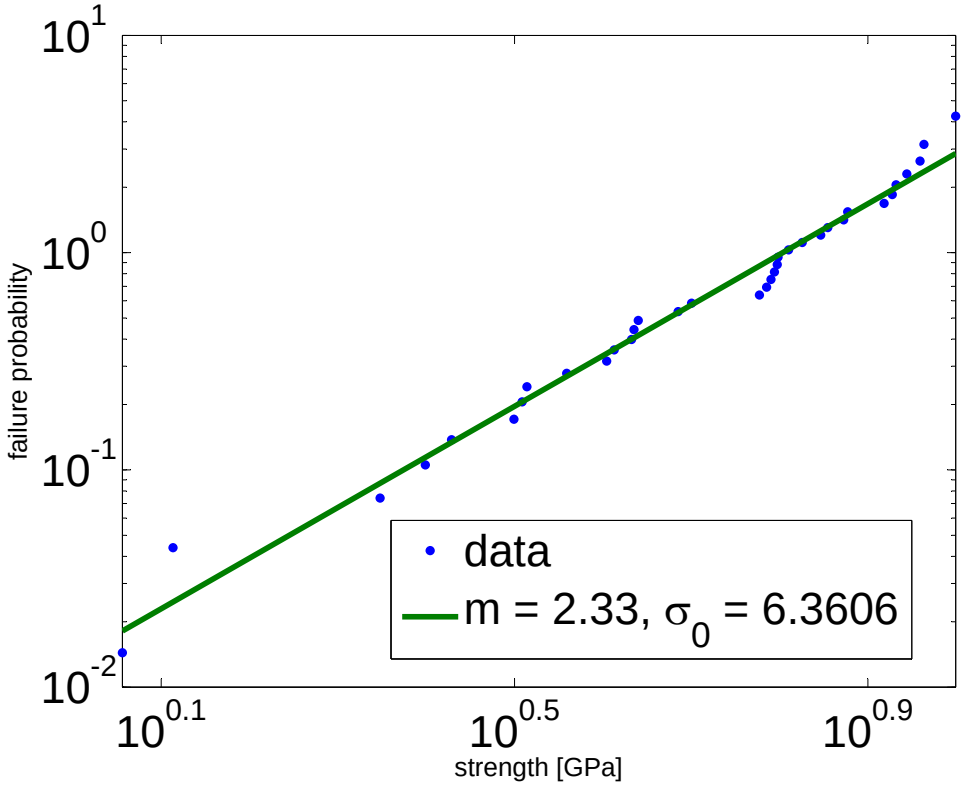

Figure D-14: Weibull Distribution resulting from data binning for 6 inch 500μm Thick Wafer with 6 minutes SF_6 and Oxidation and 35 Data Points

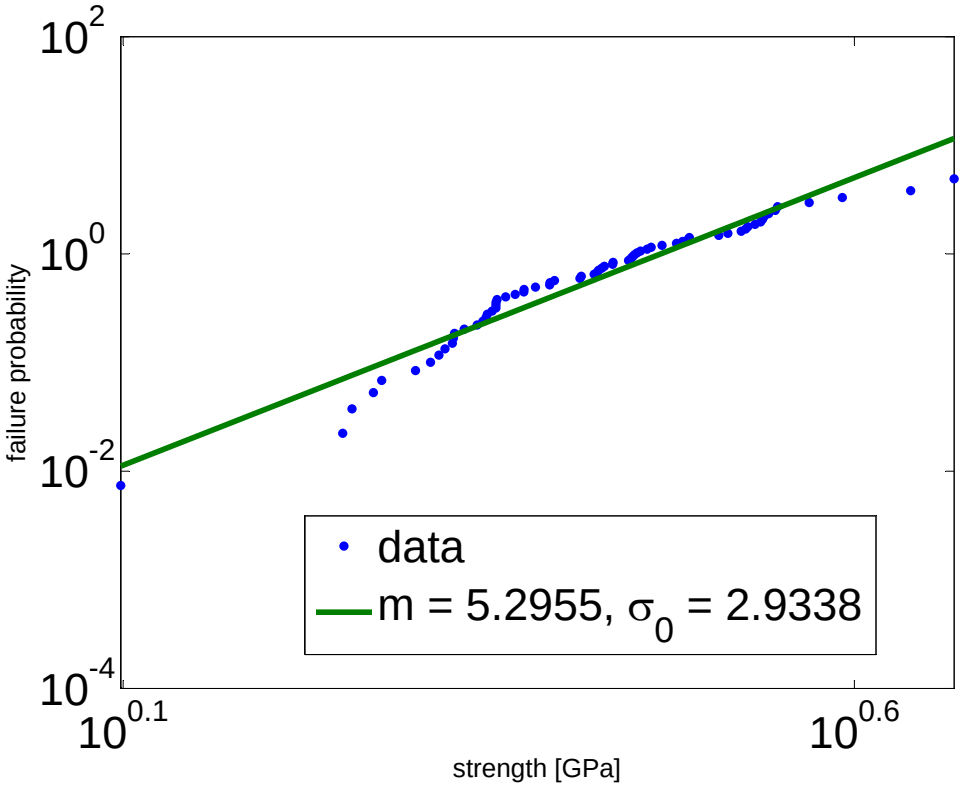

Figure D-15: Weibull Distribution for 6 inch 650μm Thick Wafer with 1 minute SF_6, Oxidation, and UHV and 68 Data Points

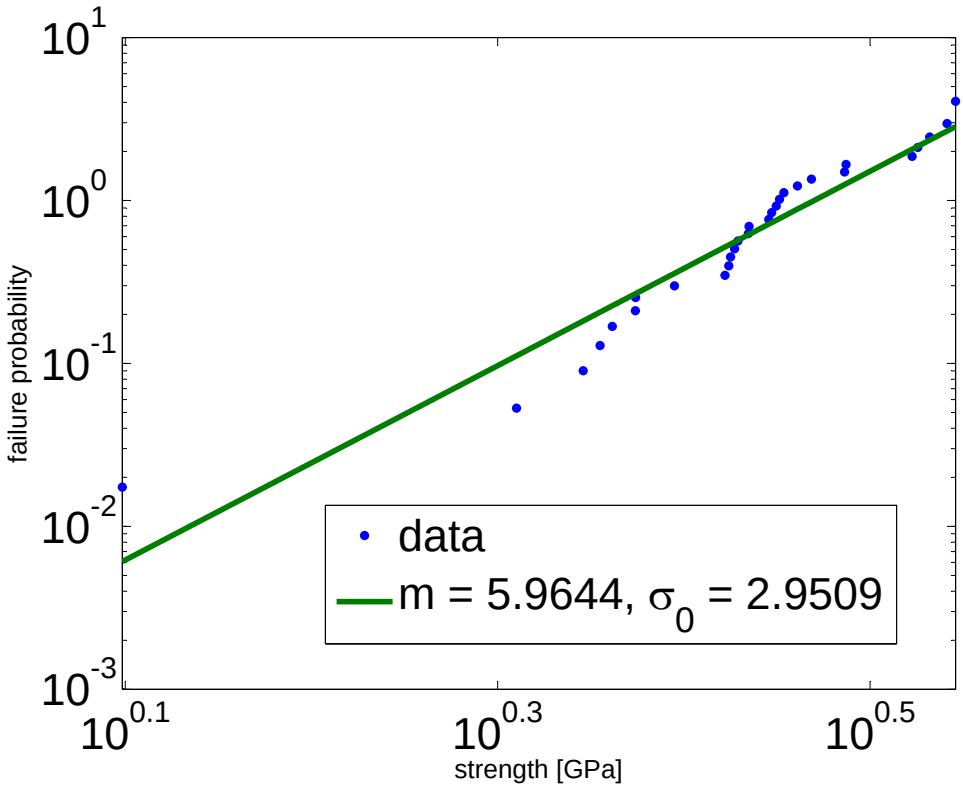

Figure D-16: Weibull Distribution resulting from data binning for 6 inch 650μm Thick Wafer with 1 minute SF_6, Oxidation, and UHV and 29 Data Points

Appendix E

Experimental Evaluation of Pressure Vessel Features

This appendix describes experimental work that can be done using a pressure vessel coupon (PVC) to demonstrate key aspects of the silicon pressure vessel design.

E.1 Pressure Vessel Coupon Design

The pressure vessel coupon design consists of the three concentric layers of honeycomb cells made by bonding two wafer layers together with small through-holes etched on the bottom through which the cells can be pressurized. Figure E-1 illustrated a single PVC with a cross-section taken through the top wafer so that the inside of the PVC can be seen. For ease of testings, the PVC is designed to be pressurized with an external connection to a high pressure tank with a minimum of 2000 psi pressure.

E.2 Fabrication

The fabrication of the PVC will now be described which is illustrated in figure E-2. The process begins with two double side polished <100> orientation wafers. The wafers are RCA cleaned so that they can be placed in a high temperature tube to have 500 nm of wet thermal oxide grown on them at 1000°C. Once coated with

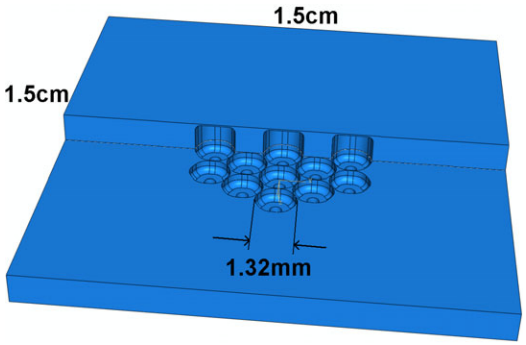

Figure E-1: Illustration of PVC with cross-section taken through top portion to reveal inner geometry

oxide, the front and back of the wafers are coated with a thick layer of photoresist with a thickness of about $8\mu m$. (Both the front and back of the wafer are coated with photoresist to protect the backside from damage during the etching processes.) Wafer 1 (indicated by W1 on figure E-2) is exposed with mask 1 (indicated by M1 on figure E-2) and developed to reveal the cell patterns. The oxide is then plasma etched (better results have been found with plasma etching of oxide over wet etching), the silicon is then etched with DRIE, and finally a isotropic SF_6 etch is done to give nearly spherical end caps on the cells. The second wafer (W2) is etched in nearly the same way as wafer 1 except that there will be an additional photo cycle and etch initially to create the through holes for pressurization on the wafer backside. The through-hole etch on wafer 2 will be done with a thick resist cycle, plasma oxide etching, and DRIE. The isotropic etch done on the frontside of wafer 2 will additionally smooth any roughness and sharp corners from the backside through-hole etch. The resist and oxide are stripped with an oxide plasma and wet HF etch from wafers 1 and 2 respectively. The wafers are then bonded together and exposed to surface migration for strength recovery. The wafers are then diced into individual PVC samples using a die saw.

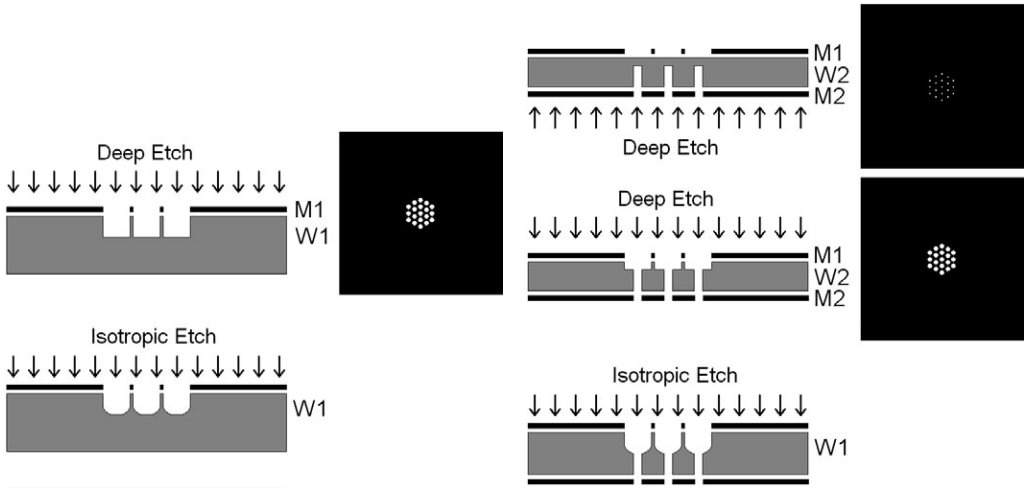

(a) Etch top portion of cells

(b) Etch bottom portion of cells with opening for pressurization

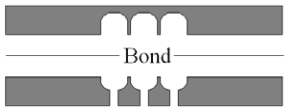

(c) Bond top and bottom cell portions together

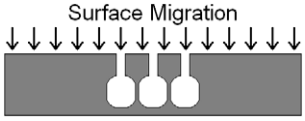

(d) Surface migration to reduce flaws

Figure E-2: Fabrication steps for PVC

E.3 Experimental Setup

An experimental setup was conceptualized to test the PVC. FigureE-3 illustrates a cross-section of the test setup. The test setup holds the PVC between two stainless steel plates held together with screws with area machined out to allow the PVC cells to deform as needed when pressurized. Two o-rings are used between the stainless steel blocks and the PVC to prevent leakage of pressurization gas and offer a softer interaction between the stainless steel supports and the silicon specimen.

E.4 FEM Modelling

Preliminary work was done using ABAQUS^{TM}to analyze deformation of the test setup and the stresses from the o-ring supports on the PVC. Figure E-4 illustrates how the pressure vessel coupon and o-ring interactions are modelled as circular pins on the

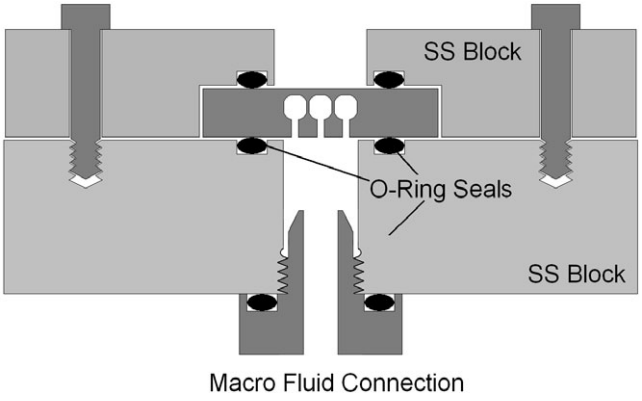

Figure E-3: Illustration of PVC experimental setup

top and bottom PVC surface. The light gray shading around the surfaces inside the bottom o-ring on the figure indicates the region exposed to pressurization in the model. Only a quarter of the coupon was simulated with symmetric boundary conditions on the quartered sides.

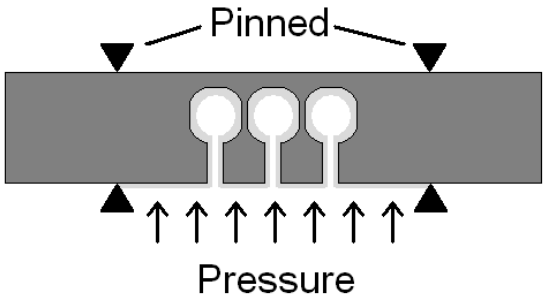

Figure E-4: Simplified model of o-rings as pins on PVC

Figure E-5 illustrates resultant principal stresses on a PVC designed with no significant SF_6 to form the somewhat spherical end caps on the PVC cells. The model is pressured with 2,000 psi. The model is not fully complete because it has not been successfully partitioned to have convergent behavior for increased mesh fineness. Mesh sensitivity for this model can be found in appendix F. The model should also be modelled with a larger fillet on the cell corners (to model a somewhat spherical end cap). The model however does suggest that the test setup proposed for the PVC will not result in significant bending of the structure which would corrupt the desire of the test to model actual pressure vessel behavior.

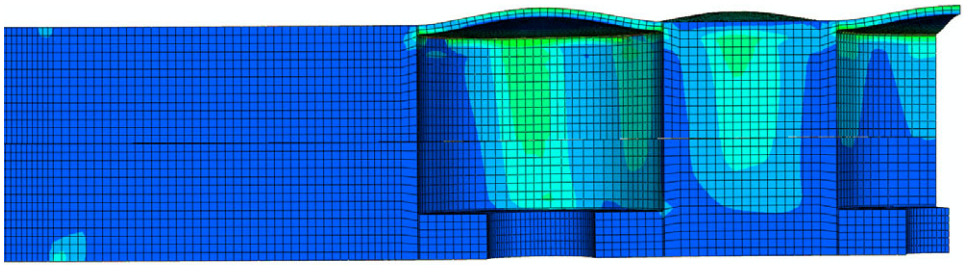

Figure E-5: Illustration of principal stress distribution in PVC FEM model with 2x exaggerated deformation

Appendix F

Mesh Sensitivity Studies

F.1 RHFS Mesh Sensitivity Studies

A mesh sensitivity study was done for the baseline RHFS FEM model for loads of 10.74MPa, 35.81MPa, and 57.3MPa. The results of this study are shown in the following plots. Fluctuations in maximum stress with respect to seed sizes smaller than $150\mu m$ showed minimal fluctuations. Seed size in the model represented the distance between seed points which defined distance between grid points. The smaller the seed size the finer the mesh. A seed size of $50\mu m$ was used for geometry variation studies. For the fillet radius area, partitions were manually added to the model to refine the mesh around the small geometry variation.

F.2 PVC Mesh Sensitivity Studies

A mesh sensitivity study was done for the baseline RHFS FEM model for loads of 6.895MPa, 10.34MPa, and 13.79MPa. The results of this study are shown in the following plot.

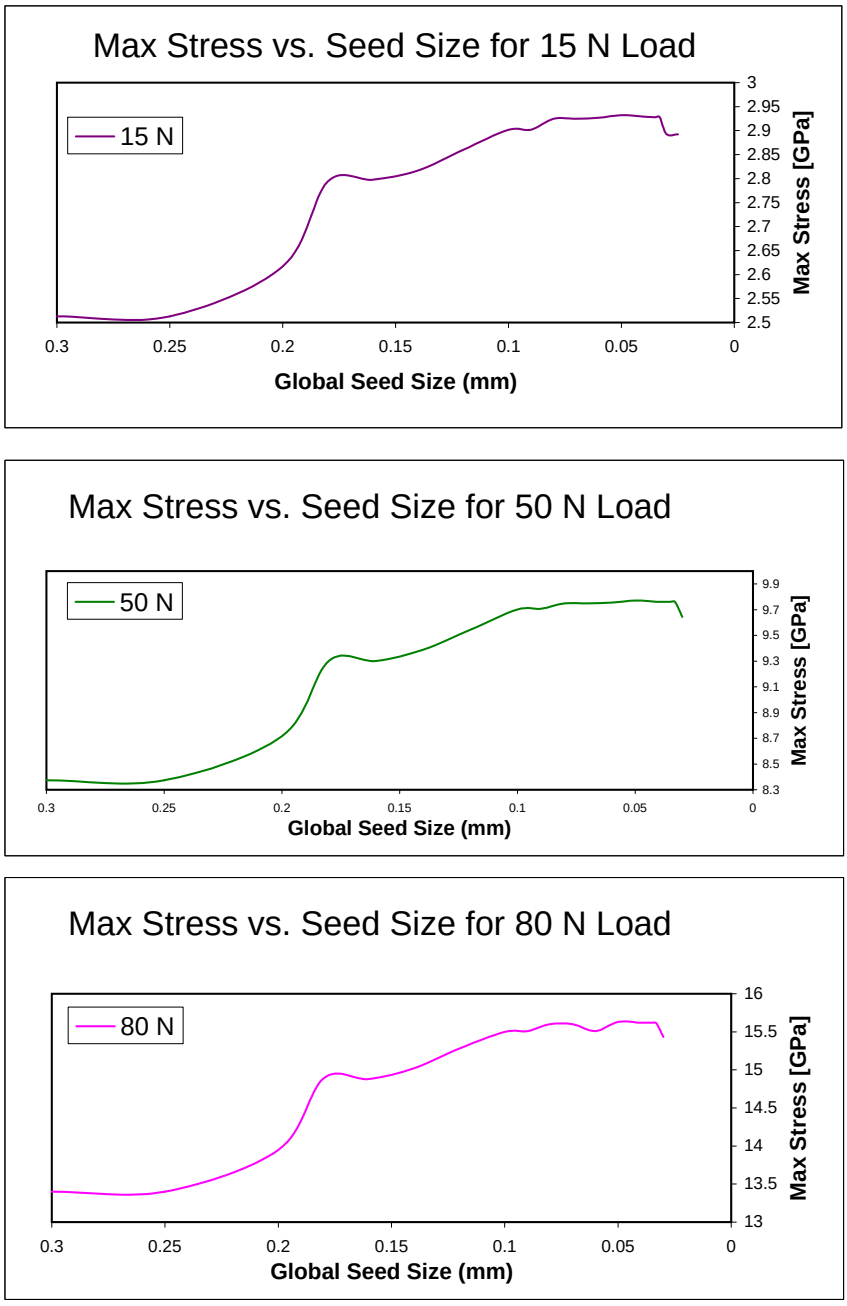

Figure F-1: RHFS FEM mesh sensitivity

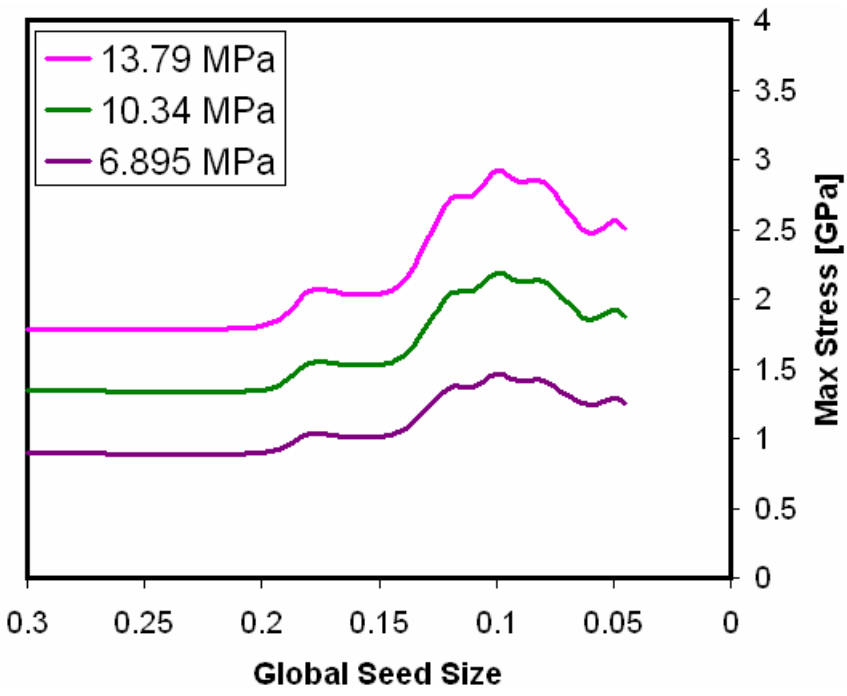

Figure F-2: PVC FEM mesh sensitivity

Bibliography

[1] Eugene A. Avallone, Theodore Baumeister, Ali Sadegh, and Lionel Simeon Marks. *Marks' standard handbook for mechanical engineers*. McGraw-Hill, Reading, Massachusetts, eleventh edition, 2006.

[2] A. A. Ayón, R. L. Bayt, and K. S. Breuer. Deep reactive ion etching: A promising technology for micro- and nanosatellites. *Smart Materials and Structures*, 10:1135–1144, 2001.

[3] E. H. Baker, L. Kovalevsky, and F. L. Rish. *Structural Analysis of Shells*, chapter 2. Rober E. Krieger Publishing Company, Huntington, New York, second edition, 1981.

[4] Ralph L. Barnett, Paul C. Hermann, James R. Wingfield, and Chester L. Connors. Fracture of brittle materials under transient mechanical and thermal loading. Technical Paper 0879946, IIT Research Institute, Chicago, Illinois, March 1967.

[5] Richard Budynas and Keith Nisbett. *Shigley's Mechanical Engineering Design*. Mcgraw-Hill, New York, NY, eighth edition, 2006.

[6] Caltech. Properties of silicon, January 2011. `http://www.design.caltech.edu/Research/MEMS/siliconprop.html`.

[7] I. Chakraborty, D. P. Bame, J. Mueller, and W. C. Tang. Mems micro-valve for space applications. *Sensors and Actuators A: Physical*, 83(1), 2000.

[8] Kuo-Shen Chen. *Characterization and Structural Design of Ceramic Micro Turbomachinery*. PhD dissertation, Massachusetts Institute of Technology, Department of Aeronautics and Astronautics, February 1999.

[9] W. E. C. Creyke, I. E. J. Sainsbury, and R. Morrell. *Design with Non-Ductile Materials*, section 3.5, pages 73–95. Applied Science Publishers LTD, Essex, England, 1982.

[10] Alissa M. Fitzgerald, David M. Pierce, Brent M. Huigens, and Carolyn D. White. A general methodology to predict the reliability of single-crystal silicon mems devices. *Journal of Microelectromechanical Systems*, 18(4):962–970, August 2009.

[11] A. M. Freudenthal. *Statistical approach to brittle fracture*, volume 2 of *Fracture, An Advanced Treatise*, pages 591–619. Academic Press, New York, New York, 1968.

[12] K Gabriel, W Trimmer, and M Mehregany. Micro gears and turbine etched from silicon. In *Transducers*, number 12, pages 341–348, March 1987.

[13] A. A. Griffith. The phenomena of rupture and flow in solids. *Philosophical Transactions of the Royal Society*, pages 163–198, 1921. This is a full ARTICLE entry.

[14] Hank Heidt, Jordi Puig-Suari, Augustus S. Moore, Schinichi Nakasuka, and Robert J. Twiggs. Cubesat: A new ganeration of picosatellite for education and industry low-cost space experimentation. In *14th Annual Small Satellite Conference*, Logan, UT, August 2000.

[15] A.M. Howatson, P.G. Lund, and J.D. Todd. *Engineering Tables and Data*. Chapman and Hall, Reading, Massachusetts, second edition.

[16] Tai-Ran Hsu. *MEMS packaging*. EMIS Processing Series 3. Inspec, Reading, Massachusetts, 2004.

[17] S. M. Hu. Critical stress in silicon brittle fracture, and effect of iion implantation and other surface treatements. *Journal of Applied Physics*, 53(5):3576–3580, May 1982.

[18] Michael A. Huff, Alex D. Nikolich, and Martin A. Schmidt. Design of sealed cavity microstructures formed by silicon wafer bonding. *Journal of Microelectromechanical Systems*, 2(2):74–81, 1993.

[19] Michael A. Huff and Martin A. Schmidt. Fabrication, packaging, and testing of a wafer-bonded microvalve. In *Solid-State Sensor and Actuator Workshop*, pages 194–197, Hilton Head Island, 1992.

[20] Robert Hull. *Properties of Crystalline Silicon*. Institution of Engineering and technology, 13September 2005.

[21] Stefan Johansson, Jan-Åke Schweitz, Lars Tenerz, and Jonas Tirén. Fracture testing of silicon microelements *in situ* in a scanning electron microscope. *Journal of Applied Physics*, 63(10):4799–4803, May 1988.

[22] Richard J. Francis Jr. A system study of very small launch vehicles. Master's project, Massachusetts Institute of Technology, Department of Aeronautics and Astronautics, September 1999.

[23] Anthony Kelly and N. H. Macmillan. *Strong Solids*. Monographs on the Physics and Chemistry of Materials. Oxford Science Publications, New York, third edition, 1986.

[24] Hitoshi Kuribayashi, Reiko Hiruta, Ryosuke Shimizu, Koichi Sudoh, and Hirohsi Iwasaki. Shape transormation of silicon trenches during hyrogen annealing. *Journal of Vacuum Science & Technology A*, 21(4):1279–1283, October 2003.

[25] Ming-Chang M. Lee and Ming C. Wu. Thermal annealing in hydrogen for 3-d profile transformation on silicon-on-insulator and sidewall roughness reduciton. *Journal of Microelectromechanical Systems*, 15(2):338–343, April 2006.

[26] Q. Liu, L. Spanos, C. Zhao, and E. A. Irene. A morphology study of the thermal oxidation of rough silicon surfaces. *Journal of Vacuum Science & Technology A*, 13(4):1977–1983, 1955.

[27] R. B. Marcus and T. T. Sheng. The oxidation of shaped silicon surfaces. *Journal of the Electrochemical Society*, 129(6):1278–1282, 1982.

[28] N. N. Nemeth, O. Jadaan, J.P. Palko, J. Mitchell, and C. A. Zorman. Structural modeling and probabilitistic characterization of mems pressure sensor membranes. In *Proceedings of the MEMS: Mechanics and Measurements Syposium*, pages 46–51, Portland, Oregon, 2001.

[29] Noel N. Nemeth, Jane M. Manderscheid, and John P. Gyekenyesi. Ceramics analysis and reliability evaluation of structures life prediction program (cares/life) users and programmers manual. NASA Technical Paper 2916, NASA, August 1990.

[30] Lien T. Ngo, Dorothée Almécija, John E. Sader, Brian Daly, Nikolay Petkov, Justin D. Holmes, Donats Erts, and John J. Boland. Ultimate-strength germanium nanowires. *Nano Letters*, 6(12):2964–2968, 2006.

[31] Erin E. Noonan. *Structural Analysis of the MIT Micro Rocket Combustion Chamber*. PhD dissertation, Massachusetts Institute of Technology, Department of Aeronautics and Astronautics, June 2002. This is a full PHDTHESIS entry.

[32] Kurt E. Petersen. Silicon as a mechanical material. *Proceedings of the IEEE*, 70(5):420–446, May 1982.

[33] W.T. Pike, W. J. Karl, S. Kumar, S. Vijendran, and T. Semple. Analysis of sidewall quality in through-wafer deep reactive-ion etching. *Microelectronic Engineering*, 73, 2004.

[34] Egor Paul Popov. *Engineering Mechanics of Solids*. Prentice Hall, Englewood Cliffs, N.J., second edition, 1990.

[35] Tsutomu Sato, Kunihiro Mitsutake, Ichiro Mizushima, and Yoshitaka Tsunashima. Micro-structure transformation of silicon: A newly developed transformation technology for patterning silicon surfaces using the surface migration of silicion atoms by hydrogen annealing. *Japan Journal of Applied Physics*, 39(9), 2000.

[36] Stephen D. Senturia. *Microsystem Design*, chapter 1.2, pages 69–71. Kluwer Academic Publishers, first edition, 2000.

[37] Daniel K. Sparacin, Steven J. Spector, and Lionel C. Kimerling. Silicon waveguide sidewall smoothing by wet chmical oxidation. *Journal of Lightwave Technology*, 23(8):2455–2461, August 2005.

[38] S. Mark Spearing. Materials and processes: A research overview. *Advanced Materials for Micro- and Nano- Systems*, 1, 2004.

[39] Y. Su, A. G. R. Evans, and Brunnschweiler. Micromachines silicon cantilever paddles with piezoresistive readout for flow sensing. *Journal of Micromechanics and Microengineering*, 6(1):69–72, 1996.

[40] S. Timoshenko and S. Woinowsky-Krieger. *Theory of Plates and Shells*. McGraw-Hill Company, New York, New York, second edition, 1959.

[41] Ernst Hjalmar Waloddi Weibull. A statistical theory of the strength of materials. *Generalstabens Litografiska Anstalts*, 20(151):1–45, 1939.

[42] Wikipedia. Boule (crystal), January 2011. `http://en.wikipedia.org/wiki/Boule_(crystal)`.

[43] Wikipedia. Deep reactive-ion etching, January 2011. `http://en.wikipedia.org/wiki/Deep_reactive-ion_etching`.

[44] Warren C. Young. *Roark's Formulas for Stress & Strain*. McGraw-Hill, sixth edition, 1989.

[45] Warren C. Young. *Roark's Formulas for Stress & Strain*. McGraw-Hill, sixth edition, 1989.